

REPORT DOCUMENTATION PAGE

Form Approved OMB NO. 0704-0188

The public reporting burden for this collection of information is estimated to average 1 hour per response, including the time for reviewing instructions, searching existing data sources, gathering and maintaining the data needed, and completing and reviewing the collection of information. Send comments regarding this burden estimate or any other aspect of this collection of information, including suggestions for reducing this burden, to Washington Headquarters Services, Directorate for Information Operations and Reports, 1215 Jefferson Davis Highway, Suite 1204, Arlington VA 22202-4302. Respondents should be aware that notwithstanding any other provision of law, no person shall be subject to any penalty for failing to comply with a collection of information if it does not display a currently valid OMB control number.
PLEASE DO NOT RETURN YOUR FORM TO THE ABOVE ADDRESS.

1. REPORT DATE (DD-MM-YYYY) 28-09-2015	2. REPORT TYPE Final Report	3. DATES COVERED (From - To) 1-Sep-2012 - 31-May-2016		
4. TITLE AND SUBTITLE Final Report: Exploitation of Full-Waveform LiDAR to Characterize / Exploit Under Canopy Targets - Foliage Penetration (FOPEN)		5a. CONTRACT NUMBER W911NF-12-1-0181		
		5b. GRANT NUMBER		
		5c. PROGRAM ELEMENT NUMBER 622784		
6. AUTHORS Charles Toth, Dorota A. Grejner-Brzezinska		5d. PROJECT NUMBER		
		5e. TASK NUMBER		
		5f. WORK UNIT NUMBER		
7. PERFORMING ORGANIZATION NAMES AND ADDRESSES Ohio State University 1960 Kenny Road Columbus, OH 43210 -1016		8. PERFORMING ORGANIZATION REPORT NUMBER		
9. SPONSORING/MONITORING AGENCY NAME(S) AND ADDRESS (ES) U.S. Army Research Office P.O. Box 12211 Research Triangle Park, NC 27709-2211		10. SPONSOR/MONITOR'S ACRONYM(S) ARO		
		11. SPONSOR/MONITOR'S REPORT NUMBER(S) 59687-EV.2		
12. DISTRIBUTION AVAILABILITY STATEMENT Approved for Public Release; Distribution Unlimited				
13. SUPPLEMENTARY NOTES The views, opinions and/or findings contained in this report are those of the author(s) and should not be construed as an official Department of the Army position, policy or decision, unless so designated by other documentation.				
14. ABSTRACT Foliage presents a type of terrain characteristic that can obstruct information required by the warfighter. Traditional remote sensing offers rather limited, if any, capabilities to acquire data under the canopy. Recently, state-of-the-art LiDAR technology, in particular waveform processing, can provide not only foliage penetration but can also support better object identification and material classification under the canopy. To make use of this relatively new technology, not yet operational in the Army's surveillance and reconnaissance practice, this project aims at contributing to much needed research necessary to build up the gap between the potential of an active sensor				
15. SUBJECT TERMS LiDAR, laserscanning, waveform				
16. SECURITY CLASSIFICATION OF: a. REPORT UU		17. LIMITATION OF ABSTRACT b. ABSTRACT UU	18. NUMBER OF PAGES c. THIS PAGE UU	19a. NAME OF RESPONSIBLE PERSON Charles Toth
				19b. TELEPHONE NUMBER 614-292-7681

Report Title

Final Report: Exploitation of Full-Waveform LiDAR to Characterize / Exploit Under Canopy Targets - Foliage Penetration (FOPEN)

ABSTRACT

Foliage presents a type of terrain characteristic that can obstruct information required by the warfighter. Traditional remote sensing offers rather limited, if any, capabilities to acquire data under the canopy. Recently, state-of-the-art LiDAR technology, in particular waveform processing, can provide not only foliage penetration but can also support better object identification and material classification under the canopy. To make use of this relatively new technology, not yet operational in the Army's surveillance and reconnaissance practice, this project aims at contributing too much needed research necessary to bridge the gap between the potential of an active sensor technology and the implementation of deployable systems. The proposed approach is based on combining the use of targets and materials, assessed by full waveform LiDAR, to understand and, consequently, develop the acquisition strategy, processing, and product generation necessary to best exploit the mission. Our objective is to model full waveform LiDAR acquisition parameters designed around various canopy and foliage types (e.g., single to multi- storied canopies, temperate, tropical, sub-tropical) that are of major interest from the Army's operational standpoint. Matching canopy type to LiDAR acquisition would more effectively drive any given sortie and optimize the mission acquisition and support the Army's field operations, including planning, battlefield command and logistics in general.

Enter List of papers submitted or published that acknowledge ARO support from the start of the project to the date of this printing. List the papers, including journal references, in the following categories:

(a) Papers published in peer-reviewed journals (N/A for none)

Received Paper

TOTAL:

Number of Papers published in peer-reviewed journals:

(b) Papers published in non-peer-reviewed journals (N/A for none)

Received Paper

TOTAL:

Number of Papers published in non peer-reviewed journals:

(c) Presentations

Number of Presentations: 3.00

Non Peer-Reviewed Conference Proceeding publications (other than abstracts):

Received Paper

08/31/2014 1.00 Charles K. Toth, Zoltan Koppanyi, Sandor Laky, John Anderson, Ricky Massaro. THE IMPACT OF INCIDENCE ANGLE ON LIDAR WAVEFORM,
Ca/GIS ASPRS 2013 Specialty Conference. 28-OCT-13, . : ,

TOTAL: **1**

Number of Non Peer-Reviewed Conference Proceeding publications (other than abstracts):

Peer-Reviewed Conference Proceeding publications (other than abstracts):

Received Paper

TOTAL:

Number of Peer-Reviewed Conference Proceeding publications (other than abstracts):

(d) Manuscripts

Received Paper

TOTAL:

Number of Manuscripts:

Books

Received Book

TOTAL:

Received Book Chapter

TOTAL:

Patents Submitted

Patents Awarded

Awards

Graduate Students

<u>NAME</u>	<u>PERCENT SUPPORTED</u>	Discipline
Zoltan Koppanyi	0.50	
FTE Equivalent:	0.50	
Total Number:	1	

Names of Post Doctorates

<u>NAME</u>	<u>PERCENT SUPPORTED</u>
FTE Equivalent:	
Total Number:	

Names of Faculty Supported

<u>NAME</u>	<u>PERCENT_SUPPORTED</u>	National Academy Member
Charles Toth	0.15	
FTE Equivalent:	0.15	
Total Number:	1	

Names of Under Graduate students supported

<u>NAME</u>	<u>PERCENT_SUPPORTED</u>
FTE Equivalent:	
Total Number:	

Student Metrics

This section only applies to graduating undergraduates supported by this agreement in this reporting period

The number of undergraduates funded by this agreement who graduated during this period: 0.00

The number of undergraduates funded by this agreement who graduated during this period with a degree in science, mathematics, engineering, or technology fields:..... 0.00

The number of undergraduates funded by your agreement who graduated during this period and will continue to pursue a graduate or Ph.D. degree in science, mathematics, engineering, or technology fields:..... 0.00

Number of graduating undergraduates who achieved a 3.5 GPA to 4.0 (4.0 max scale):..... 0.00

Number of graduating undergraduates funded by a DoD funded Center of Excellence grant for Education, Research and Engineering:..... 0.00

The number of undergraduates funded by your agreement who graduated during this period and intend to work for the Department of Defense 0.00

The number of undergraduates funded by your agreement who graduated during this period and will receive scholarships or fellowships for further studies in science, mathematics, engineering or technology fields:..... 0.00

Names of Personnel receiving masters degrees

<u>NAME</u>
Total Number:

Names of personnel receiving PHDs

<u>NAME</u>	
Zoltan Koppanyi	
Total Number:	1

Names of other research staff

<u>NAME</u>	<u>PERCENT_SUPPORTED</u>
FTE Equivalent:	
Total Number:	

Sub Contractors (DD882)

Inventions (DD882)

Scientific Progress

This research has advanced the understanding of LiDAR waveform. In particular, the relationship between the material characteristic of the object space and the waveform shape.

Technology Transfer



Study title:

Exploitation of Full-waveform LiDAR to Characterize/Exploit under Canopy Targets - Foliage Penetration (FOPEN)

Authors:

Charles Toth¹ and Dorota A. Grejner-Brzezinska²

Center for Mapping¹
Department of Civil and Environmental and Geodetic
Engineering²
The Ohio State University

Report date:

August 2015

Sponsor name:

Army Research Office

Acknowledgments

The authors thank the staff of the ARO for their contributions to this project. In particular, we want to express our gratitude to Dr. John Anderson, USACE ERDC Remote Sensing and Fluorescence Spectroscopy Lab, for his leadership and technical assistance. The authors greatly appreciate the support of Ricky Massaro and Jarrod Edwards for their continuing support and coordination of the system acquisition and the field testing. Thanks should go to Jason Woolard from NOAA for providing the multi-sensor LiDAR datasets.

Contents

1.	INTRODUCTION.....	8
2.	RESEARCH OBJECTIVES	8
3.	INCIDENCE ANGLE DEPENDENCE STUDY	10
3.1	Background	10
3.2	Test Dataset	12
3.3	Processing ScanPos1 and ScanPos2 Datasets	17
3.3.1	Point filtering	20
3.3.2	Basic characterization of waveform groups.....	22
3.3.3	Gaussian waveform decomposition.....	24
3.3.4	Incidence angle estimation with feed forward neural network	28
3.3.5	Surface material classification based on waveform data	31
3.4	Processing ScanPos4 Dataset.....	33
3.4.1	Gaussian parameters	36
3.4.2	Solution with feed-forward neural network.....	37
4.	WAVEFORM-BASED CLASSIFICATION FROM AIRBORNE LIDAR	39
4.1	Background	39
4.2	Data set	40
4.3	Data processing.....	41
4.3.1	Data preprocessing	41
4.3.2	Feature extraction.....	45
4.4	Data classification	49
4.4.1	Classifiers	50
4.4.2	Confusion matrix.....	56
4.4.3	The library and tools	58
4.5	Classification evaluation	58
4.5.1	Incidence angle estimation	58
4.5.2	Clustering with SOM neutral network	66
4.5.3	Land classification	70

5. LiDAR SYSTEM PERFORMANCE COMPARISONS.....	85
6. CONCLUSION AND FUTURE TASKS.....	86
7. REFERENCES	87
8. APPENDIX	88
8.1 ISPRS Technical Commission I Symposium, Denver, CO, November 17-20, 2014.....	88
8.2 Research discussion presentation.....	96
8.3 Photogrammetrie, Fernerkundung, Geoinformation (PFG, ISSN 1432-8364)	118

Figure 1 Impact of incidence angle	11
Figure 2 Time delay as a function of the incidence angle (a), and changes of the shape of the Gaussian waveform due different incidence angles (b).....	12
Figure 3 USACE ERDC mobile measurement system with Riegl VZ-400 laser scanner (a) and OSU GPSVan with targets (b).....	13
Figure 4 Field survey locations, OSU West Campus; shakeup area is marked in green, survey range with targets is marked by red line, and survey of man-made objects area is marked by yellow.....	14
Figure 5 Shakeup are point cloud	15
Figure 6 Target materials	15
Figure 7 Workflow of the raw data processing.....	16
Figure 8 Relative channel gain and high channel intensities (a), actual and computed low and high channel intensities (b).....	17
Figure 9 Intensity values at near zero incidence angle.....	18
Figure 10 Various positions and orientations of the van in the XY plane.....	18
Figure 11 Calculation of the incidence angle	19
Figure 12 Point cloud of a disk target (red) with fitting plane, points within 1 cm distance from plane (blue), points after rotation to XZ plane (green)	21
Figure 13 Points within 25 cm from the center	21
Figure 14 Full waveforms grouped by materials (blue), and average waveforms (red).....	22
Figure 15 Full waveforms from all targets grouped by incidence angle (blue), and average waveforms (red).....	23
Figure 16 Directions illustrating when no waveforms are obtained from target 3 (highly reflective metal)	24
Figure 17 Generalized Gaussian shape functions	25
Figure 18 Fitting Gaussian shape to a typical waveform	26
Figure 19 Gaussian fitting parameters as a function of incidence angle, grouped by the five target materials (red: retro reflective, blue: wood, cyan: fluffy plastic, yellow: cardboard, and black: painted wood)	27
Figure 20 Gaussian fitting parameters as a function of incidence angle, grouped by the four target materials (blue: wood, cyan: fluffy plastic, yellow: cardboard, and black: painted wood).....	28
Figure 21 Waveforms shapes of in the three classes.....	32
Figure 22 Buildings used in investigation.....	35
Figure 23 Waveforms as functions of horizontal (left) and vertical (right) incidence angle (Building I)	35
Figure 24 Gaussian parameters of Building I	36
Figure 25 Gaussian parameters of Building II	37
Figure 26 Calculated and correct solution for Building I.....	38
Figure 27 Calculated and correct solution for Building II.....	39
Figure 28 Locations in the sensor coordinate system from the Riegl Waveform Extraction Library Manual (Page 6)	42
Figure 29 Laser beam directions	43

Figure 30 Scan angles from LAS file and calculated values from the SDF file using the direction vector ..	44
Figure 31 Scan angles provided by LAS file and the calculated angles from the SDF file using the origin and direction vectors	44
Figure 32 The effect of the parameters on the shape of the function	46
Figure 33 Shift correction of waveforms	48
Figure 34 Median and average waveforms	49
Figure 35 Final configuration of the pattern recognition neural network.....	52
Figure 36 References (upper) and simulated waveforms (lower)	53
Figure 37 The pattern recognition feed forward neural network results on the simulated data	54
Figure 38 Configuration of the SOM network.....	55
Figure 39 Roof with two classes (left) and aerial photo of the building (right)	59
Figure 40 Plan fitting and outlier removal	60
Figure 41 Histograms of the six Gaussian parameters	61
Figure 42 Histograms of skewness and kurtosis; mean and median are marked be red and green, respectively	62
Figure 43 Confusion matrix from the discriminant analysis	62
Figure 44 Typical waveforms with spline interpolation used for visualization.....	63
Figure 45 Median waveforms for the two classes	64
Figure 46 Neural network based classification performance	66
Figure 47 Road test area; orthophoto (a), altitude (b), and scan angle (c)	67
Figure 48 SOM result from original waveforms.....	68
Figure 49 SOM result from translated waveforms	70
Figure 50 Land type categories (classes)	71
Figure 51 Land type classes after filtering	72
Figure 52 Statistics of sample vectors per class	73
Figure 53 Median sample vectors from translated sample vectors samples (left), and the classification results (right).....	74
Figure 54 Median sample vectors from translated sample vectors	74
Figure 55 Distances from median waveform	75
Figure 56 Histograms of the Gaussian parameters by the categories	78
Figure 57 Kurtosis and skewness	79
Figure 58 Land classification by SOM with 4x4 neuron configuration (left) and 2x2 neuron configuration (right)	81
Figure 59 Results on the training set before applying mode filter (top) and after if (bottom)	83
Figure 60 Results on the validation set before applying mode filter (top) and after if (bottom).....	84

Table 1 Description of the datasets	14
Table 2 Direction of the disks, determined from measurements.....	20
Table 3 Coarse target reflectivity grouping	22
Table 4 Feed forward neural network for incidence angle determination for the retro reflective target.	30
Table 5 Feed forward neural network for incidence angle determination for all the targets.....	30
Table 6 Classification results for three classes.....	32
Table 7 Classification results for two classes	33
Table 8 The main parameters of the NGA data acquisition data sets	40
Table 9 Features.....	45
Table 10 Shift corrections	48
Table 11 Median and average waveforms.....	49
Table 12 Classifiers.....	50
Table 13 Classification using L2 norm	51
Table 14 Classification using max norm.....	51
Table 15 Confusion matrix	56
Table 16 Software and 3rd party libraries (links from 2014).....	58
Table 17 Statistics of point removal	60
Table 18 Statistics of the Gaussian parameters.....	61
Table 19 Skewness and Kurtosis results	61
Table 20 Classification by the distance from the median waveform without threshold	76
Table 21 Classification by the distance from the median waveform with at 0.5 sigma threshold	77
Table 22 Classification by the distance from the median waveform with 0.2 sigma threshold.....	77
Table 23 Linear discriminant analysis of the Gaussian parameters.....	79
Table 24 Combined method	81

1. INTRODUCTION

Foliage presents a type of terrain characteristic that can obstruct information required by the warfighter. Traditional remote sensing offers rather limited, if any, capabilities to acquire data under the canopy. Recently, state-of-the-art LiDAR technology, in particular waveform processing, can provide not only foliage penetration but can also support better object identification and material classification under the canopy. To make use of this relatively new technology, not yet operational in the Army's surveillance and reconnaissance practice, this project aims at contributing too much needed research necessary to bridge the gap between the potential of an active sensor technology and the implementation of deployable systems. The proposed approach is based on combining the use of targets and materials, assessed by full waveform LiDAR, to understand and, consequently, develop the acquisition strategy, processing, and product generation necessary to best exploit the mission. Our objective is to model full waveform LiDAR acquisition parameters designed around various canopy and foliage types (e.g., single to multi- storied canopies, temperate, tropical, sub-tropical) that are of major interest from the Army's operational standpoint. Matching canopy type to LiDAR acquisition would more effectively drive any given sortie and optimize the mission acquisition and support the Army's field operations, including planning, battlefield command and logistics in general.

2. RESEARCH OBJECTIVES

With significant advancements in LiDAR technology, the information content available to applications is rapidly growing. In particular, waveform processing offers a new opportunity for surface material characterization and subsequently object classification. The primary goal of this research project is to analyze the waveform potential with respect to object material identification and classification under various canopy conditions that are important to support the Army's field operations, including planning, battlefield command and logistics. The research objectives span over three major fields, including (1) full waveform LiDAR processing in general, (2) the use of LiDAR-specific targets, and (3) full waveform application in forestry.

The review on current waveform processing methods, LiDAR-specific targets and forestry applications clearly indicates that while research is active in all fields, these works are generally disconnected, and there is rather limited effort devoted to combining these three activities to exploit the full potential of waveform information extraction. The actual objectives are the followings:

1. Characterize LiDAR waveform with respect to ARO-specific requirements, including information extraction in general to support tactical identification, localization, and tracking, and surveillance and reconnaissance.
2. Extend investigation (1) into the use GmAPD sensing (Geiger-mode avalanche photodiode); depending on data availability.
3. Create a material and terrain surface model database to establish empirical or, if possible, analytical relationship to LiDAR waveform; this would be based on analyzing field data, including the use of dedicated targets and reference materials.
4. Develop methods based on (3) to process waveform data in real-time and post-processing mode to support near real time decision-making for the Joint Operating Environment.
5. Provide performance metrics for the waveform-based terrain characterization, including benchmarking of the developed methods and identifying the material and surface classes that can be reliably extracted.
6. Investigate the tradeoff between on-board processing, transmission, centralized processing, and dissemination; develop recommendation for system developments and deployment.

The above tasks include a balanced amount of algorithmic research, initial implementation, testing, data acquisition (jointly, by ARO and other government agencies), data analysis, software developments and technical report preparation. Most of the algorithmic developments are implemented in the Matlab environment, while some programs may be compiled with Microsoft Visual C++ on the Windows platform. The format of LiDAR data includes both

manufacturer-specific as well as the LiDAR data exchange format, i.e., the industry standard LAS format.

3. INCIDENCE ANGLE DEPENDENCE STUDY

This research task is aimed at improving our understanding of the impact of the incidence angle of the laser beam, as it is backscattered from the target, on full waveform data. In addition, a secondary aspect of the study is to investigate the material dependency of waveforms.

3.1 Background

The relationship between transmitted and received photons and the physical environment is described by the following equation:

$$N_s(\lambda, R) = N_L(\lambda_L) * \beta(\lambda, \lambda_L, \theta, R) \Delta R * \frac{A}{R^2} * T(\lambda_L, R) T(\lambda, R) * \mu(\lambda, \lambda_L) G(R) + N_B$$

where $N_s(\lambda, R)$ is the number of received photons from distance R , $N_L(\lambda_L)$ is the number of transmitted photons, $\beta(\lambda, \lambda_L, \theta, R)$ is the volume scatter coefficient at distance R for incidence angle θ , ΔR is the thickness of the range bin, A is the aperture of the sensor, $T(\lambda_L, R) T(\lambda, R)$ is one-way rate of the loss photons while it is transmitted from laser source to target and from target to receiver in distance R , $\mu(\lambda, \lambda_L)$ is the system optical efficiency, $G(R)$ is the geometric factor of the optics and N_B is the photon counts from background radiation. From our perspective, the $\beta(\lambda, \lambda_L, \theta, R)$ part of the equation, called the probability to be scattered, is of importance. The expression is a function of θ , which is the incidence angle, R is the distance between the instrument and the target, λ is the incoming wavelength, and λ_L is the outgoing wavelength. The construction of the equation above suggests that the impact of incidence angle and the intensity of the materials may be detected.

To determine the theoretical impact of the incidence angle on waveform, consider that the distance between the laser source and the target is $R = 300\text{ m}$, the angle between the object and the X axis is $\alpha = 45^\circ$ and the beam divergence is $\mu = 0.3\text{ mrad}$ see **Error! Reference source not found.**. In this special case, when the laser beam is nearly perpendicular to the X axis, the incidence angle is the same as α (for

general case, see Figure 1). Note these parameters reflect the measurement arrangement of the Riegl VZ400 laser scanner, used to collect data for this investigation.

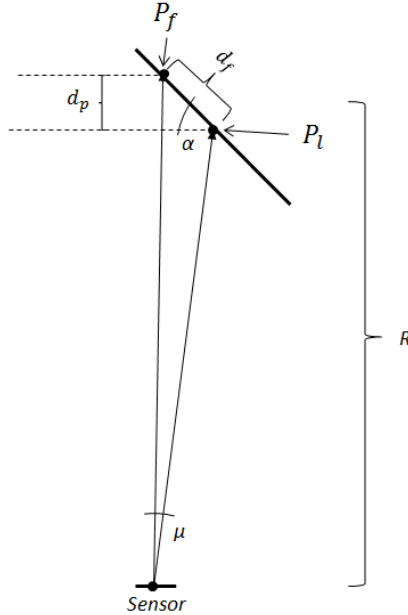


Figure 1 Impact of incidence angle

The first photons are scattered back from point P_f , while the last ones come back from point P_l . Since the backscattering takes more time than the pulse width, by T , the resulting waveform is stretched. The footprint of the laser beam in R distance is:

$$F \approx \mu R = 0.3 \text{ mrad} * 300 \text{ m} = 9 \text{ cm}$$

If the shape of the transmitted waveform was a Gaussian-like function, after the backscatter, the width of the function, at least, must have increased. The quantitative value of this change can be easily calculated. The geometrical distance between points P_f and P_l in Y-axis direction is:

$$d_p = \cos(\alpha) * F = \sin(45^\circ) * 9 \text{ cm} = 6.36 \text{ cm}$$

The waveform is a function of the time, thus to determine the travel time of the pulse on the T distance is:

$$2 * \Delta t = \frac{d_p}{c} = 2 * \frac{6.36 \text{ cm}}{299\,792\,458 \text{ m/s}} = 0.42 \text{ ns}$$

Since the pulse travels forth and back, there is multiplication by 2. When the laser beam is perpendicular to the target surface, the incidence angle is close to zero. **Error! Reference source not found.** for the changes of width as the function of incidence angle in the left side and the shapes of waveforms in different incidence angles. Figure 2b clearly shows that for the relatively short range and laser beam narrow convergence angle the impact is small.

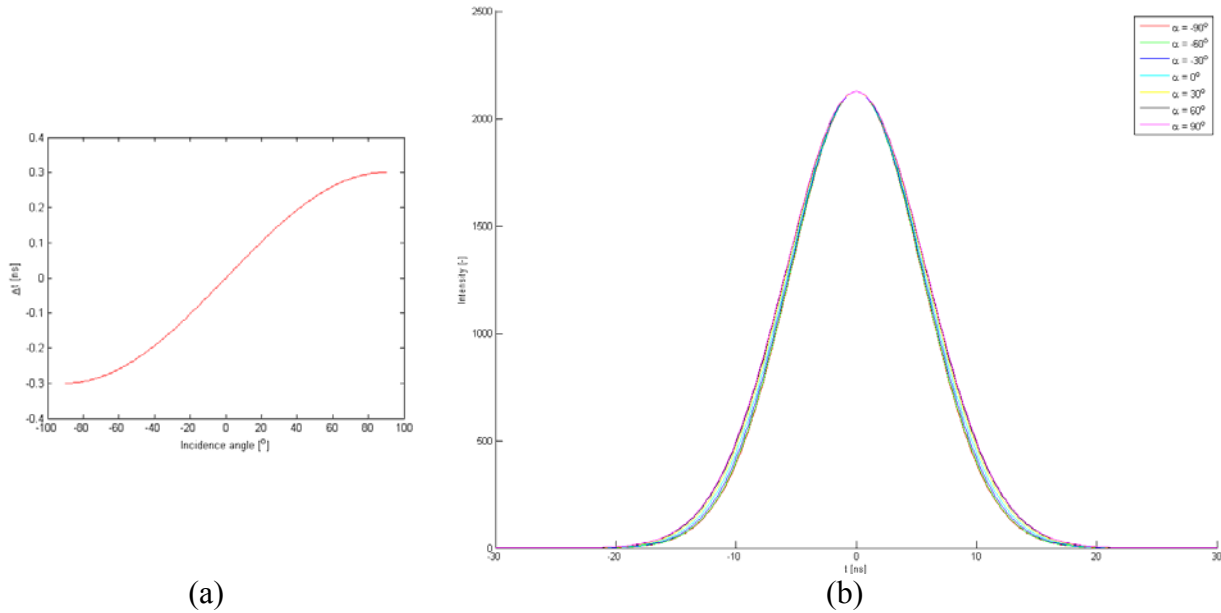


Figure 2 Time delay as a function of the incidence angle (a), and changes of the shape of the Gaussian waveform due different incidence angles (b)

3.2 Test Dataset

In cooperation with the USACE ERDC Remote Sensing and Fluorescence Spectroscopy Lab, a data collection campaign was conducted at the OSU West Campus on October 15, 2012. The OSU GPSVan was outfitted with different targets and the Riegl VZ-400 laser scanner of the USACE ERDC mobile measurement system was acquiring laser data in different configurations; vehicles and scanner are shown in Figure 3. The geographical location of the field survey is shown in Figure 4. The laser surveys included three areas with four data collections, as listed in

Table 1 and shown in Figure 4; the target-based data collection was interrupted by rain, so the data for the targets was acquired in two sub-sessions. Besides the usual system check, the shakeup test provided a short range survey of the targets on the GPSVan, see Figure 5. ScanPos2

and ScanPos3 datasets contain the measurement from different types and orientations of the target discs. Finally, ScanPos4 includes scans from two different types of building: a parking garage with horizontal extent and an office building with more vertical extent. In these cases the walls of the building is considered for analyzing the impact of the incidence angle.



(a)



(b)

Figure 3 USACE ERDC mobile measurement system with Riegl VZ-400 laser scanner (a) and OSU GPSVan with targets (b)

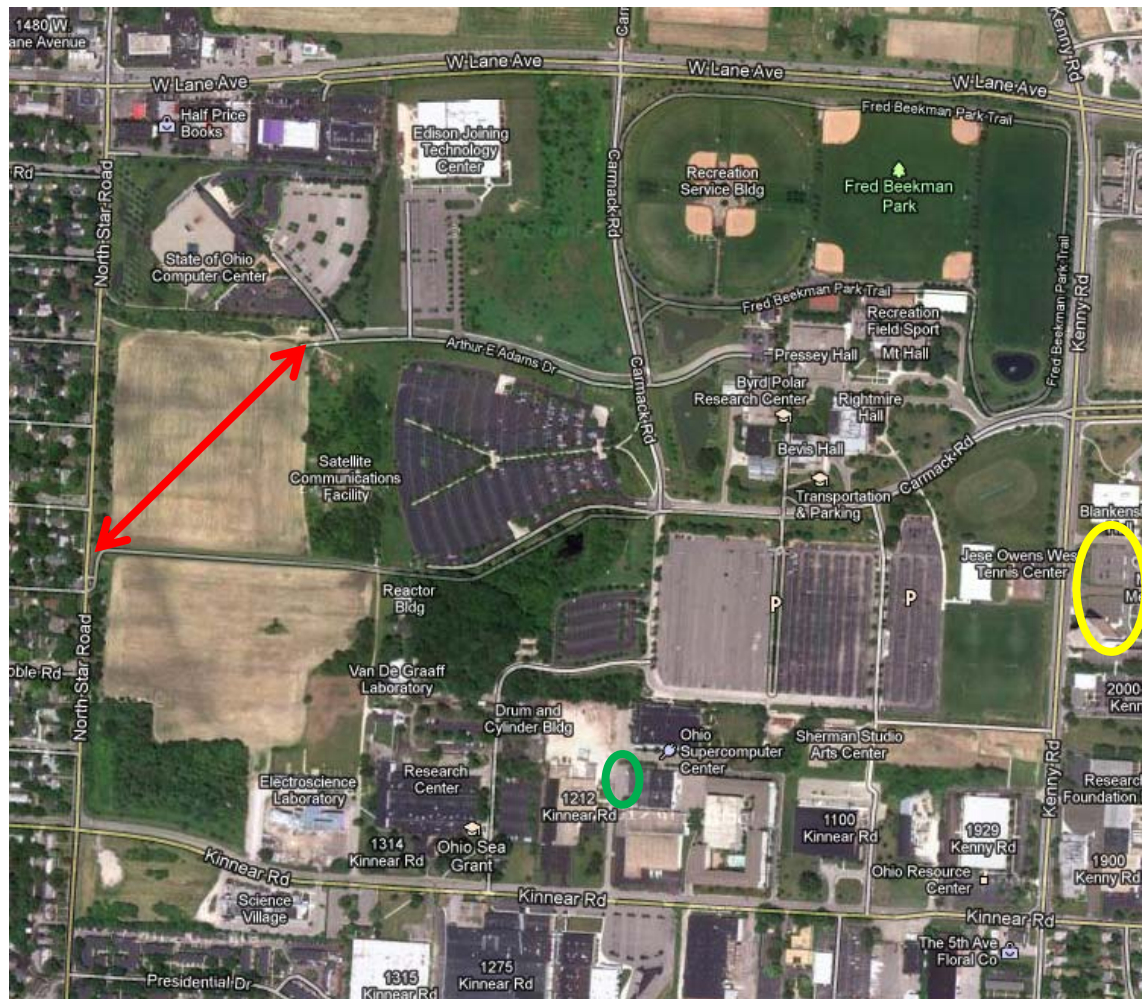


Figure 4 Field survey locations, OSU West Campus; shakeup area is marked in green, survey range with targets is marked by red line, and survey of man-made objects area is marked by yellow

Table 1 Description of the datasets

Name	Description	Time (EST)	Marked
ScanPos1	Shakeup test at CFM	13:45:29 – 13:50:39	Green
ScanPos2	Surveying disc targets (session 1)	14:31:54 – 14:54:41	Red
ScanPos3	Surveying disc targets (session 2)	17:20:19 – 17:55:31	Red
ScanPos4	Surveying buildings	18:17:19 – 18:18:43	Yellow

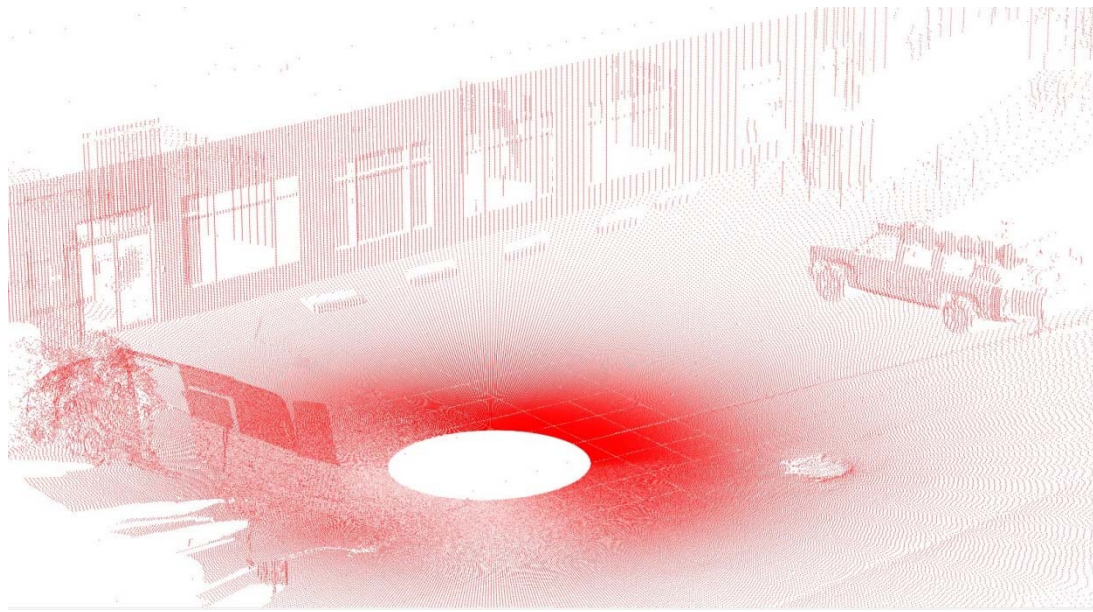


Figure 5 Shakeup are point cloud

The circular targets installed on the GPSVan were covered by six different materials to support the investigation of waveform dependency on physical properties. The different coatings are shown in Figure 6, and they represent several materials of interest.

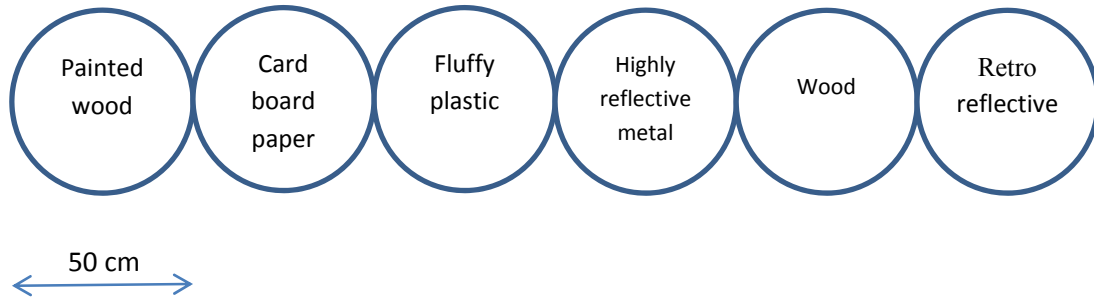


Figure 6 Target materials

The data preprocessing primarily included the extraction of all the relevant information to waveform from the raw measurement files. The direct access to the data was provided through the Riegl software toolkit, RiWaveLib library. Note USACE ERDC provided all the raw measurement files as well as the point clouds in LAS format later. In addition, the GPSVan location and orientation was computed to provide accurate georeferencing for the targets. The overall workflow of this preprocessing is shown in Figure 7.

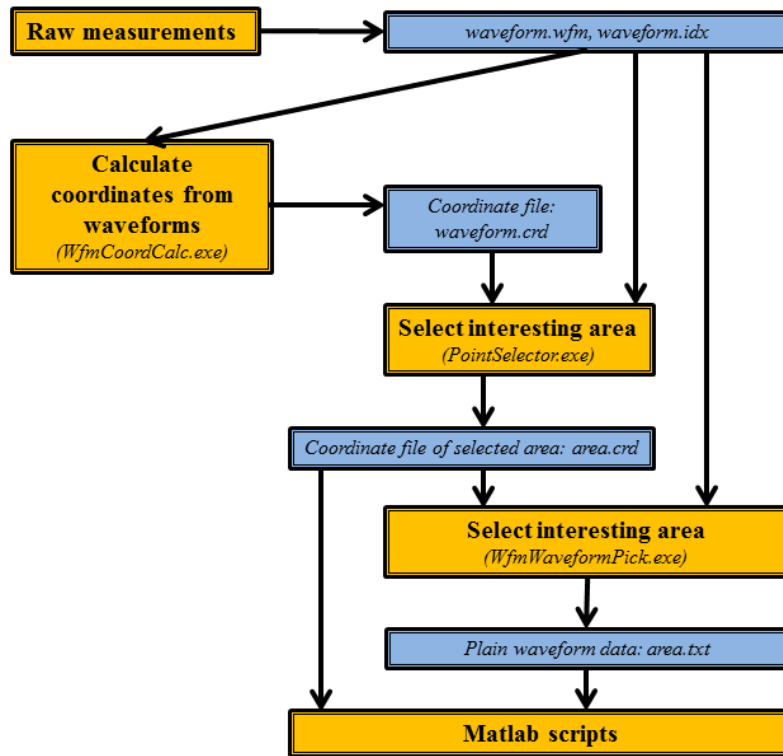


Figure 7 Workflow of the raw data processing

WFM files and the index files are provided from the measurements, and the coordinates of the points can be calculated with the *WfmCoordCalc* program developed by OSU. The Riegl VZ-400 scanner uses low and high channel units for digitizing the waveforms, and, thus, waveforms from the WFM files are derived from low or high or both channels. In our data processing, first the low level channel is used when available. If only the high channel is available, the high channel intensities are converted to low channel intensities. For this reason, the gain between the two channels had to be determined, and thus this function can be used to convert from high channel to low channel intensity. Note that Riegl provides no information on the relation between channel intensity values. Based on test data, linear regression between the relative gain and high channel intensity was established, as shown in Figure 8a. In the subsequent processing, the following equation was applied for scaling the high channel intensities to low level intensity domain:

$$I_{low} = \frac{I_{high}}{0.006781497 + 0.000240794 * I_{high}}$$

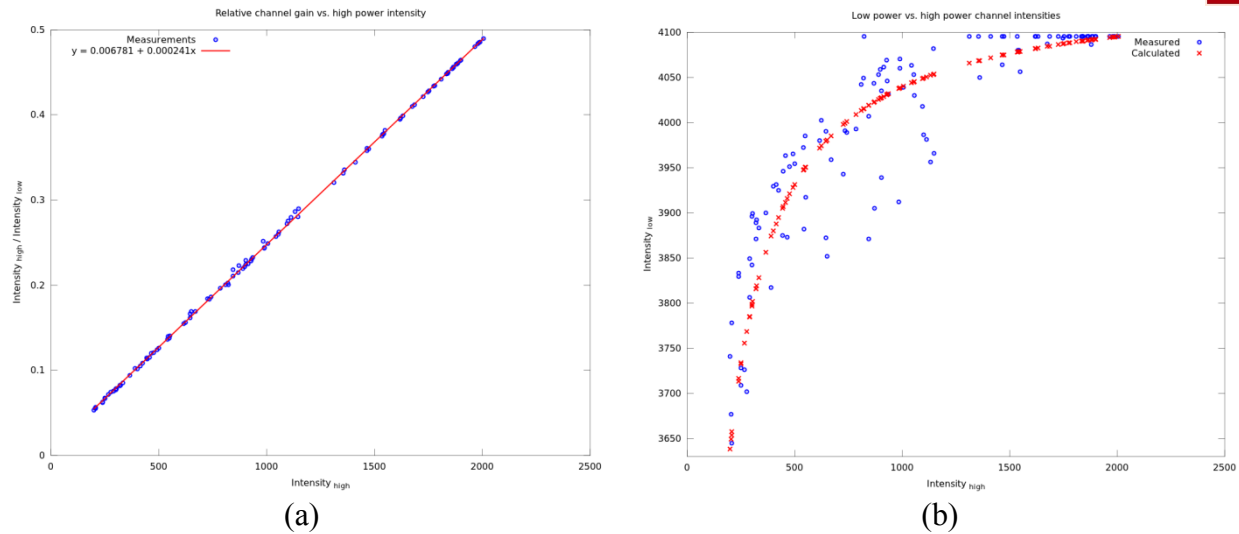


Figure 8 Relative channel gain and high channel intensities (a), actual and computed low and high channel intensities (b)

The differences between the measured and computed intensities can be seen in Figure 8b. Note that the fitting is not satisfactory enough, and, thus, this determined correlation was only used for the coordinate calculation, and it was not directly applied to the processing of waveform intensities. In the subsequent calculations, as mainly low channel we used, though the coordinate calculation high channel data was also used after transformation. After finishing coordinate calculation, the CRD file contains the coordinates of the waveforms.

3.3 Processing ScanPos1 and ScanPos2 Datasets

The GPSVan, equipped with six target discs, see Figure 3b, was positioned at a distance from the Riegl VZ-400 station of about 330 meter. Unfortunately, the digitizer uses a 2 ns sampling rate that is below of the normal 1 ns value, widely used in airborne LiDAR, making the measurement of the impact of the incidence angle on waveform difficult. The targets were scanned in 11 different orientations of the van, representing a broad range of the angle of incidence. Note the laser scanner station was in a fixed position during the scans and only the van did move to change orientation. The intensity values of a sample point cloud obtained from the targets at close to zero incidence angle is shown in Figure 9. While keeping the vehicle center at the same location and just changing the orientation of the van was attempted, there was a minor deviation in the vehicle center as shown in Figure 10.

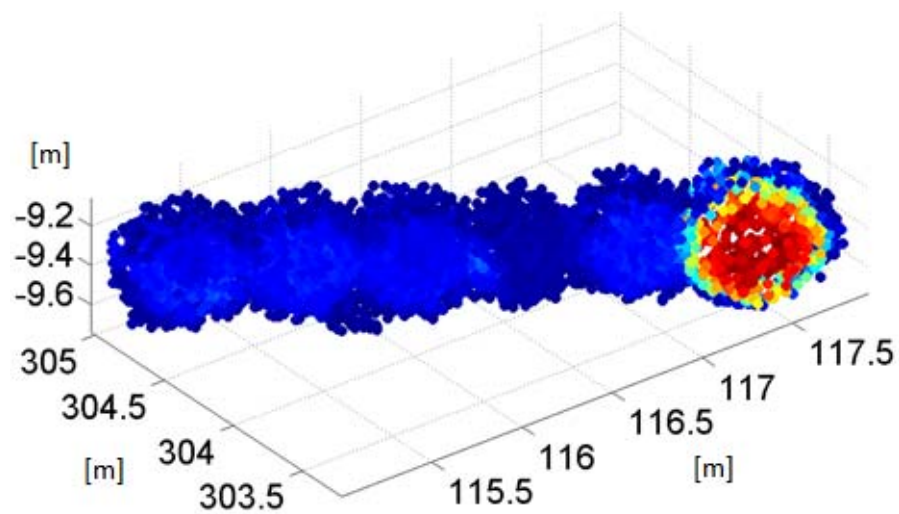


Figure 9 Intensity values at near zero incidence angle

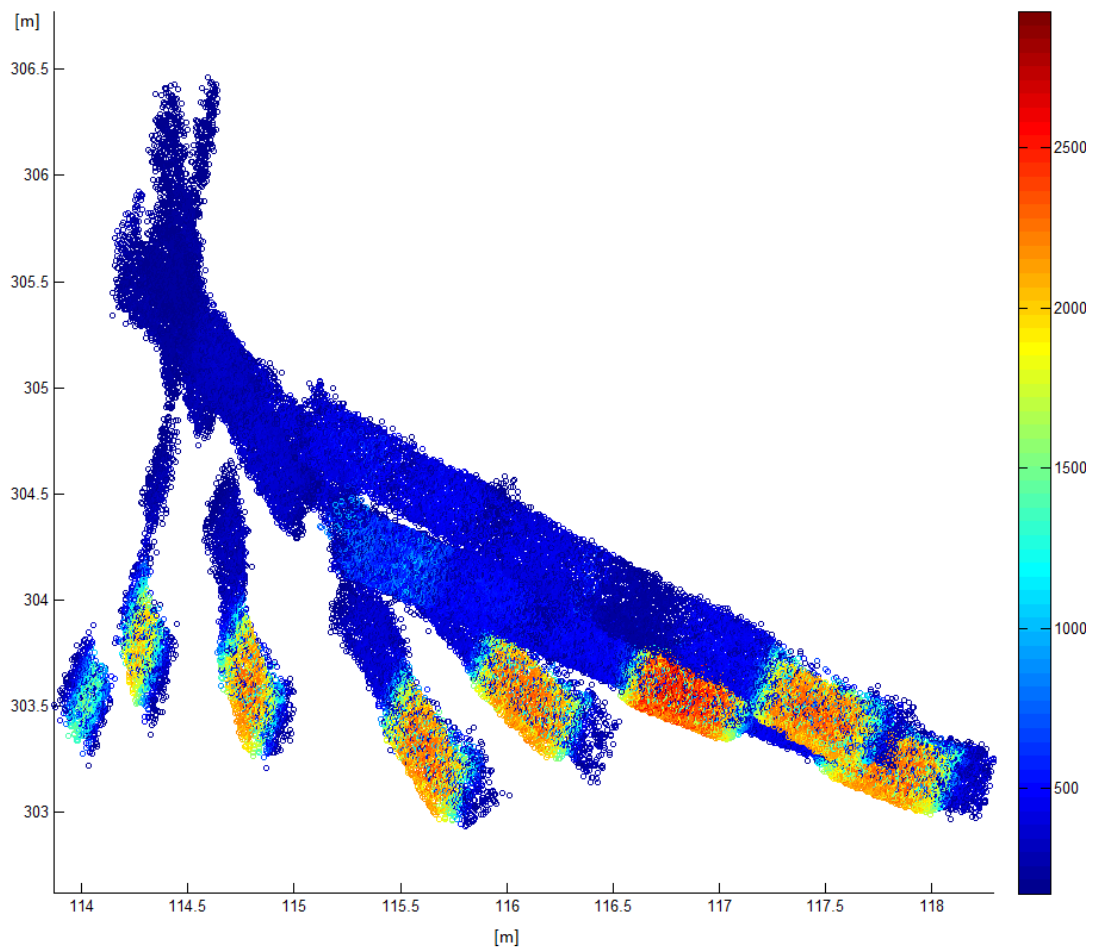


Figure 10 Various positions and orientations of the van in the XY plane

Though the GPS/IMU system of the van provided highly accurate georeferencing for the targets, as a test, the directions of the discs, i.e. the van orientation, was also determined from measured point cloud. In this exercise, two methods were used: (1) grouping, and (2) eigenvector based solution. In the case of grouping method, the dataset is divided into two parts by the indexes of the point, and then the angle between the two centers of the groups is determined in the XY plane, defining the direction of the van. The eigenvector based method first computes the covariance matrix, and then solves for the eigenvalues. The direction of the greatest eigenvalue approximates the direction of the van, which is identical to line defined by the targets. The overall results with remarks are listed in Table 2. Note that in most cases, a 180 degree difference can be detected between the grouping and the eigenvalue solutions. This is caused by the fact that the direction of the largest eigenvector shows the major extension of the point set, while the direction obtained by the group method depends on the direction of the scan. With the center point of the point cloud of the targets and the direction of the targets, the incidence angle can be easily calculated; Figure 11 shows the principle of the calculation.

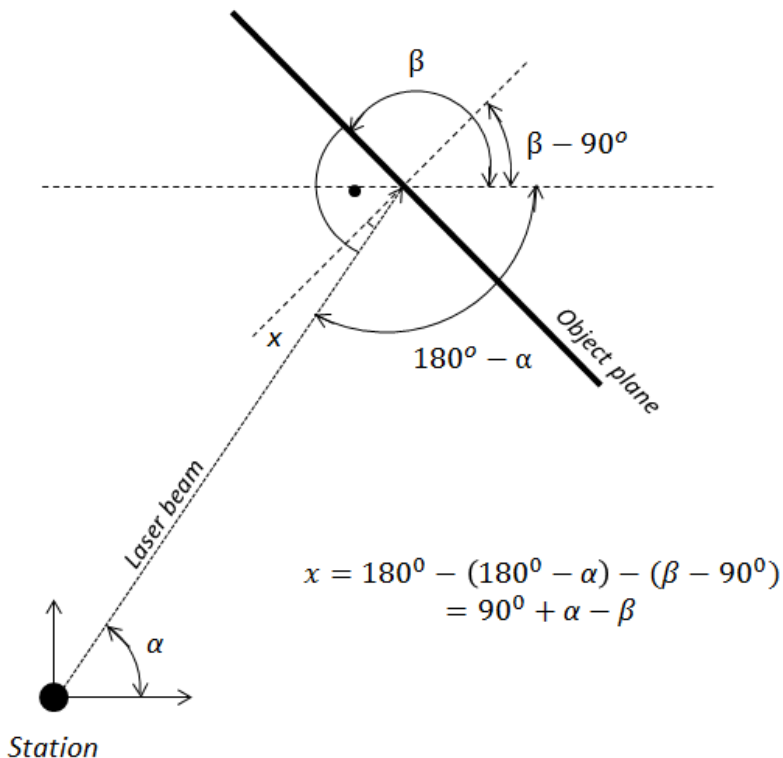


Figure 11 Calculation of the incidence angle

Table 2 Direction of the disks, determined from measurements

ID	Solution from group method [degree]	Solution from eigenvector method [degree]	Final direction (β) [degree]	Angle of center (α) [degree]	Angle of incidence (x) [degree]	Ori-en-tation	Remarks
172120	-30.1	149.7	149.7	69.0	9.3	\	Few points
172411	151	150.9	150.9	69.1	8.2	\	
172807	-28.8	151	151	69.0	8	\	
173132	133.9	133.5	133.5	69.3	25.8	\	A disk from the center is missing
173523	-61.1	118.6	118.6	69.3	40.7	\	A disk from the center is missing
173842	99.1	98.9	98.9	69.4	60.5		A disk from the center is missing
174216	83.7	-96.2	83.8	69.4	75.6		
174655	83.3	76.4	76.4	69.4	83.0	/	Large difference of the solutions
175044	-22.5	157.7	157.7	69.0	1.3	\	
175325	167.4	69.7	69.7	69.0	89.3	/	Very few points, large difference of the solutions
175531	-22.5	157.7	157.7	69.0	1.3	\	

3.3.1 Point filtering

The point filtering was used to determine the points backscattered from each disk. Since the target disks are in a plane, positioned slightly in front of the van, the point cloud can be easily thresholded to an envelope containing all the points of the six targets. Also, the gaps between the disk can be used to separate the initial point cloud into six groups. Next, fitting planes are calculated for all the six targets. In the datasets the standard deviation of the distances from the plane was ~6-8 cm, and then those points are selected which are within that distance from the fitting plane. After filtering, these points are rotated to the XZ plane, as shown in Figure 12. Filtered points on the fitted plane are shown in Figure 13. The points, which lie within 0.25 m (that was the radius

of the discs) from the center, are selected and they are subject of all the subsequent analysis, as there is a high confidence that these point are from the target disc.

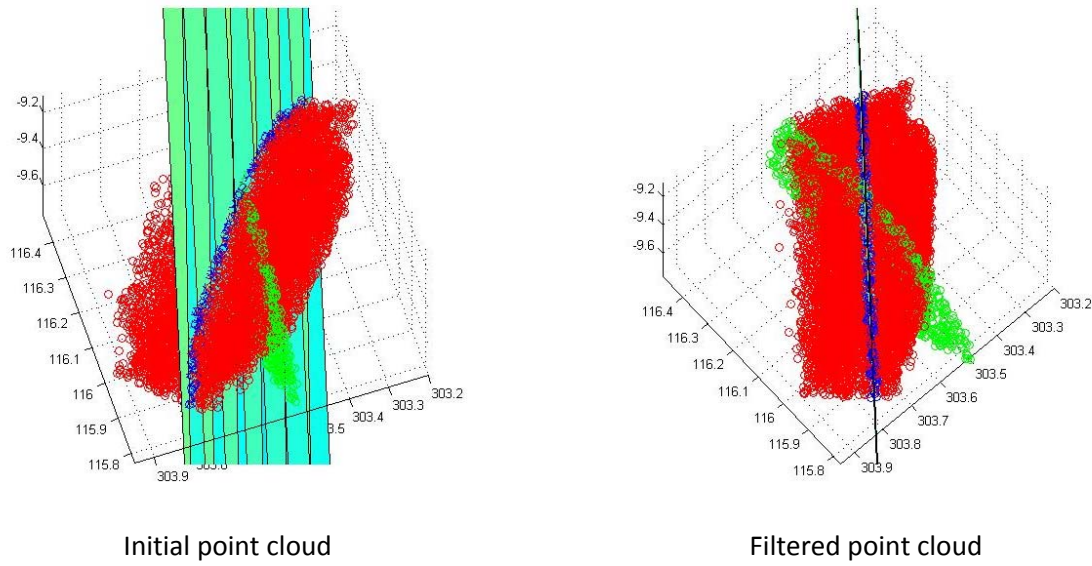


Figure 12 Point cloud of a disk target (red) with fitting plane, points within 1 cm distance from plane (blue), points after rotation to XZ plane (green)

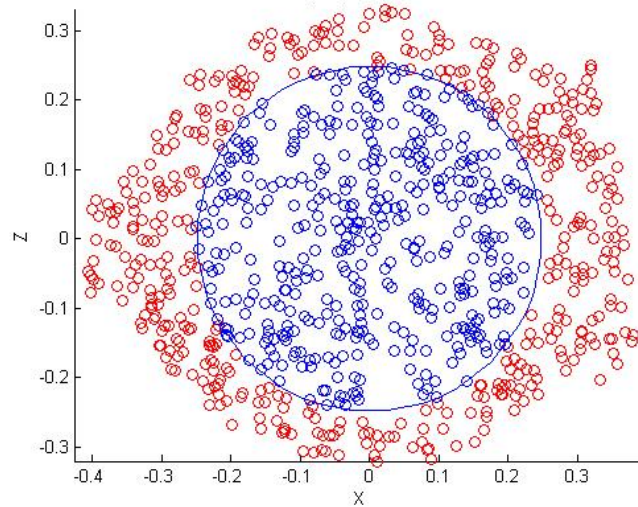


Figure 13 Points within 25 cm from the center

3.3.2 Basic characterization of waveform groups

The visualization of the waveforms from the six targets is provided in Figure 14. Note that the materials with strong reflective properties can easily differ from the ones with non-reflective properties. Other material properties cannot be recognized, and thus, suggesting that materials should be classified by reflectivity on this dataset. Consequently, the materials can be grouped by reflectivity; using three classes, the materials are grouped, as listed in Table 3.

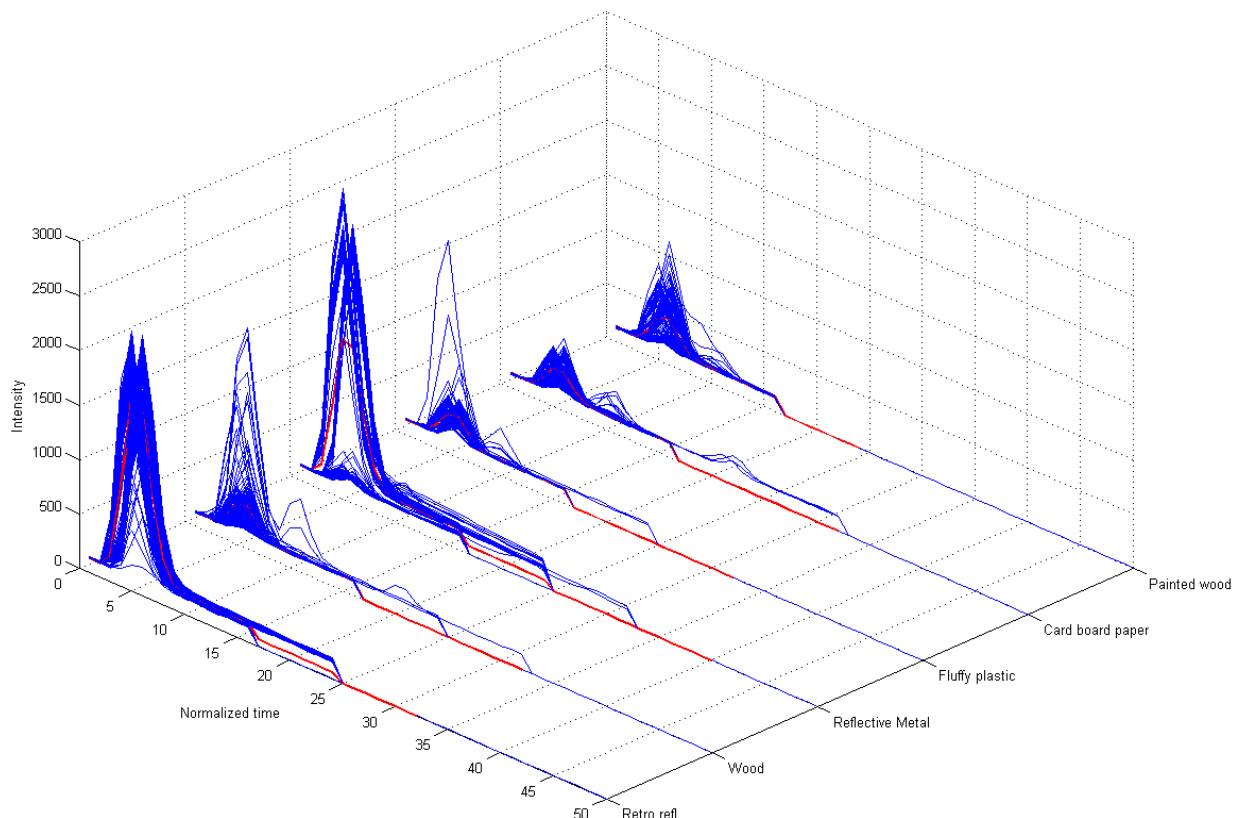


Figure 14 Full waveforms grouped by materials (blue), and average waveforms (red)

Table 3 Coarse target reflectivity grouping

Material	Class by reflectivity
Retro reflective	1
Wood	3
Reflective metal	2
Fluffy plastic	3
Card board paper	3
Painted wood	3

Waveforms from all groups with respect to the incidence angle are visualized in Figure 15. Notice that target 3 is not used in this analysis, as the highly reflective metal material has a mirror-type of reflection; no returns exist if there is any incidence angle. Figure 16 illustrates incidence angles where no data available from target 3 (marked by red circle).

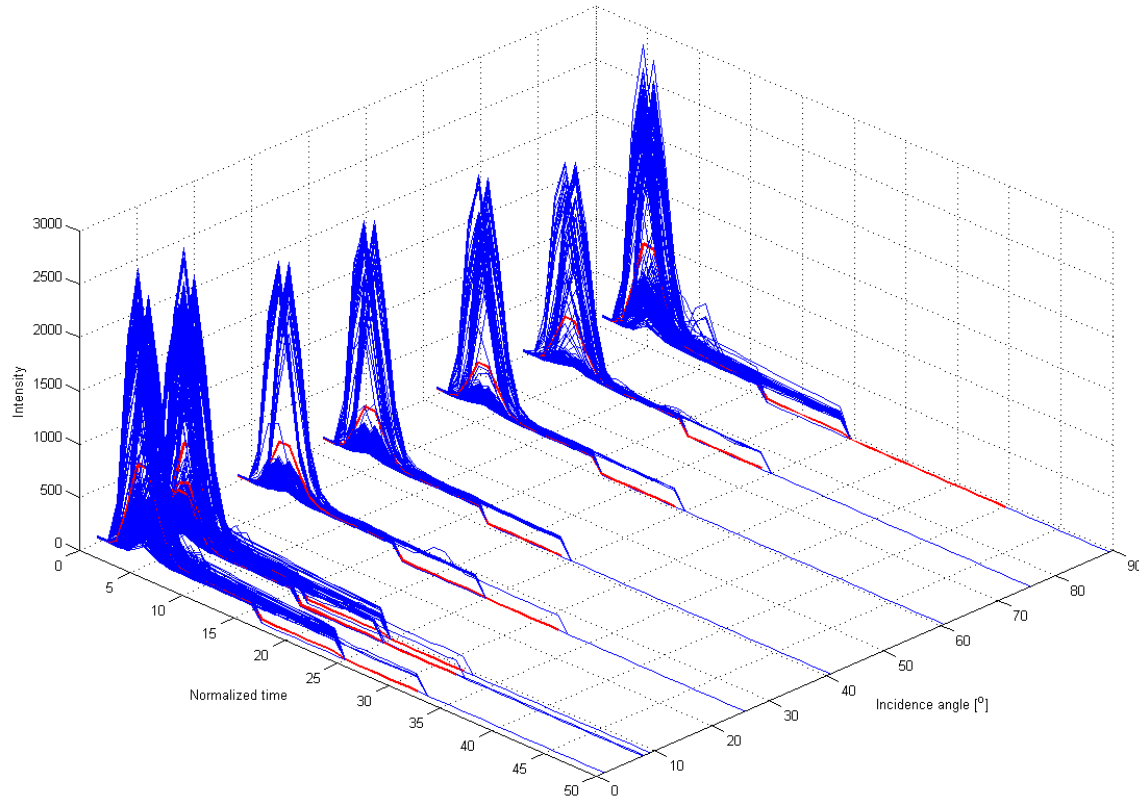


Figure 15 Full waveforms from all targets grouped by incidence angle (blue), and average waveforms (red)

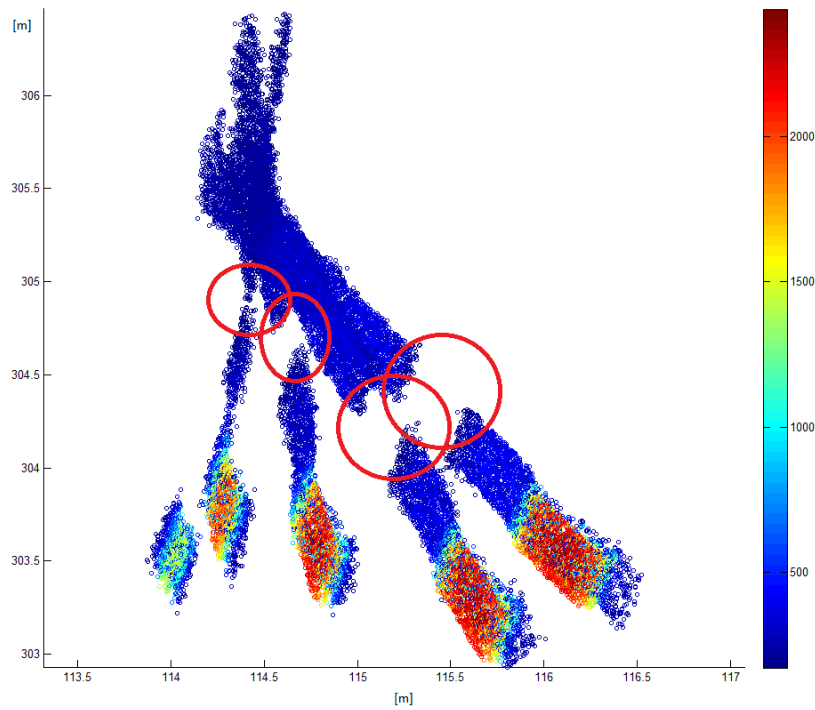


Figure 16 Directions illustrating when no waveforms are obtained from target 3 (highly reflective metal)

3.3.3 Gaussian waveform decomposition

Gaussian waveform decomposition is the most widely used waveform processing method. The idea is that if the outgoing laser pulse has a Gaussian shape, then the backscattered pulse should have similar shape too. Or for sparse vertical structures, such as vegetation, the returning waveform is composed of several reflections, and thus the waveform is the sum of several pulses of Gaussian shape. Once the waveform is decomposed, all the shapes will represent an object surface/boundary, and, in addition, the shape parameters can be used for further investigation, such as correlation the surface geometrical or material properties. Since the outgoing pulse is rarely of perfect Gaussian shape, and during the backscattering the shape of the reflected pulse can be distorted, generalized Gaussian shapes are frequently used in waveform processing. In theory, the shape of the outgoing pulse can be used for decomposition, which leads to an ill-posed deconvolution. In this investigation, a generalized Gaussian shape model is used, as described by the following equation:

$$f(x) = mi(m) \left[\frac{\text{atan}(a(x-t))}{\pi} + \frac{1}{2} \right] e^{-\frac{|x-t|^b}{s}}$$

where t (time) is the translation of the function, a is the skewness parameter, b is the flattening, s is the width (i.e. the sigma), $mi(m)$ is the scaling variable (the magnitude of the function). Figure 17 show example of shape functions with various parameterization.

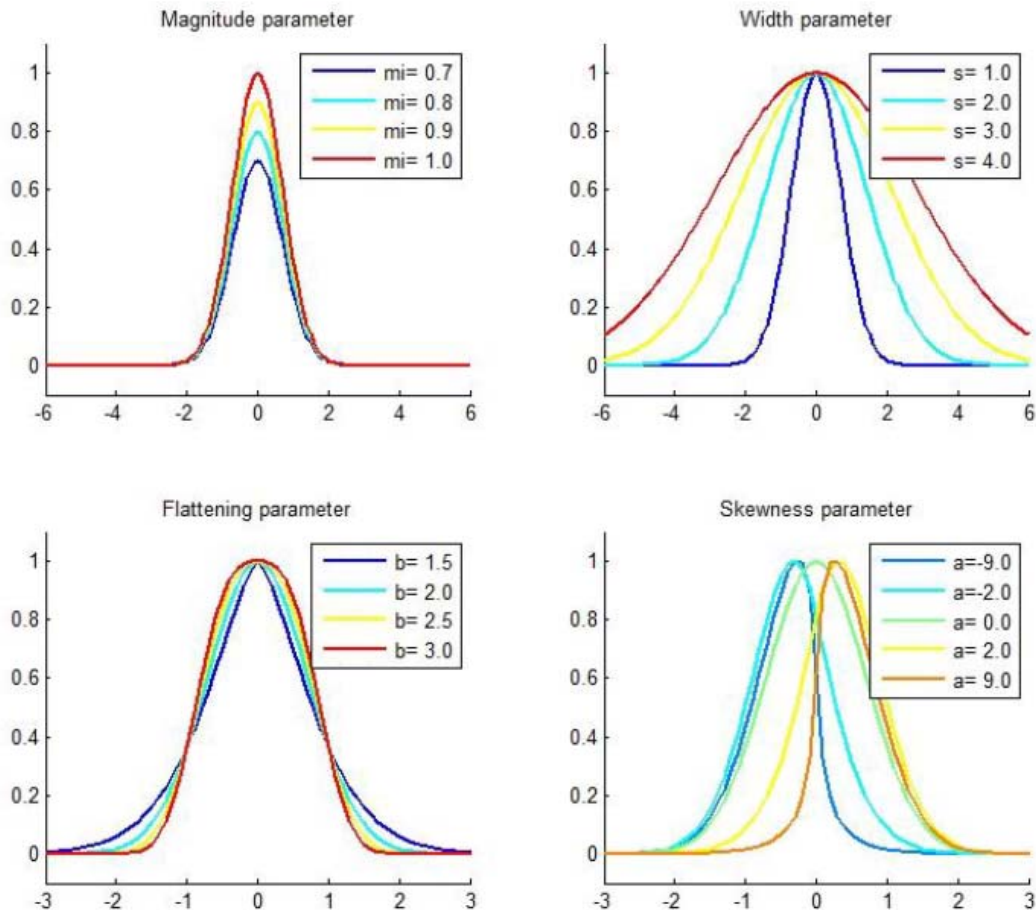


Figure 17 Generalized Gaussian shape functions

The result of a typical waveform fitting is shown in

Figure 18. The discrete full waveform data is represented by a polyline marked with blue color. Note that in our tests, hard surface targets were used, so only single returns are expected. In fact, the multiple peak waveforms, very rare cases, were filtered out during processing. For the parameter estimation, the least squares method was used; the fitted Gaussian shape is shown in green in

Figure 18. The quality of the fit was also checked and the cases, where the fit was unsuccessful or of poor quality, i.e., the fitting parameter, the norm of the residuals of the regression, was larger than 10, were removed.

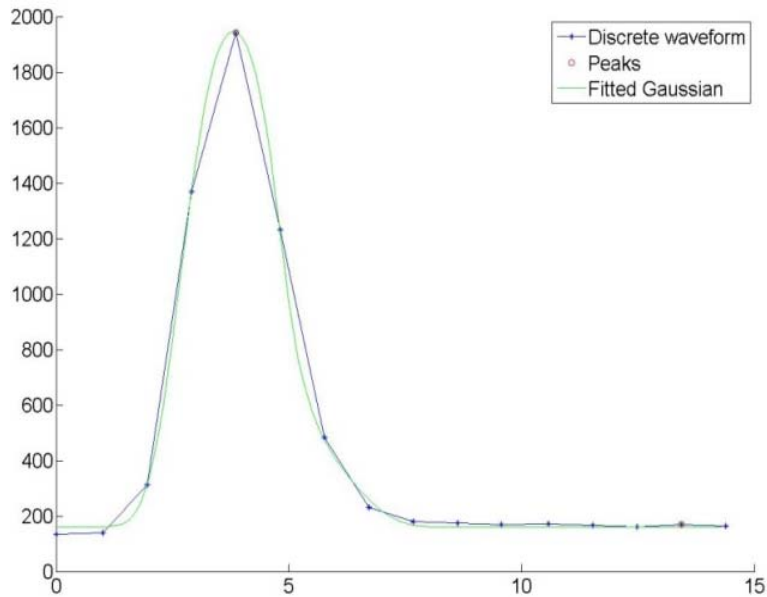


Figure 18 Fitting Gaussian shape to a typical waveform

The generalized Gaussian shape parameters were determined for each waveform, and the statistics for the five target groups with different incidence angles were computed. Figure 19 lists the results for all the fitting parameters for each target with all incidence angles. In addition, the number waveforms as well as adjustment quality parameters are also included. The small circles show the mean of the parameter values, and the vertical lines indicate the standard deviations.

To identify trends, a 2nd order polynomial regression was applied to the datasets; these curves are also shown in Figure 19, and the norm of the regression residuals is listed in the titles of each figures. Clearly, there is a visible difference between the highly-reflective and normal reflectivity targets; though, no obvious trend can be observed. Removing the retro-reflective target group, Figure 20 shows the statistics, allowing for better differentiation of targets with normal reflectivity. Visibly, the fitted polynomials look more attractive, but the residuals are also noticeably large.

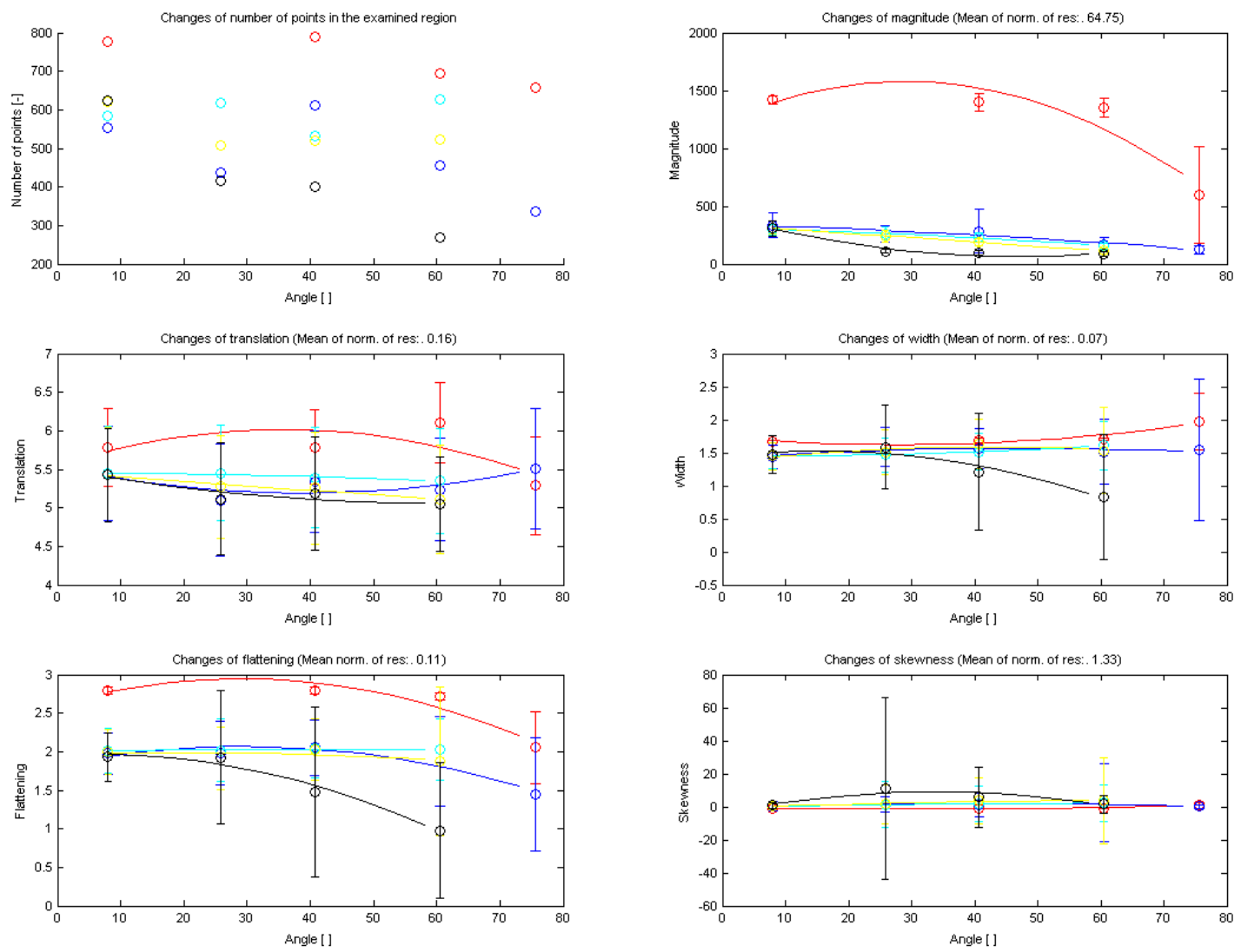


Figure 19 Gaussian fitting parameters as a function of incidence angle, grouped by the five target materials (red: retro-reflective, blue: wood, cyan: fluffy plastic, yellow: cardboard, and black: painted wood)

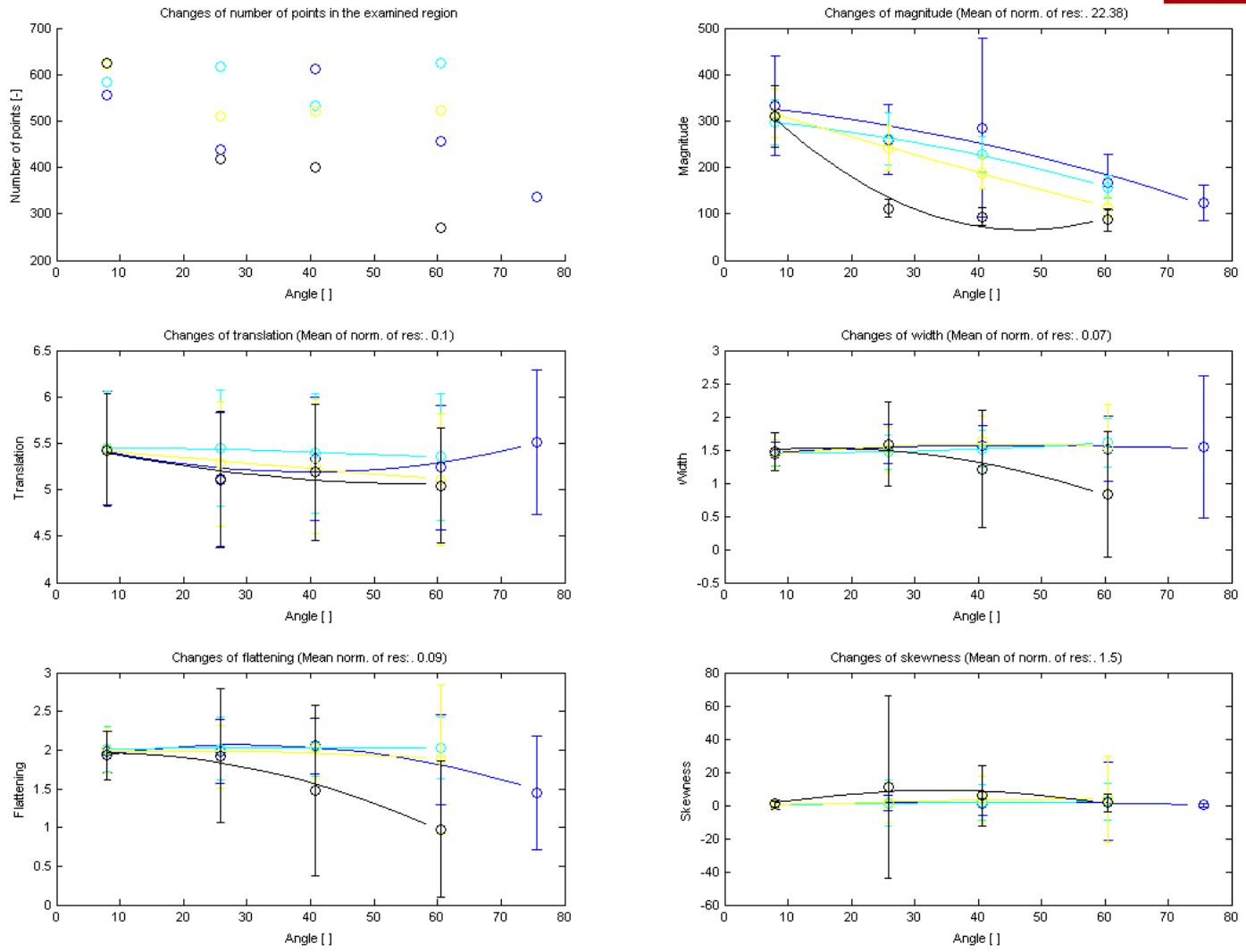


Figure 20 Gaussian fitting parameters as a function of incidence angle, grouped by the four target materials (blue: wood, cyan: fluffy plastic, yellow: cardboard, and black: painted wood)

3.3.4 Incidence angle estimation with feed forward neural network

Since there is no obvious analytical model for the incidence angle estimation from decomposed waveform parameters, a neural network based approach was selected, where by learning, the classifier parameters can be determined. Feed forward (FF) neural network is a basic network type that can be a good choice for classification, pattern recognition and several other problems. In our investigation, the network was trained for estimating the incidence angle. In neural network applications, one of the first questions is the complexity of the network, such as the number of hidden layers, the number of neuron, etc. The selection is mostly done empirically,

based on testing with various data. Another question is the input and/or the selection of parameters derived from the input data. In our case, we decided to apply the more generic approach of directly using the waveform, i.e., the intensity vectors, as it potentially allows for better performance by using all the information in the data. The output of the network is one variable that is the estimated incidence angle.

To train a neural network, the dataset is generally divided into two parts: training set and validation set. Following general practice, the training set contains every waveform with odd numbers from the dataset while waveforms with even numbers form the validation set. The aim of this selection methodology is to provide consistent data in the training and validation set. For training the neural network, the Levenberg-Marquardt algorithm was used. After the training, the network was checked on the validation set. The incidence angles for elements in the validation set are known, thus the “must” and “is” value can be compared as the residuals of the system model. In addition, the mean and the standard deviation of the residuals are also calculated.

Table 4 shows the results of the feed forward network applied only to the retro reflective target dataset. Note that as the number of neurons is increasing the mean of the deviation becomes worse. This is caused by over-fitting or over-learning. In the table, the best configuration is the {4, 2, 1} alignment, and for that case various waveform sizes are analyzed; the cut-off value in the table shows the number of waveform element used in the process, for instance, the value of 16 means that the first 16 intensity values are the input of the neural network. The table shows that no significant differences between the cut-off values of 16, 32, and 50, suggesting that the first 16 intensity values contain most of the information about the waveforms, as expected.

Table 4 Feed forward neural network for incidence angle determination for the retro reflective target

	Hidden layer(s)					
	{6, 3, 1}	{14, 6, 1}	{4, 2, 1}	{4, 2, 1}	{4, 2, 1}	{4, 2, 1}
Input neurons' activation function	tangent sigmoid					
Hidden neurons' activation function	tangent sigmoid	pure linear				
Output neuron's activation function	tangent sigmoid					
Cut off [-]	16	16	16	32	50	16
Norm of residuals [°]	298.5	498.0	240.5	248.3	252.0	301.0
Mean [°]	0.3	2.2	0.4	0.3	0.3	0.5
Standard deviation [°]	9.1	15.1	7.4	7.6	7.7	9.2

The results of neural network on the whole dataset (including all targets) is shown in

Table 1. Note that changing the cut-off edge value has practically no impact on the results. Not surprisingly compared to the retro target case, a different network structure provides the best solution, resulting in a mean value of 0.1 degree and standard deviation of 11.7 degree. To assess this performance in absolute sense, the coarse sampling rate (2 ns), the relatively short object distance, and the small footprint should be taken into account, and under these conditions, the 10 degree variance is a good and realistic value.

Table 5 Feed forward neural network for incidence angle determination for all the targets

	Hidden layer(s)				
	{4,2,1}	{4,2,1}	{4,2,1}	{14, 6, 1}	{6,3,1}
Input neurons' activation function	tangent sigmoid				
Hidden neurons' activation function	tangent sigmoid	tangent sigmoid	pure linear	tangent sigmoid	tangent sigmoid
Output neuron's activation function	tangent sigmoid				
Cut off	50	16	16	16	16
Norm of residuals [°]	856.9	955.3	918.1	867.2	572.9
Mean [°]	-0.0	0.1	0.5	0.2	0.1
Standard deviation [°]	12.2	13.6	13.1	12.4	11.7

3.3.5 Surface material classification based on waveform data

In this task, a basic investigation was carried out to identify potential correlation between waveform shapes and object materials. The waveform vector is defined as

$$w = \{I_{t_1}^w, I_{t_2}^w, I_{t_3}^w, \dots, I_{t_n}^w\},$$

where w is the waveform, $I_{t_i}^w$ is the intensity at the time moment t_i in waveform w . Given that the number of intensity values of the two waveforms w_1, w_2 is the same (i.e., same length) and the sampling rate is identical ($t_i^{w_1} = t_i^{w_2}$), the distance between two waveforms can be defined as:

$$d(w_1, w_2) = \sum_{i=1}^n |I_{t_i}^{w_1} - I_{t_i}^{w_2}|.$$

Similarly to incidence angle estimation, the dataset is divided to learning and validation system. From the learning dataset the average waveform is calculated for each target as:

$$\hat{I}_{t_i} = \frac{\sum_{j=1}^m I_{t_i}^{w_j}}{m},$$

where m is the number of the full waveforms. The average waveforms are determined for each reflectivity class. Then the classification is based on calculating the distance between an incoming waveform and the average waveforms, and then the nearest one will determine the reflectivity class of the income waveform:

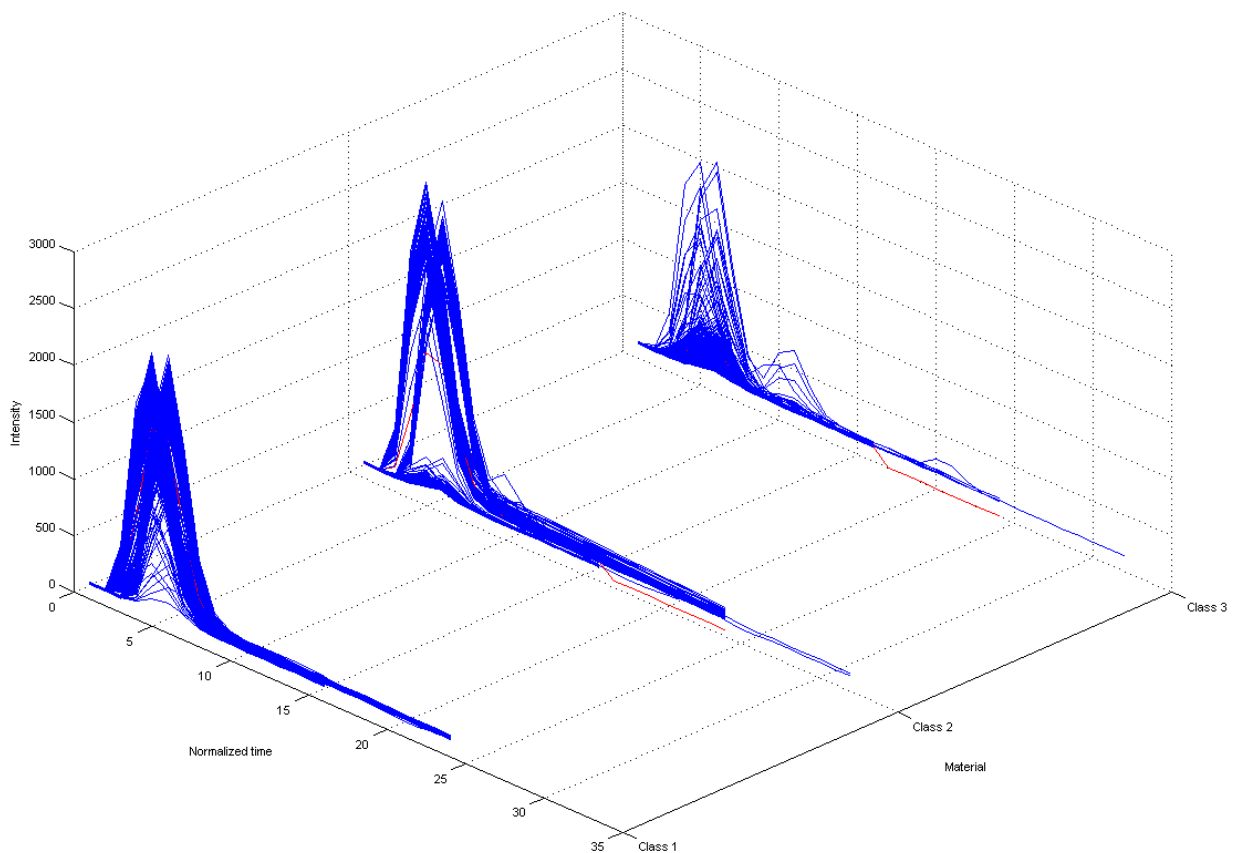
$$\min_c d(w_{income}, \hat{w}_c),$$

where c is the class of reflectivity, w_{income} is the incoming waveform, and \hat{w}_c is the average waveform of the reflectivity class c . To assess the performance, the algorithm was tested on the validation set and the results are listed in Table 6.

Table 6 Classification results for three classes

Reflectivity class	Success rate
1	87.8 %
2	0.5 %
3	99.2%
Overall	84.5%

Clearly, Class 2 shows an unacceptable performance, which may be somewhat related to the small number of waveforms from target 2, see Figure 21. Note that the shape of the class 2 is halfway between classes 1 and 2.

**Figure 21 Waveforms shapes of in the three classes**

Merging classes 2 and 3, the results are shown in Table 7; the success rate of the class 1 slightly decreased, but the overall rate increased.

Table 7 Classification results for two classes

Reflectivity class	Success rate
1	79.9 %
2	99.6 %
Overall	93.1%

3.4 Processing ScanPos4 Dataset

The aim of this investigation was to use vertical and horizontal walls to estimate the incidence angle. For this reason, an area with tall buildings was chosen; see Figure 22(a) for the scanned area. For the vertical analysis, a parking garage was selected (Building I, Figure 22 (b), and Figure 22 (d)), and an office building was the object with some measurable height dimension (Building II, Figure 22 (c), Figure 22 (e)). In the case of the office building, trees hide the lower part of the building, and were subsequently removed (Figure 22 (e)). The points of the front wall was used for data analysis (Figure 22 (g), Figure 22 (h)).



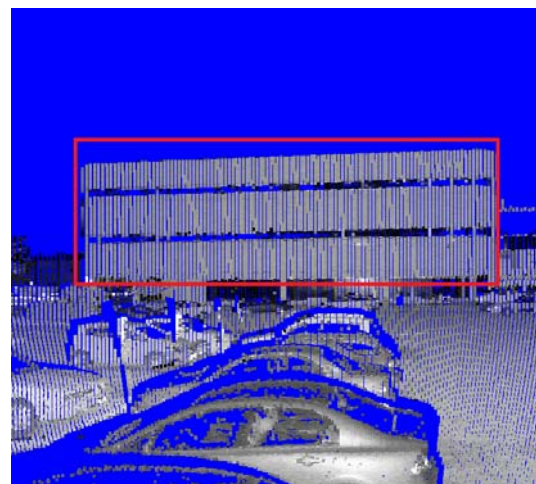
(a) Area of scan



(b) Building I (parking garage)



(c) Building II (office building)



(d) Point cloud from Building I



(e) Point cloud from Building II



(f) Point cloud from Building II after cleaning

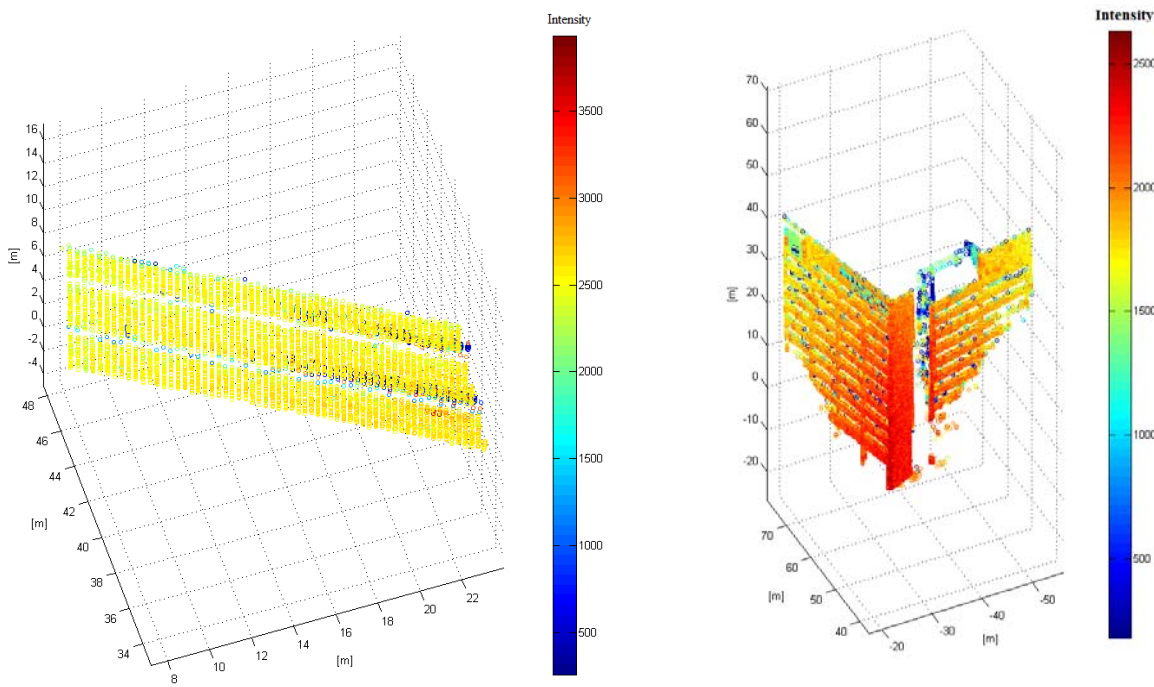


Figure 22 Buildings used in investigation

In the case of Building I., the angle of the surface (i.e. wall) is constant, thus the incidence angle only depends on the angle of laser beam. The angle of the wall that it close with X-axis of the coordinate system of the instrument was 148.60 (reverse clockwise). The intensities of points are also same. The limits of scanned angle were between 75 and 88 degree on vertical plane and between 56 and 81 degree on horizontal plane. The waveforms can be seen in Figure 21.

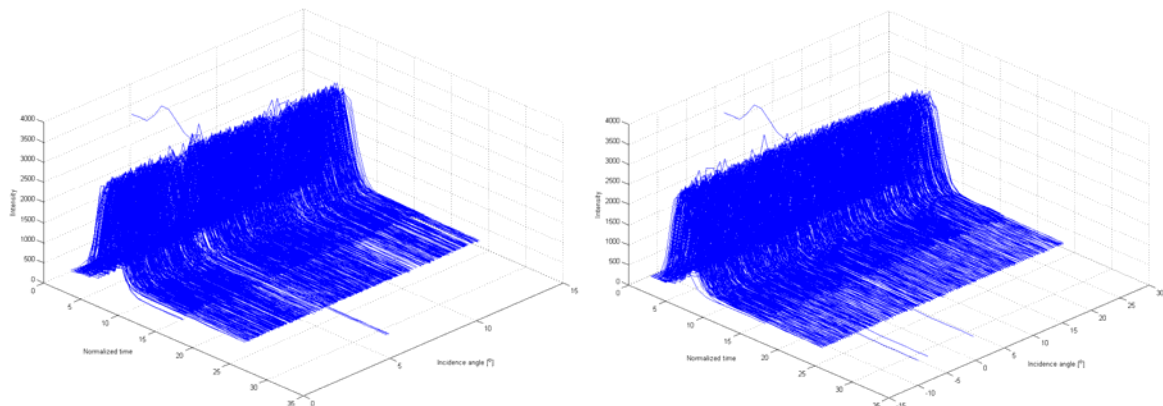


Figure 23 Waveforms as functions of horizontal (left) and vertical (right) incidence angle (Building I)

3.4.1 Gaussian parameters

Having performed Gaussian shape decomposition, the parameters were computed as a function of the incidence angle. Note that no special trend properties can be seen.

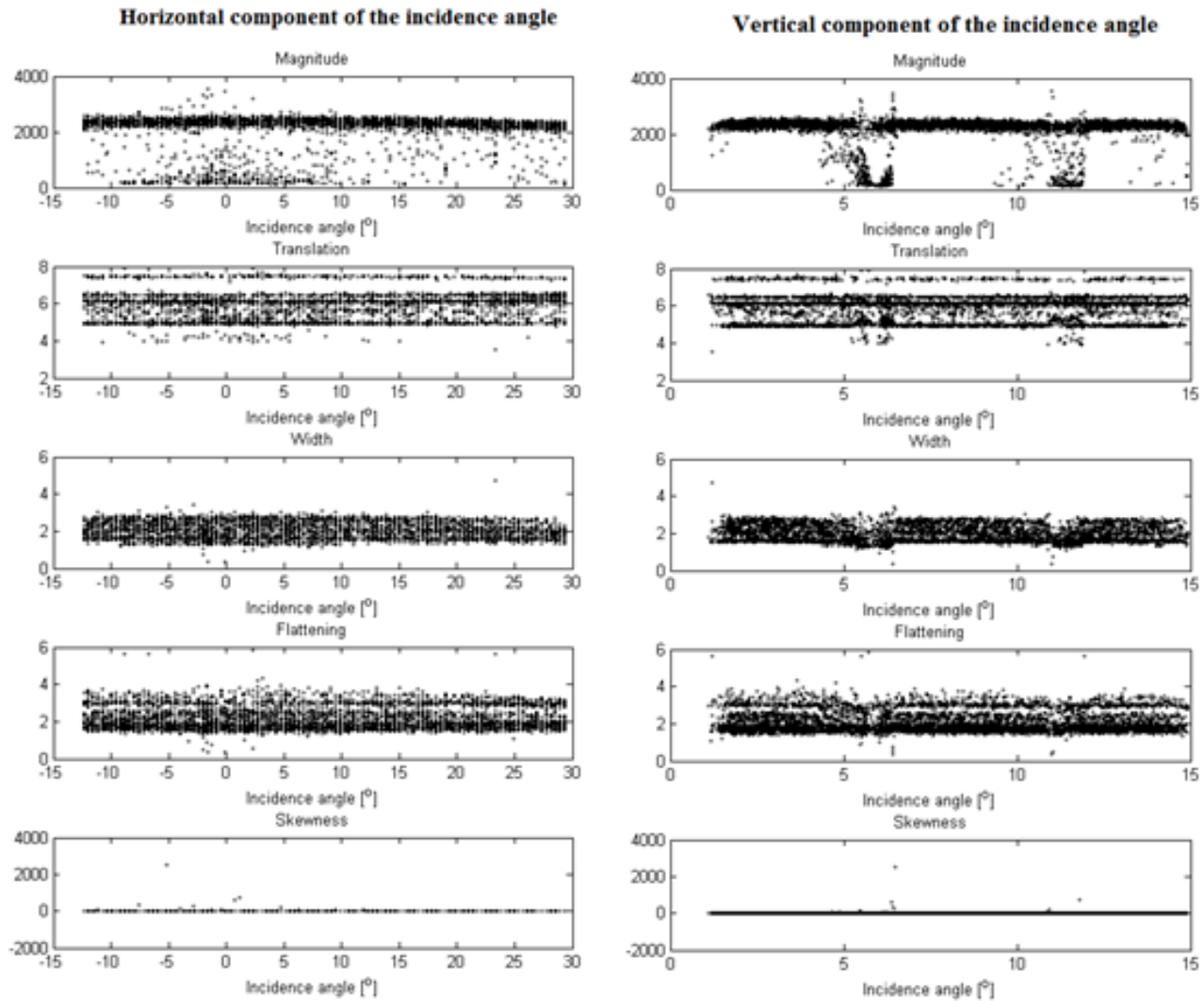


Figure 24 Gaussian parameters of Building I

The results of Building II can be seen in Figure 23. The horizontal angles are not incidence angle but the angle of the laser beam in the figure. Note that correlation can be detected between the magnitude and incidence angle, but the number of outliers is significant.

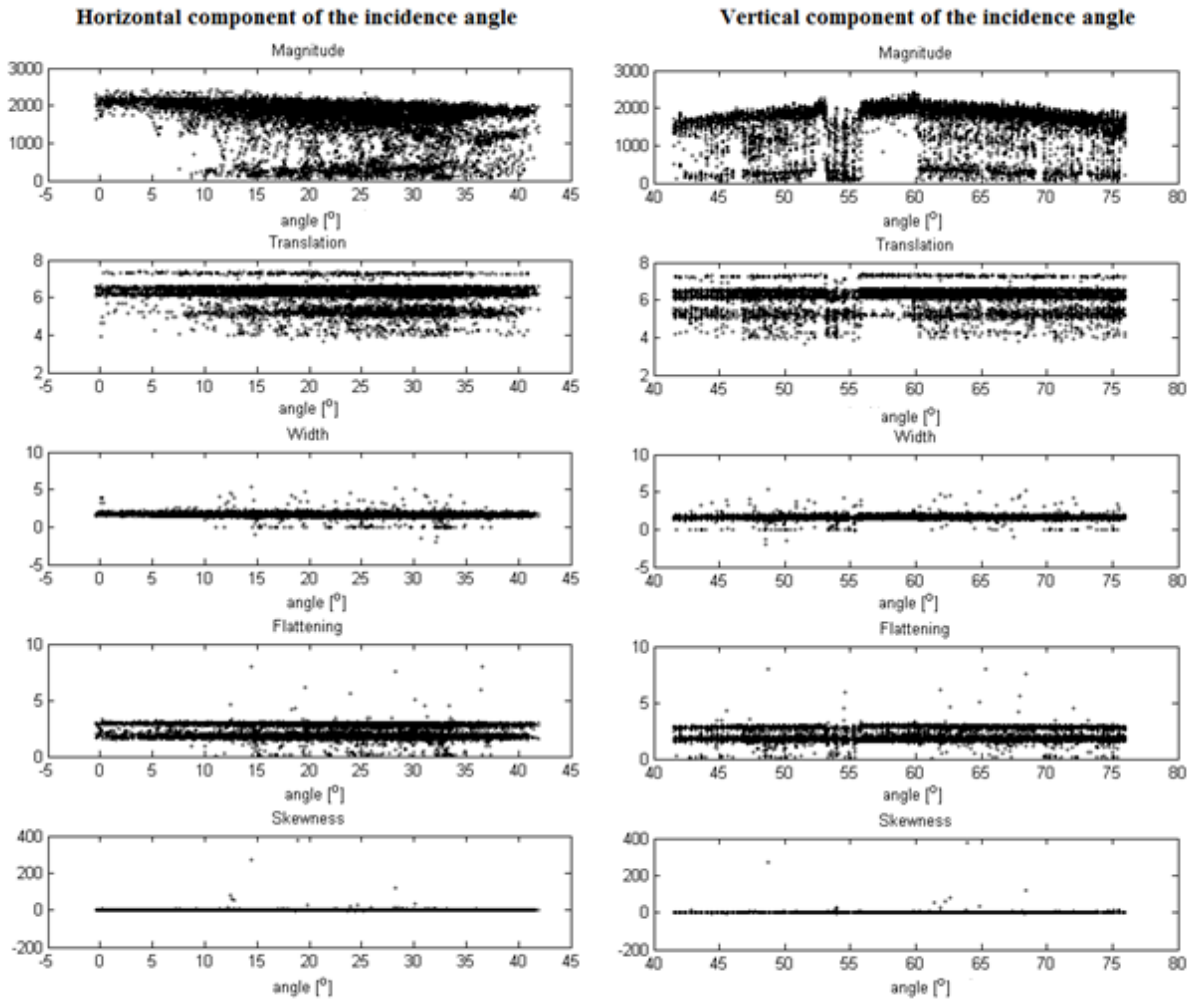


Figure 25 Gaussian parameters of Building II

3.4.2 Solution with feed-forward neural network

On the ScanPos4 dataset, we also used the feed forward neural network for incidence angle estimation as in 3.2.5. In this case, 16 intensity values were applied as input parameters of the neural network, and the outputs were the horizontal and vertical components of the incidence angles. The network layer alignment was {6, 4, 2}, and tangent sigmoid type transfer functions were used. Every odd point was the training set, and the validation set consisted of even points.

Applying neural network to the Building I dataset, the mean of the differences are nearly zero in the case of both incidence angle directions. The standard deviation of the vertical angle was 3.7° ,

while in the horizontal plane it was 10.5° . But this result on the examined dataset is clearly not acceptable, see Figure 26. Note that though the standard deviation seems to be low, yet the measurement ranges of the angle is also small, especially in the case of vertical angles.

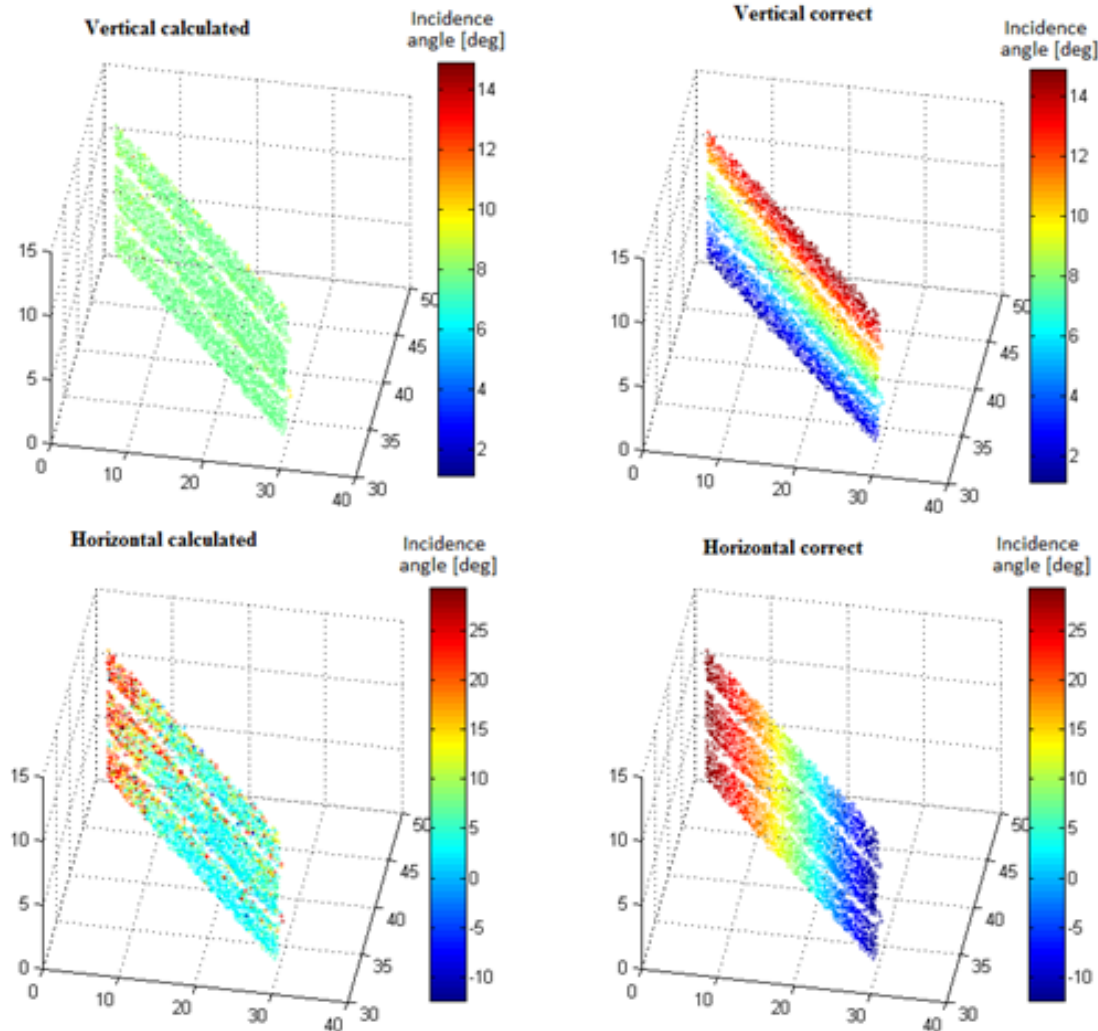


Figure 26 Calculated and correct solution for Building I

In the case of Building II, the mean of the residuals is also nearly zero, and the standard deviation of the horizontal angle is 8.9° , while the vertical angle deviation is 7.8° . These results are also not acceptable. The comparison between the calculated and correct values can be seen in Figure 27.

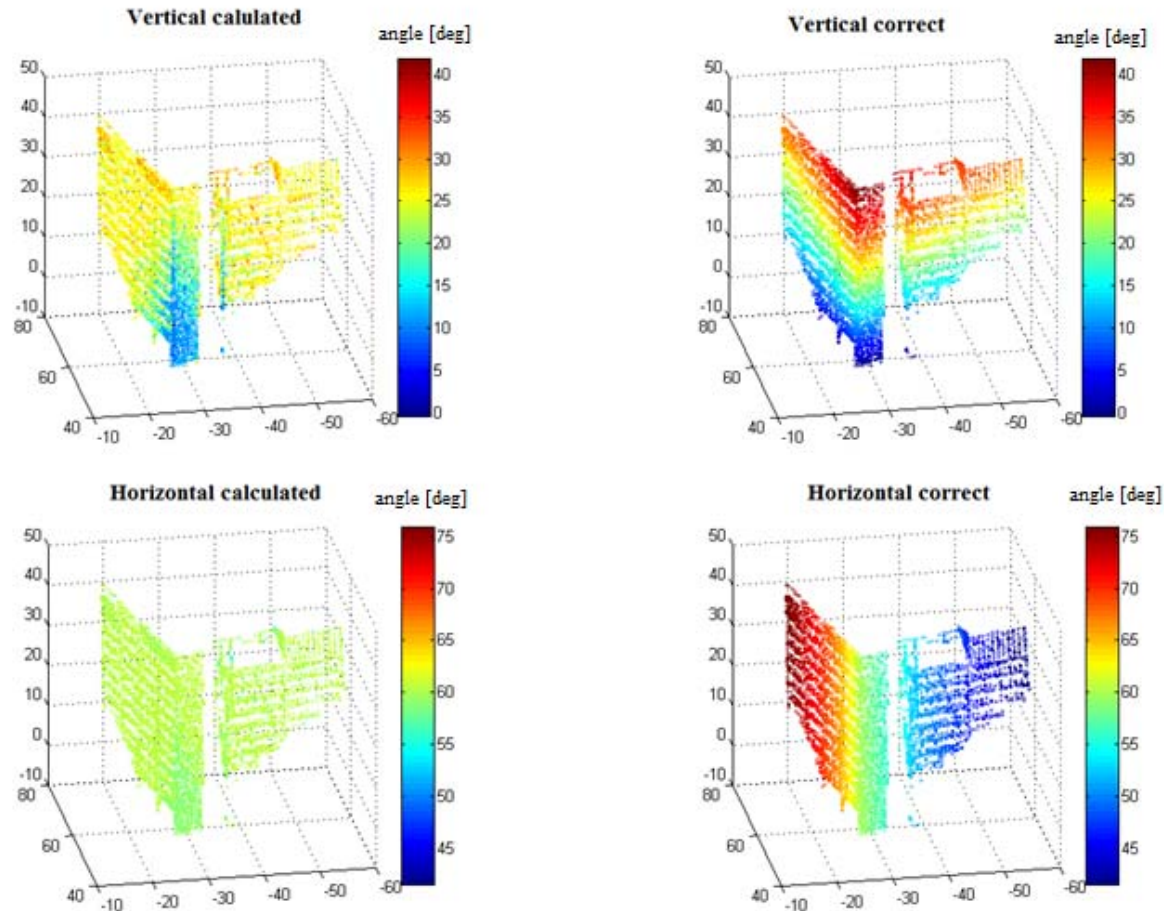


Figure 27 Calculated and correct solution for Building II

4. WAVEFORM-BASED CLASSIFICATION FROM AIRBORNE LIDAR

4.1 Background

Chapter 3 discussed the concept of waveform decomposition and the theory of applying the decomposed waveform parameters to incidence angle estimation. Using terrestrial scanner data, described in Section 3.2, the methodology was tested and the results were evaluated in Chapter 3. In the next phase, airborne LiDAR data, acquired in a normal mission, was processed to obtain performance evaluation for typical operational environment. Extracting or identifying incidence angle features from waveforms allows to obtain object information based on a single waveform;

without knowing their spatial position or using neighborhood points' information. Obviously, determining the orientation surface, in general, is not a challenged topic when information from the point environment can be used, but it becomes rather difficult if these neighbor points are not available, and the estimation has to be based on only the shape of the waveform.

4.2 Data set

NOAA acquired a unique airborne data set in the summer of 2013 to support comparative analysis of airborne LiDAR data. A unique aspect of the data acquisition campaign was that three sensor units were installed in an aircraft to simultaneously acquire data. The three Riegl systems included the Q680i and Q780 models that have full waveform capabilities and, subsequently were used in this study. The waveform data was sampled at 1 ns, and two digitizers, low and high channels, were used in both instruments, see Table 8. The main parameters of the NOAA data acquisition data sets. The airborne campaign covered two sites: Corbin, VA and Duck, NC.

Table 8 The main parameters of the NOAA data acquisition data sets

	Site 1 – Corbin, VA		Site 2 – Duck, NC	
	Waveforms			
Scanner (SN)	Q680i (9997902)	Q780 (9999173)	Q680i (9997902)	Q780 (9999173)
Sampling interval [ns]	1	1	1	1
Number of facets	4	4	4	4
Number of records	12,357,036	11,983,916	8,840,996	8,496,610
Blocks of low power channel³⁾	2	2	2	2
Number of reference channel samples	24	28	24	28
Number of low power channel samples	60 or 120	60 or 120	60 or 120	60 or 120
Pulses in the scan line (<i>s</i> dimension)	1431-(1432)	1435-(1436)	1431-(1432)	1435-(1436)
Scan lines (<i>l</i> dimension)	550	532	1011	977
Bands (<i>w</i> dimension)	120	120	120	120
Corresponding point cloud (LAS)				
No. of points in the whole strip	19,412,881	21,434,764	7,862,489	7,796,281
Max. no of returns	7	7	6	7
Points in corresponding cloud	936,285	960,664	1,378,814	1,348,555

Max. no of returns	7	7	6	6
---------------------------	---	---	---	---

4.3 Data processing

This study covers two types of investigation on waveforms. The first one is classification by incidence angle, while the second topic is land type classification. Different methods and approaches are used to solve the classification problem.

4.3.1 Data preprocessing

The sensor level data preprocessing steps included the matching of records from the two data formats (SDF and LAS), conversion the binary data into Matlab readable format, etc. For the classification, the different categories (classes) had to be defined, requiring the spatial delimitation of the dataset, as part of the preprocessing.

Matching LAS and SDF records by timestamps

The LAS file specification supports the waveform storage, but in our case, the waveforms are stored separately in SDF file. Since the SDF does not contain the coordinates of the waveforms in the object space, and, unfortunately, it cannot be calculated because the global coordinates of the sensor reference point is not stored in the files, the records between LAS and SDF are matched based on the global reference timing (UTC). Note that the matches showed about 0-2 μ s differences between the timestamps, equivalent of about 600 m distance at the speed of light. in this time interval, which means that the 2 μ s difference is just caused by the different processing techniques, and matches with this time discrepancy are fine.

Footprint size

The average flight height (h) was ~680 m, and the beam divergence (δ) of the Riegl's Q780 system is 0.25 mrad, thus the footprint can be calculated with the following expression:

$$f = h * \delta = 0.17 \text{ m}$$

Calculating the scan angles

The Riegl SDF file format contains several parameters to georeference the waveforms in a spatial coordinate system. The locations of the waveform sample (s_i) can be determined by the following expression:

$$s_i = o + d \frac{v_g}{2} (t_i - t_{ref})$$

where o is the origin vector, d is the direction of the emitted pulse, t_{ref} is the reference time, v_g is the group velocity, see Figure 28.

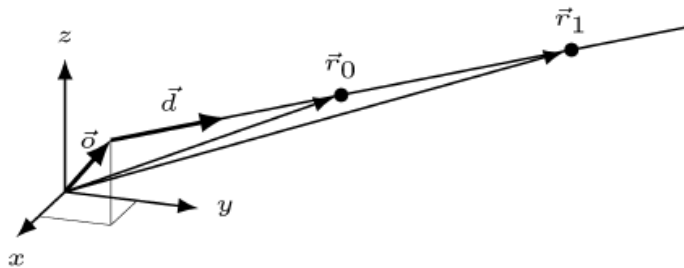


Figure 28 Locations in the sensor coordinate system from the Riegl Waveform Extraction Library Manual (Page 6)

Where the direction and the residual vector can be calculated by:

$$\delta_v = \arctan\left(\frac{v_3}{\sqrt{v_1^2 + v_2^2}}\right)$$

where v is any vector and δ_v is the direction of v in the X-Y plane. First, just the d (direction of the emitted pulse) is used to calculate this direction. The results for a rooftop are shown in Figure 29.

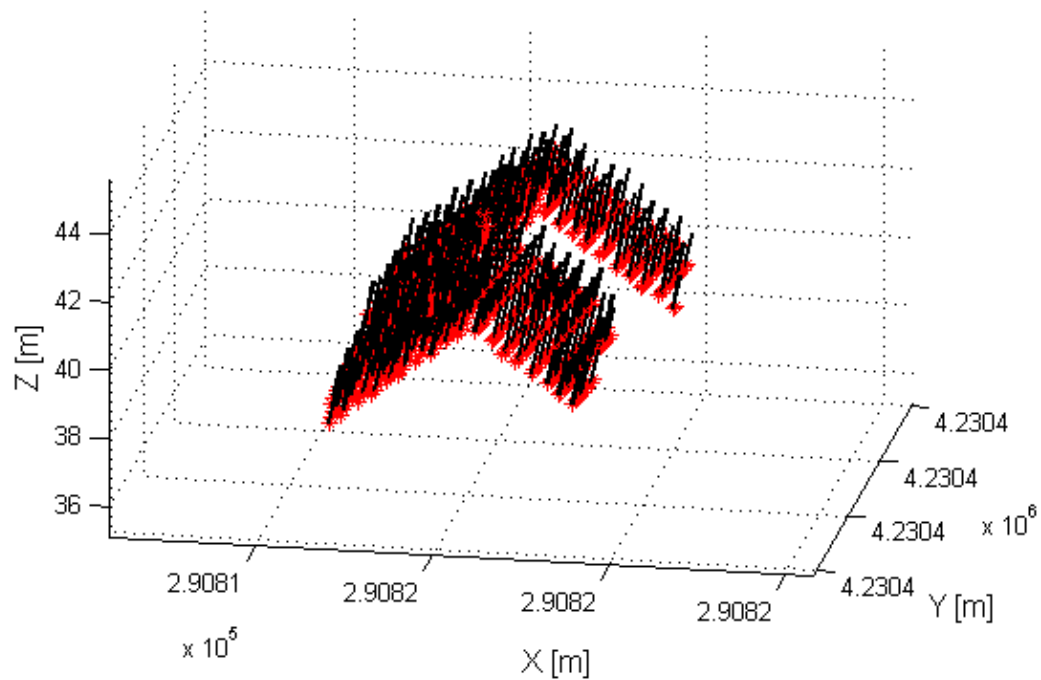


Figure 29 Laser beam directions

The LAS files contain the scan angle, but the precision of these data is at degree-level. The comparison of the calculated scan angle from the direction vector ($v = o$) with the scan angle provided by the LAS file can be seen in Figure 30. Note that the 11° and 12° scan angles are from the LAS file, and the red graph in the figures shows the calculated scan angles. The dashed lines depict the assumed rounding limits.

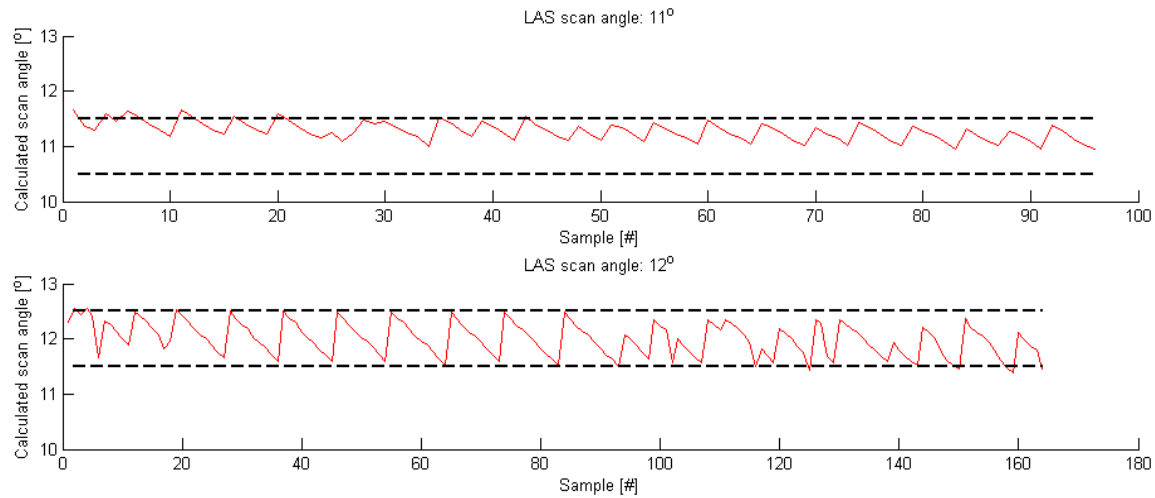


Figure 30 Scan angles from LAS file and calculated values from the SDF file using the direction vector

The direction is also determined from the sensor reference point by calculating the residual vector of the origin and direction vectors of the emitted pulse ($v = o + d$). In this case the comparison between LAS and the SDF files shows larger discrepancies, see Figure 31.

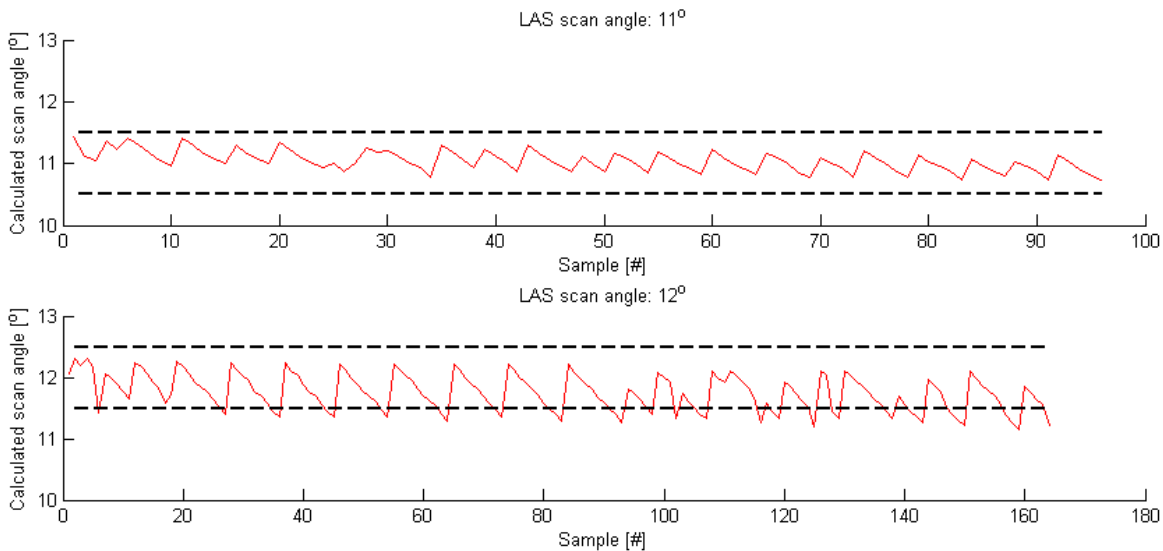


Figure 31 Scan angles provided by LAS file and the calculated angles from the SDF file using the origin and direction vectors

4.3.2 Feature extraction

The features extraction provides the input data for all the subsequent processing. The feature vector includes both derived and original samples from the waveforms; Table 9 lists the features used in this investigation.

Table 9 Features

#	Feature (parameter)	Description
FP1	Parameters of Generalized Gaussian	Parameter vector of the fitting by the generalized Gaussian function
FP2	Kurtosis and skewness	The statistical estimation of kurtosis and skewness from the samples
FP3	Vector of waveform samples	The waveforms are represented as the vector of the intensities (samples)
FP4	Translated vector of waveform samples	Same as P4, but the maximum place is translated to the middle of the vector
FP5	Median waveform	Median waveforms calculated from the classified waveforms, generally the groups are determined by the user (training-validating process)

Generalized Gaussian function parameters

There are four parameters to model the generalized Gaussian function as defined below:

$$G(x, p) = p_1 e^{-\left[\frac{(x-p_2)}{p_3}\right]^{p_5}} + p_4$$

where p_1 is the amplitude, p_2 is the position of the peak (mean), p_3 is the dispersion of the function (standard deviation), p_5 is the shape parameter (it is Gaussian distribution, if $p_5=2$), and p_4 is the translation in Y direction. Figure 1 shows waveform shapes after changing one of the parameters.

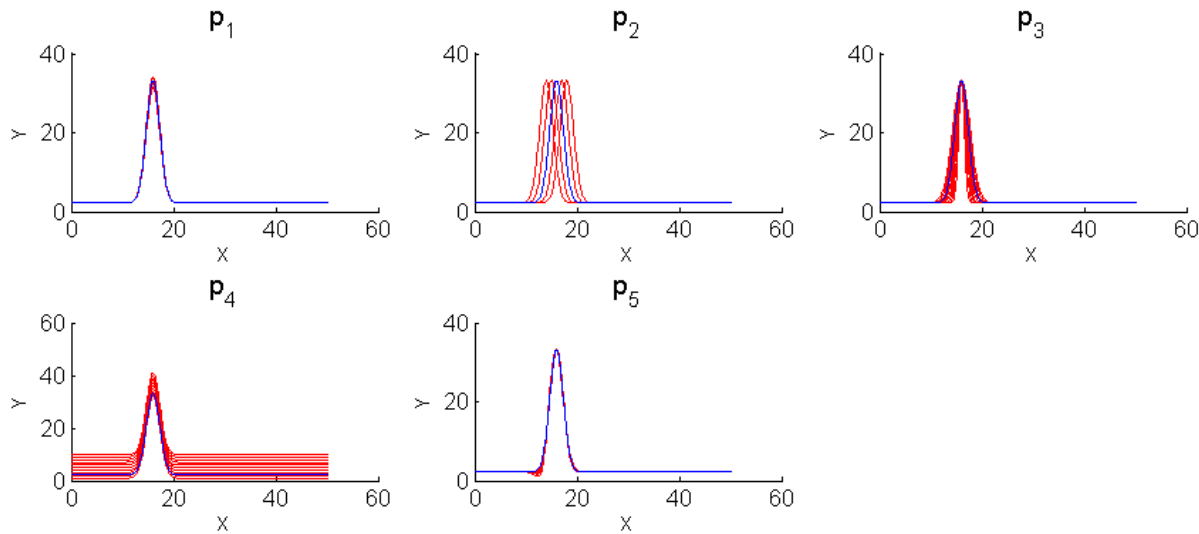


Figure 32 The effect of the parameters on the shape of the function

The parameter estimation is based on the minimization of the L2 norm of the residuals. Assuming that the (x,y) pairs are the digitized discrete samples of the waveform, the Gaussian function can be determined by the following expression:

$$\min_p \|y - G(x, p)\|$$

The optimization problem was solved by numerical methods using Matlab.

Kurtosis and skewness

The general discussion, including illustrations, is provided in 3.3.3. These parameters are estimated from the standardized third and fourth central moments of the samples by the following expressions:

$$K = \frac{E[X - \mu]^4}{\sigma^4} \approx \frac{\frac{1}{n} \sum_{i=1}^n (x_i - \bar{x})^4}{\left(\frac{1}{n} \sum_{i=1}^n (x_i - \bar{x})^2 \right)^2}$$

and

$$S = \frac{E[X - \mu]^3}{\sigma^3} \approx \frac{\frac{1}{n} \sum_{i=1}^n (x_i - \bar{x})^3}{\left(\sqrt{\frac{1}{n} \sum_{i=1}^n (x_i - \bar{x})^2} \right)^3}$$

where X is the random variable (vector) of the samples, μ is the expected value, σ is the standard deviation, x_i are the samples, \bar{x} is the sample mean and n is the sample size.

Vector and translated vector of waveform samples

The representation of the waveform in the SDF file is realized as the C-type vector of the intensity values, called sample vector. The time differences between the vector elements are constant 1 ns. Obviously, this vector can be the input of the classifier. The advantage of using these vectors is all the information of the waveform is preserved. The disadvantage, obviously, is the high dimensionality of the input vector. Furthermore, there is data redundancy that is not exploited for input data dimension reduction. Thus, in an extreme case, the classifier may not be able to detect the differences due to handling the large number of input variables. Note that no time information, such as start time of the wave, etc., is contained by these vectors.

The length of the sample vectors in the two data sets can be 60 or 120, and the values are from the low or the high channel digitizers. In this study, data from the low channel was used, as more waveforms are available from that sensor. The length of the sample vectors from the low channel is 60; those few, of which the vector size is 120, was removed from the examined dataset.

Analyzing the sample vectors, it was noted that the sample maximum peak locations of the waveforms are fluctuating with 1-2 indices around the median peak location. It is probably caused by the digitizing process of the LiDRA sensor; no explanation was provided by the vendor. Further investigations proved that the location of the maximum peak has no information about the object from that was backscattered, and, therefore, these differences may trouble the classification process. For this reason, the elimination of these differences is preferred to obtain better performance. The elimination process is shown in Figure 33 and Table 10, the whole samples (1) move to the standard location of the peak (2), and the empty sample places are filled with the first sample value (3). Note again that the translated vectors have no timing information.

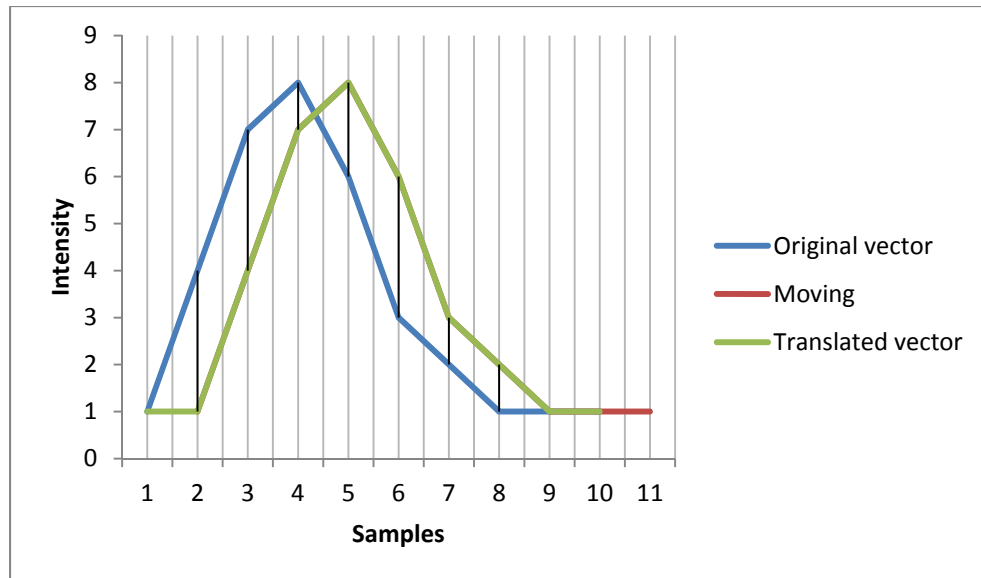


Figure 33 Shift correction of waveforms

Table 10 Shift corrections

	Sample #	1	2	3	4	5	6	7	8	9	10	11
(1)	Original vector	1	4	7	8	6	3	2	1	1	1	
(2)	Moving		1	4	7	8	6	3	2	1	1	1
(3)	Translated vector	1	1	4	7	8	6	3	2	1	1	

added

removed

Median/average waveforms

The median or the average waveforms can be calculated from the sample vectors or translated sample vectors. An example of the computation is shown in Figure 34 and Table 11.

The median and average waveforms are determined as the part of the training process, when the classes of the waveforms are determined by the investigator. The residual vectors, such as median and average vectors, are calculated for each class from the class members, and thus, theoretically, these estimated common vectors are the typical sample vectors.

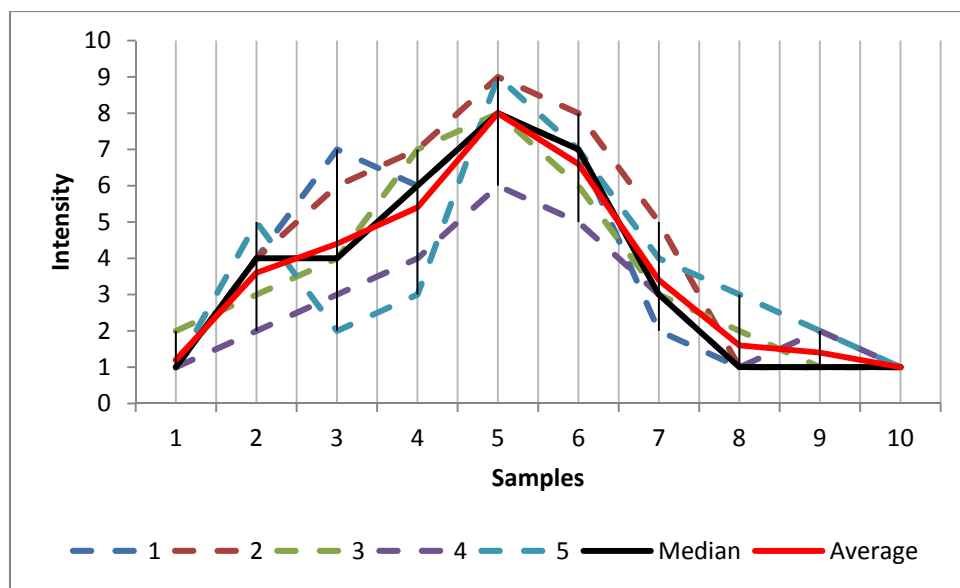


Figure 34 Median and average waveforms

Table 11 Median and average waveforms

Vector #	Samples									
	1	2	3	4	5	6	7	8	9	10
1	1	4	7	6	8	7	2	1	1	1
2	1	4	6	7	9	8	5	1	1	1
3	2	3	4	7	8	6	3	2	1	1
4	1	2	3	4	6	5	3	1	2	1
5	1	5	2	3	9	7	4	3	2	1
Median	1	4	4	6	8	7	3	1	1	1
Average	1	4	4	5	8	7	3	2	1	1

4.4 Data classification

The classifiers tested in this investigation are listed in Table 12, including the input parameters used. Of course, the question of selecting the optimal classifier for a certain data characteristics, in general, is difficult. Similarly, the input parameter selection has challenges too, though, it is less problematic. This is the reason that several features, extracted from waveforms are tested with the most commonly used classifiers (that seemed to be adequate for the waveform data). Finally, the selection of classes is also part of the classification process. Note that in most cases, supervised classification is used; the classes are defined by experts.

Table 12 Classifiers

Feature	Method	Description
FP1, FP2	Linear discriminant analysis	Linear classifier, based on statistical considerations, normal distribution of the input assumed
FP5	Measuring distance from median waveform	The closest matching median waveforms indicate the class
FP1, FP2, FP3, FP4	Feed forward neural networks	Commonly used neural network, which can handle non-linear classification problems, and also effective for other problems (regression, etc.)
FP4	Self-organizing map neural network (Kohonen network)	This type of neural network is used for unsupervised classifying, and can detect the similarities between the input

4.4.1 Classifiers

Linear discriminant analysis

Linear discriminant analysis (LDA) is a widely used, general statistical tool for classification. The method assumes that the linear combination of the features can produce the class information:

$$D_j = d_{0,j} + d_{1,j}x_1 + d_{2,j}x_2 + \cdots + d_{k,j}x_k,$$

where D_j is the j th discriminant function, the $d_{0,j} \dots d_{k,j}$ are the “weights” or coefficients of the function and $x_1 \dots x_k$ are the elements of the feature vector. The j th discriminant function measures whether the sample is included by the j th class or not. The discriminant analysis assumes that the independent variables (the features) are of normal distribution, and they follow different normal distributions in the classes. In other words, different classes generate samples corrupted by different type of normal error. Note that the method has other assumptions.

During the training phase, the algorithm estimates the coefficients of the discriminant function. In the validation phase, when the classifier is used, the discriminant functions have to be evaluated, which provides the class prediction. In this study, this classifier is used for land type

classification, based on the Gaussian parameters and the kurtosis-skewness pairs as feature vector for inputs

Measuring distance from median waveform

This method is very simple and efficient in computational sense. As it was presented above, each median or average waveform represents one class. The idea is to calculate the distances between the examined waveforms and the median or the average waveform. The shortest distance indicates the class. An example¹ is shown in Table 13. The sample vector, to be classified, is in the first row and the median sample vectors are in the 2nd and 3rd line. First, the distance of the samples has to be calculated, this distance can be defined by different measures, and here L2 norm (the squared root is the Euclidean distance) is used. Finally, these distances have to be summarized and the smallest sum indicates the class; Class 1 in this example.

Table 13 Classification using L2 norm

Sample vector	Samples									Sum
	1	2	5	6	8	6	2	1	1	
Class 1 median waveform	1	1	3	6	9	7	4	3	2	1
Class 2 median waveform	1	4	6	7	9	8	5	1	1	1
Distance from Class 1	0	1	4	0	1	1	4	4	1	0
Distance from Class 2	0	4	1	1	1	4	9	0	0	20

In another approach, the maximum norm is used instead of the L2 norm. The usage of this norm is suggested by its robustness and its connection with other statistical assumptions (Kolmogorov-Smirnov distance). In this case, the class is selected where the maximum distance between the sample and median waveforms is minimal. Table 14 shows an example.

Table 14 Classification using max norm

Sample vector	Samples									Max
	1	2	5	6	8	6	2	1	1	
Class 1 median waveform	1	1	3	6	9	7	4	3	2	1
Class 2 median waveform	1	4	6	7	9	8	5	1	1	1
Distance from Class 1	0	1	2	0	1	1	2	2	1	0
Distance from Class 2	0	2	1	1	1	2	3	0	0	3

¹ <http://davis.wpi.edu/~matt/courses/soms/>

Feed forward neural networks

The feed forward neural network is a general type of neural network which can be used for regression, classification, pattern recognition, etc. In this study, the feed forward networks are used as a pattern recognition tool because the expectations are that the waveform similarities can be recognized. The input of the network is the sample vectors. To reduce the dimensionality, only half of the waveform record is used; earlier tests indicated that the regions away from the pulse have less contribution. The input vector to the network is formed from indices 10th to 40th. The implementation was based on the Matlab built-in feed forward network (*patternnet*), which was especially developed for pattern recognition. Several configurations of hidden layers and neurons were tested, and the results showed that the best performance was achieved with 2 hidden layers and neurons of 5 and 10, respectively, shown in Figure 35. The activation functions are of sigmoid-type in the hidden layers, and the performance was measured by cross-entropy.

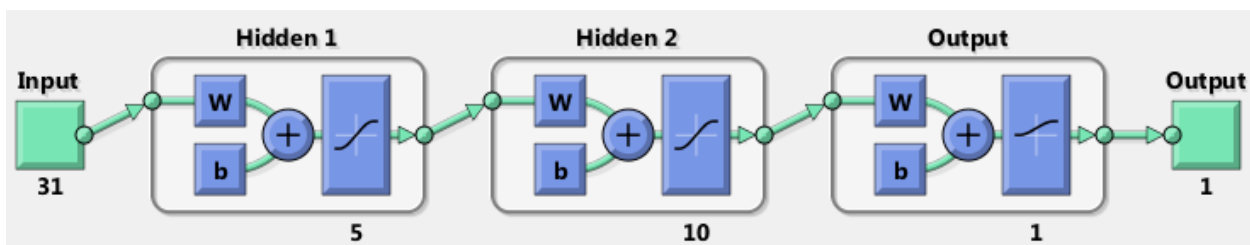


Figure 35 Final configuration of the pattern recognition neural network

The number of output depends on the number of the classes. If there are two classes, the output is 1 or 0, which indicates that the sample of the input belongs to Class 1 or not. In this study, this type of network is used with 2 classes roof extraction; discussed in subsequent section. In the training process, N number of sample vectors of 31 samples were used with their predetermined classes on the output. After forming the networks, the validation was executed on M number of sample vectors.

In order to prove the ability of the feed forward neural networks for classifying the waveforms as a pattern recognition problem, a preliminary simulation study was performed. Two reference

waveforms were defined; see the upper part of Figure 36. The Ref2 waveform is the modification of Ref1 with increasing the p_2 and p_3 parameters with +0.2.

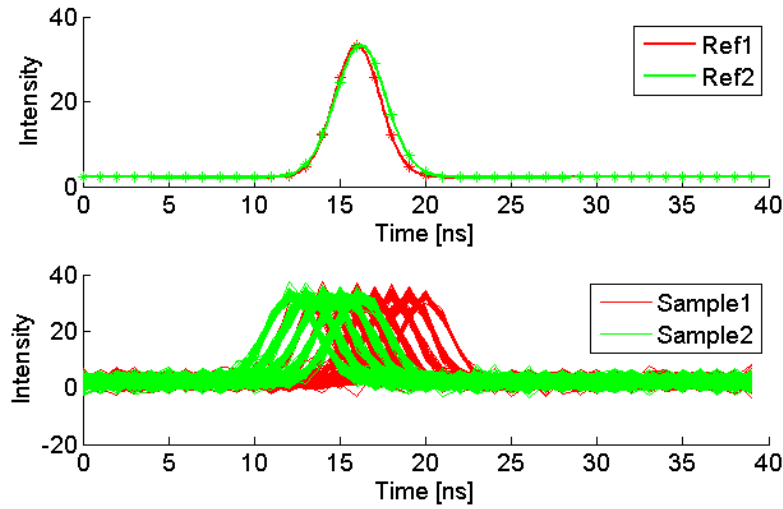


Figure 36 References (upper) and simulated waveforms (lower)

The simulated waveforms are created from these reference waveforms by adding a Gaussian noise with 1.5 standard deviation and shifting the sample indices randomly. The results as confusion matrix can be seen in Figure 37. Note that the total performance is 88.9% in the validation set, which implies that this type of network can distinguish the waveforms, that comes from different base signal, such as the waveform that is typical in the class. In the simulation, 600 random samples were used.

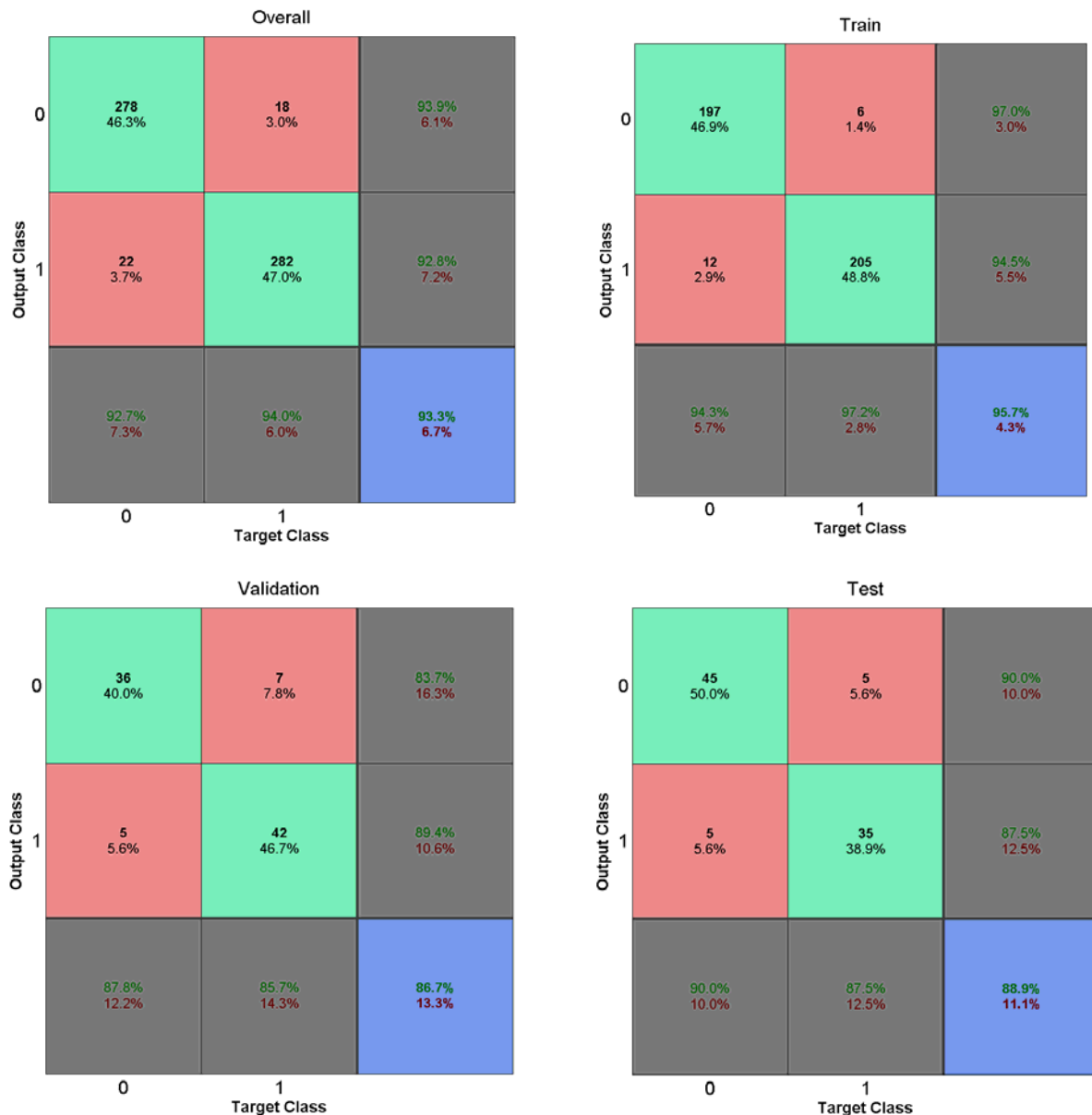


Figure 37 The pattern recognition feed forward neural network results on the simulated data

Self-organizing map

The self-organizing maps (SOM), aka Kohonen networks, are different neural networks, as these types of networks are very effective for clustering the data without prior knowledge. This process is the so-called unsupervised learning. SOM applies neighbor functions to keep the

topology of the input properties. The method can detect the similarities between the input patterns². The SOM network determines groups (clusters), in which the features are close enough to each other. These are also called as classes, but the word “classes” is restricted here for the user defined classes, and the word “group” for SOM created classes is used

One of the disadvantages of the SOM is that the groups are not known, as mentioned above. Therefore, a statistical comparison between the classes found by the SOM and the actual classes provided by the investigator is used. This evaluation results in the decision on which SOM groups represent which “real” class or classes. Furthermore, it may happen that more than one SOM group belong to one or more “real” classes, and more than one “real” class cover one or more SOM groups. Finally, a SOM group may have no pair within the “real” classes, indicating similarities in data, which has not been considered earlier.

The general configuration of the SOM network is shown in Figure 38. In this study, the translated sample vectors were used as input. The translation is required because of the “keep the topology” property of the SOM. Therefore, all the 60 samples of the vectors are used as features; no elements were removed to prevent any loss of waveform information. The number of the output of a SOM network depends on the layer structure. The network layer starting configuration is a NxM dimensional neuron grid; thus, for example, 2x2 grid has 4 outputs, while a 3x3 grid has 9 outputs. The dimension determines the number of groups that will be determined by the SOM; thus, 4 outputs provide the 4 groups of the clustered sample vectors.

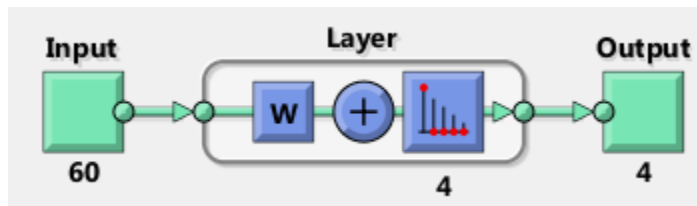


Figure 38 Configuration of the SOM network³

² <http://www.mathworks.com/help/nnet/ug/cluster-with-self-organizing-map-neural-network.html>

³ <http://www.mathworks.com/help/nnet/gs/cluster-data-with-a-self-organizing-map.html>

In the training session, there is no need to know prior the classes of the training sample vectors. The SOM will discover those hidden properties, and will decide on the grouping of the sample vectors. Thus, the inputs of the network are the number of the groups and the sample vectors. After the SOM clustered the waveforms into groups, the match to the “real” classes should be determined. These correspondences are done by comparing the suggestions of the SOM and the “real” classes; for this reason, knowing the prior classes of the input vectors is necessary.

The SOM will provide the “weights” for the 60 input samples. These weights represent the common sample vector of the SOM’s class. In the validation phase, the algorithm measures distances between the weights and the validation sample vectors to decide on which class they belong to. The closest one will determine this class. This process is same as it was introduced in the “Measuring distance from median waveform” section, but the median waveforms are the weight vectors in this case.

4.4.2 Confusion matrix

The concept of the confusion matrix is the most widely used framework to validate the performance of classification methods. Here, a short discussion is provided.

Table 15 Confusion matrix

	road1	road2	grass	tree	building	False negative
road1	15 55.6%	1 2.0%	11 21.2%	0 0.0%	0 0.0%	44.4%
road2	0 0.0%	10 41.7%	0 0.0%	0 0.0%	0 0.0%	0.0%
grass	0 0.0%	0 0.0%	25 65.8%	2 4.8%	0 0.0%	7.4%
tree	0 0.0%	13 33.3%	0 0.0%	15 50.0%	0 0.0%	46.4%
building	0 0.0%	0 0.0%	0 0.0%	0 0.0%	4 100.0%	0.0%
False positive	0.0%	58.3%	30.6%	11.8%	0.0%	71.9%

Table 15 shows an example; the rows represent the classes of the waveforms, and the columns are the classes selected by the classifier. Thus, the bold numbers in the (i,j) cells give us the number of those waveforms which are in the i^{th} class, while the classifier selected the j^{th} class. If the classifier works perfectly, all the elements except the diagonals should be zero. The percentages under the numbers in the table are calculated by the following expression:

$$C_{i,j} = \frac{n_{i,j}}{\sum_{k=1}^N n_{k,j} + \sum_{k=1}^N n_{i,k} - n_{i,j}} * 100 \%,$$

where $n_{i,j}$ is the number of the (i,j) cell and N is the number of the classes. Thus, the percentage shows the ratio of the total matches and mismatches; obviously, it is independent from the number of the points within the classes. The cells are color-coded; darker color indicates higher percentage. If the same shades repeat within a column, it means that the classifier cannot distinguish the classes properly; for example, see the column of road2. The ratios of false positives and false negatives are found in the last rows and columns. The false negative shows the ratio of the mismatches, when the class indicated by the column was selected, but the class of the row was supposed to be selected. The calculation is the following:

$$N_i = \frac{n_{i,i}}{\sum_{k=1}^N n_{k,i}} * 100 \%$$

In the case of false positive, the classifier chooses the class of the row, but it was supposed to be in the class of the column:

$$P_j = \frac{n_{j,j}}{\sum_{k=1}^N n_{j,k}} * 100 \%$$

Finally, the total classification error is the ratio of the all of the matches against the all samples:

$$T = \frac{\sum_{i=1}^N n_{i,i}}{\sum_{i,j=1}^N n_{i,j}} * 100 \%.$$

The evaluation of the total matches depends on the number of the classes. For example, if two classes are examined, the 50% match rate is same as randomly choosing a class (flip the coin).

But if the number of classes is greater, the 50% can be evaluated as a better result as the random selection. The total ratio of a random classifier is $\frac{1}{N} * 100\%$.

4.4.3 The library and tools

Tools

A MATLAB library was developed to support this project, including basic data manipulation operations, organizing the data, implementing algorithm, and to evaluate and visualize results. The source code is available from Google Codes using SVN connection (<https://code.google.com/p/lidar-wf-classification/>, 2014). All the tools used are listed in Table 16

Table 16 Software and 3rd party libraries (links from 2014)

LASTools	LAS file operation, some functions are free, others are limited, download from http://www.cs.unc.edu/~isenburg/lastools/
Riegl's Waveform extraction library	Riegl's library for extracting data from SDF file
Matlab	General mathematical framework
FugroViewer	Free LAS file viewer from Fugro Ltd., download from http://www.fugroviewer.com/request/default.asp
QGIS	Free and open source GIS desktop application, download from http://www.qgis.org/en/site/

4.5 Classification evaluation

4.5.1 Incidence angle estimation

Data preparation

The estimation of the incidence angle from waveform shape deformation was investigated based on using targets in Chapter 3. Here the focus was on using typical airborne data, in which case no ground control is available in general. Therefore, objects that can be easily described by geometrical primitives should be considered in order to obtain some local relative reference necessary for the evaluation. For this reason, a point cloud from a roof was selected from the Corbin data set, see Figure 39. The scan angle of these points covers 11-12°. Note that the point cloud was divided into two classes (data sets), depicted by green and red. Both point sets define a

plane, and the angle between these planes is around 60° . As the normal vectors of the planes are notably different, the material of the backscattering object (target) is the same, and the scan angle is also nearly identical, the comparison of the waveforms between these two classes is expected to show the difference caused by the incidence angle.

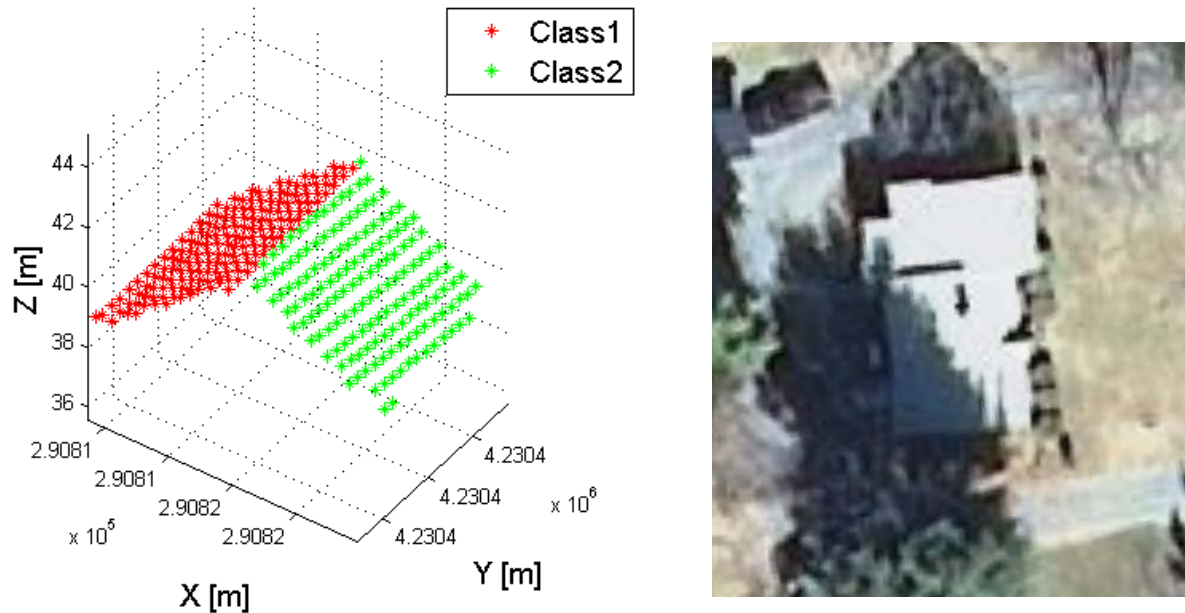


Figure 39 Roof with two classes (left) and aerial photo of the building (right)

In order to make sure that all the points belong to the roof, a fitting plane was estimated for both sides, and points with a distance from the plane more than 3-times of the standard deviation of all distances (3-sigma rule) were removed from the point sets. The outputs of this calculation with the results are shown in Figure 40 and Table 17.

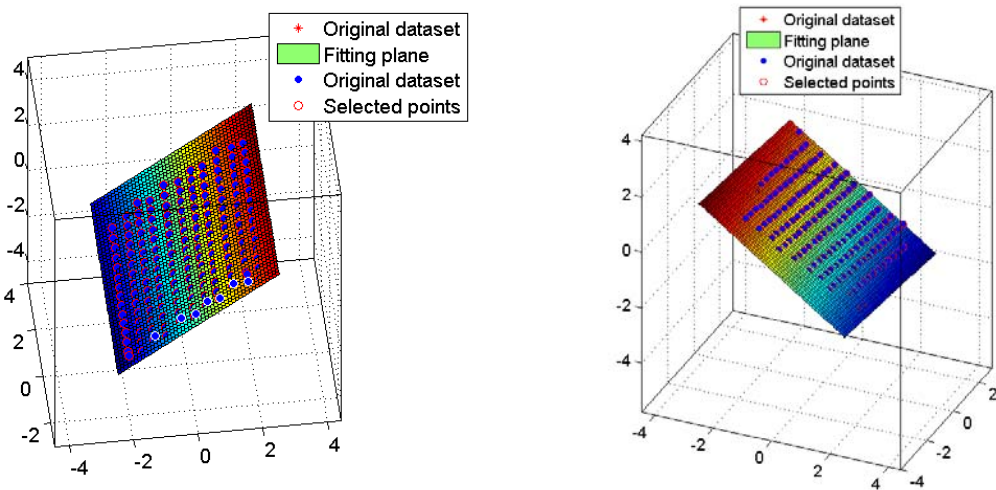


Figure 40 Plan fitting and outlier removal

Table 17 Statistics of point removal

	Class 1	Class 2
Number of points	172	158
Standard deviation (STD) [m]	0.1	0.3
Number of removed points	7	4
STD after removal [m]	0.04	0.03

Gaussian parameter estimation

The generalized Gaussian parameters were calculated for both classes based, as described in section 4.3.2. The averages and standard deviations of the parameters and the histograms for all parameters are shown in Figure 41 and Table 18. Note that the parameters are quite similar for both classes; the order-of-magnitude of the differences are two times less than the standard deviation. Therefore, the classification based only on these parameters is difficult.

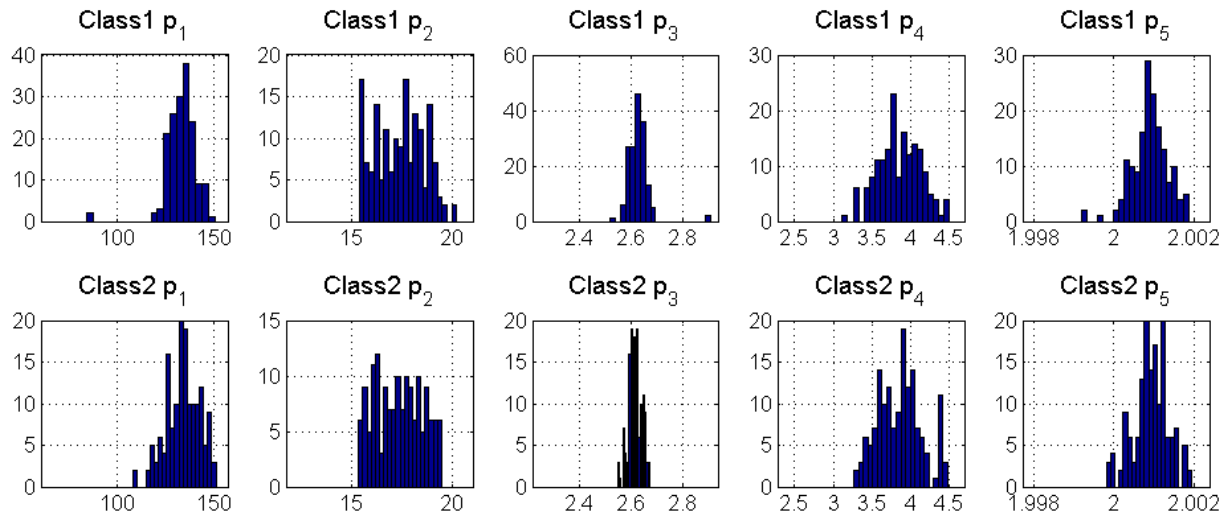


Figure 41 Histograms of the six Gaussian parameters

Table 18 Statistics of the Gaussian parameters

		p₁	p₂	p₃	p₄	p₅
Class 1	AVG	133.131	17.367	2.637	3.858	2.001
	STD	7.933	1.210	0.100	0.279	0.000
Class 2	AVG	134.336	17.376	2.623	3.935	2.001
	STD	10.764	1.204	0.064	0.914	0.001

Unfortunately, calculating the skewness and the kurtosis parameters resulted in a similar conclusion, i.e., the average and the median values are very close to each other for the two classes, and the standard deviation is much higher, see Table 19 and Figure 42.

Table 19 Skewness and Kurtosis results

	Skewness		Kurtosis	
	AVG	Median	AVG	Median
Class 1	2.291	2.292	6.909	6.911
Class 2	2.295	2.296	6.927	6.939

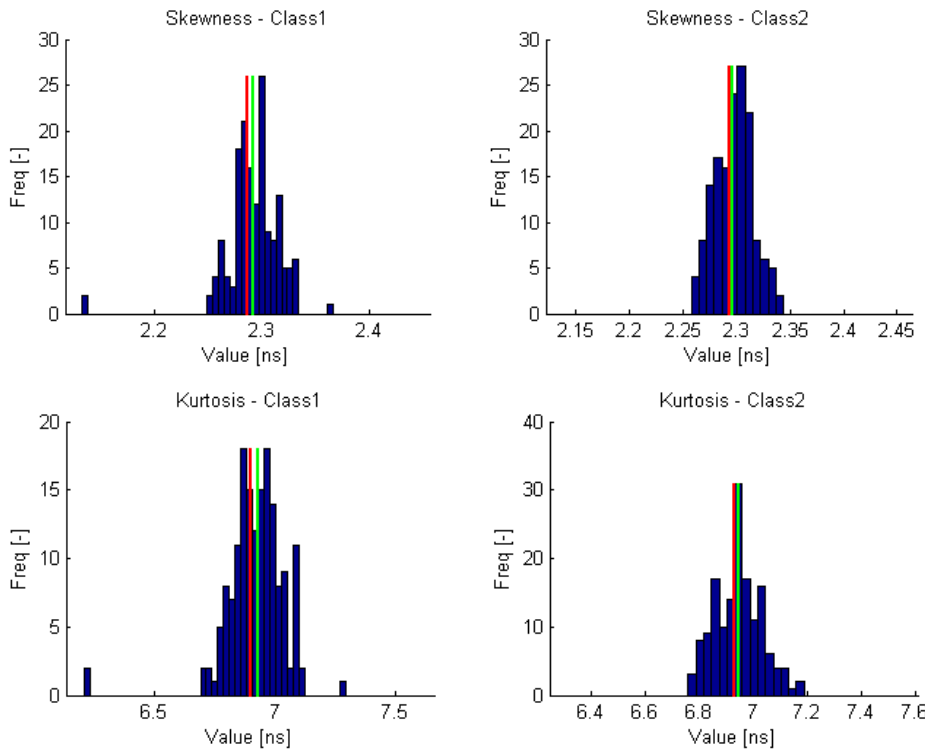


Figure 42 Histograms of skewness and kurtosis; mean and median are marked by red and green, respectively

Although the first look of the Gaussian, skewness and kurtosis parameters show no desired differences, a routine discriminant analysis was performed on these parameters. The results as confusion matrix are shown in Figure 43. Note that the success ratio is 53.9%, which is about same as just randomly selecting a class (50%).

	roof1	roof2	False negative
roof1	102 41.1%	63 26.7%	38.2%
roof2	83 32.4%	71 32.7%	53.9%
False positive	44.9%	47.0%	54.2%

Figure 43 Confusion matrix from the discriminant analysis

Median waveforms

The above presented results clearly indicate that the Gaussian parameters cannot be used for describing the changes on waveforms due to different incidence angles. Therefore, the next logical step is to use the entire waveform for classification, as opposed to the six parameters.

First, the average and median waveforms are analyzed for the classes; Figure 44 shows these functions, marked by red and blue lines. The ranges of the standard deviation at the samples are depicted with dashed lines and then the black lines indicate the minimum and maximum values. Note that spline interpolation is used on the data.

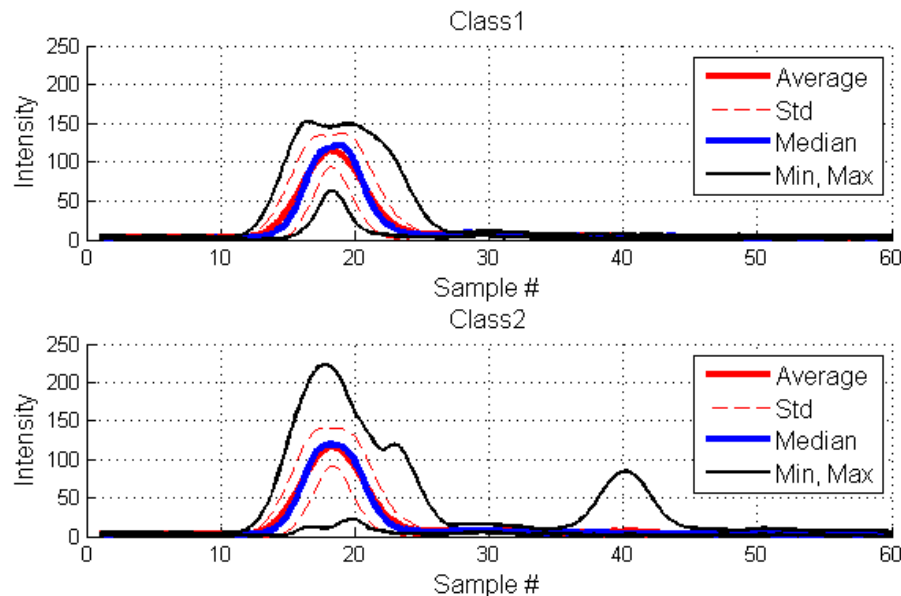


Figure 44 Typical waveforms with spline interpolation used for visualization

Figure 45 shows the median waveforms between the 10 and 40 samples, dashed lines depict the range of the standard deviation. Note that the upper and lower bounds are not parallel because of the spline interpolation. Analyzing the figure, a little difference can be noticed between the two classes around the maximum peak, but, unfortunately, the standard deviation is much higher than this difference, consequently, it is statistically not relevant.

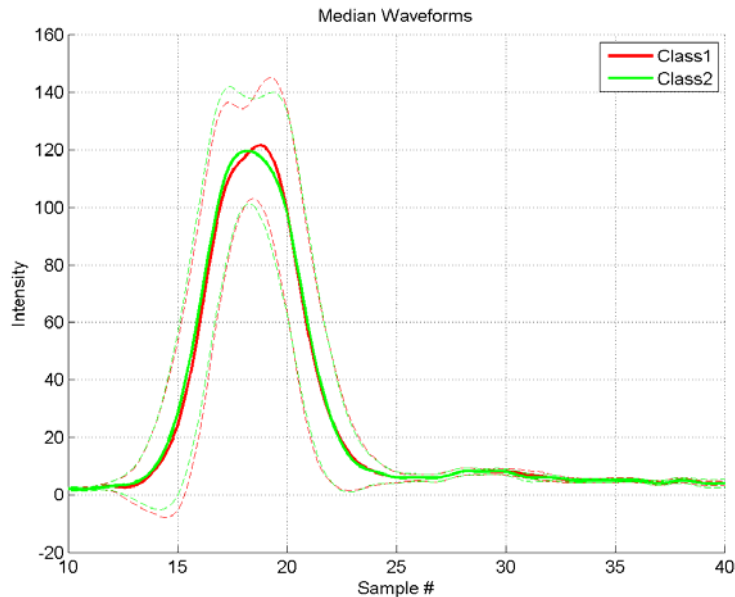
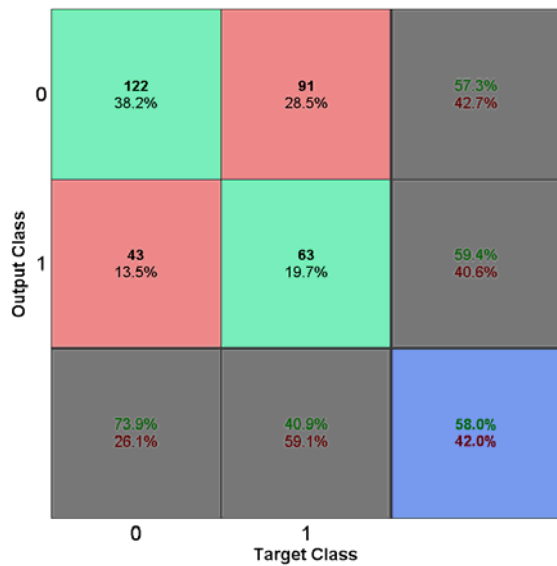


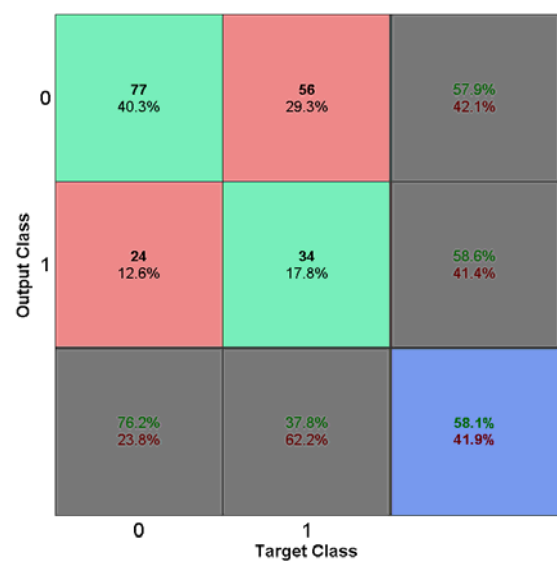
Figure 45 Median waveforms for the two classes

Neural networks

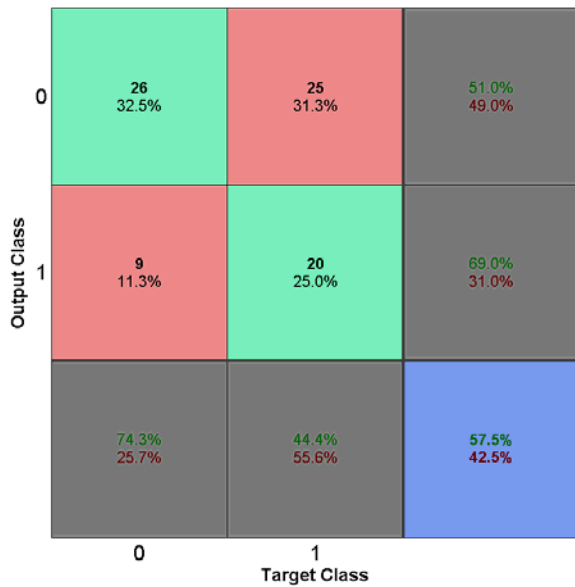
As it was presented above the Gaussian parameters and the median waveforms could not provide acceptable results. Therefore, as the last attempt, pattern recognition neural networks with the translated sample vectors as inputs were tested; the neural network may provide better result due to its capability to handle nonlinear classification problems. The 85% of the data formed the training set and 15% of the waveforms were used for validation. The results, including visualization are shown in Figure 46. The Figures 46 (a)-(c) show the confusion matrix on the overall, the training and the validation set. As we can see, the total score is ~58% which is the best result comparing the other classification methods, but it is still just slightly better than choosing the classes by coin flipping (50%).



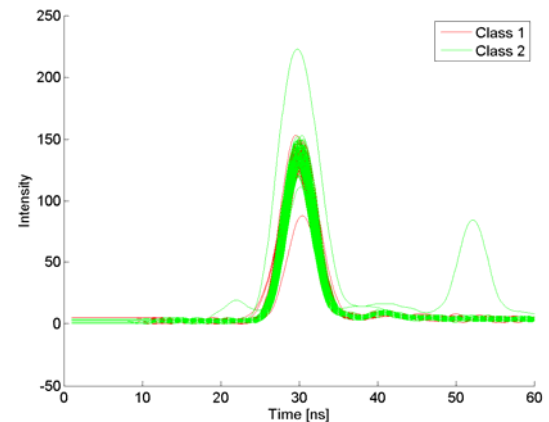
(a) Confusion matrix of overall data



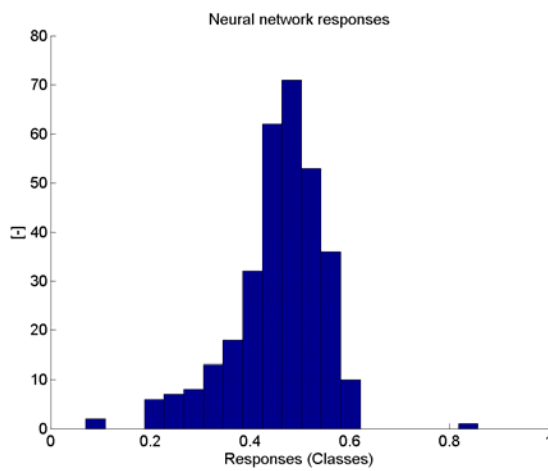
(b) Confusion matrix of training set



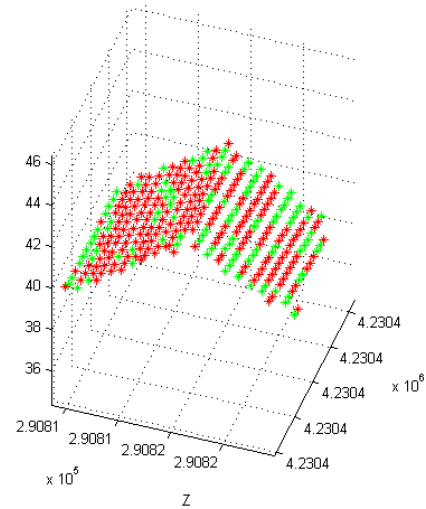
(c) Confusion matrix of validation set



(d) Translated sample vectors (waveforms)



(e) Histogram of the Neural network



(f) Classified points in the 3D space

Figure 46 Neural network based classification performance

Discussion

Based on the test data set, the classification of the Gaussian parameters, extended with skewness and kurtosis, showed that the classification performance is at the same level as the error by choosing a class with flipping coins (50%). It indicates that these parameters are unable to predict the incidence angle. Using the sample vectors, a slightly better performance can be achieved, about ~60%, but it is still not an acceptable rate. Overall, the roof tests confirmed that no reliable results on the impact of incidence angle on the waveform can be obtained.

4.5.2 Clustering with SOM neutral network

After the negative outcome of the roof tests, a SOM neural network to detect any features in a larger dataset was used. Figure 47 shows this selected dataset, a 120 m long paved road. The surface of the road is nearly planar, the changes in elevation is less than 0.5 m. The scan direction was perpendicular to the road, and the scan angles vary between 11° and 21°. Here the objective is similar: (1) detecting the scan angle from waveform, and (2) the impact of the topography on the performance,

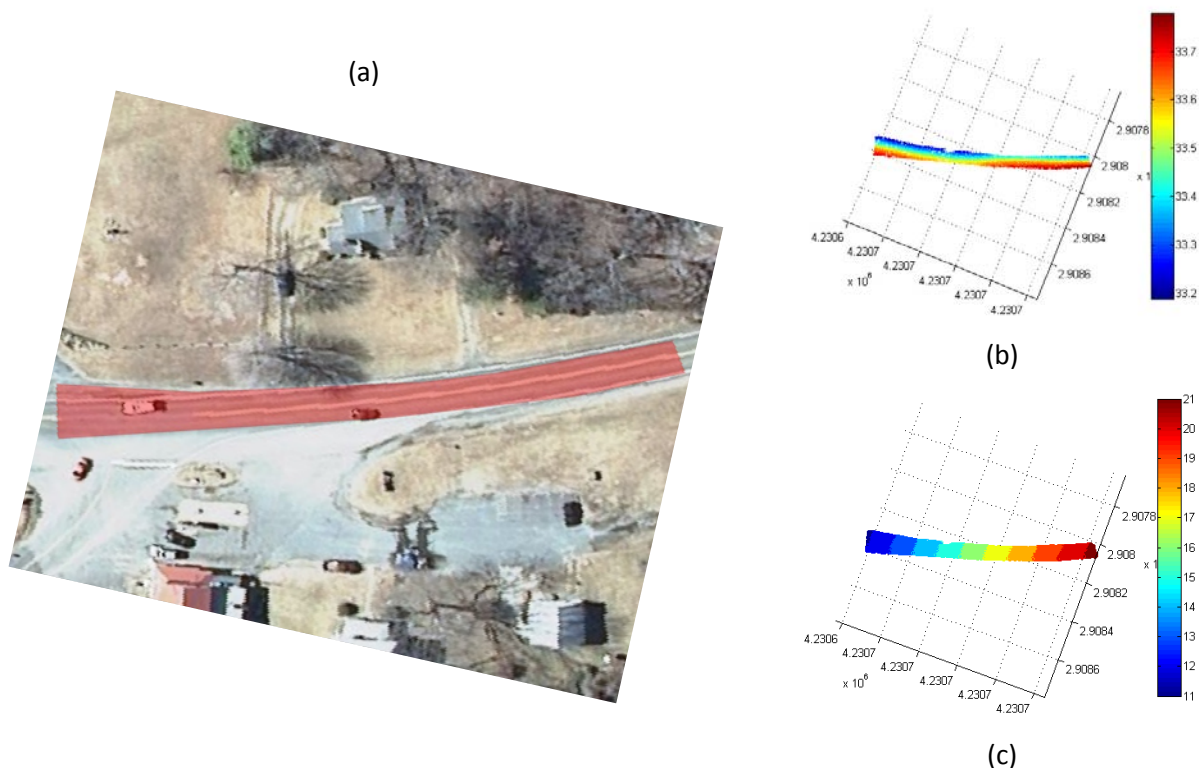
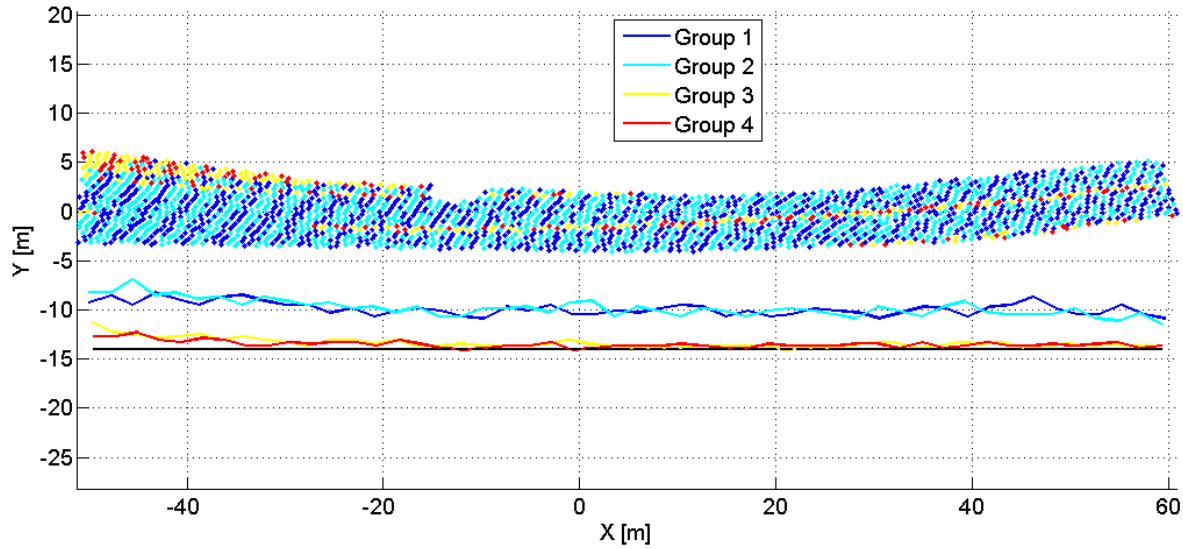


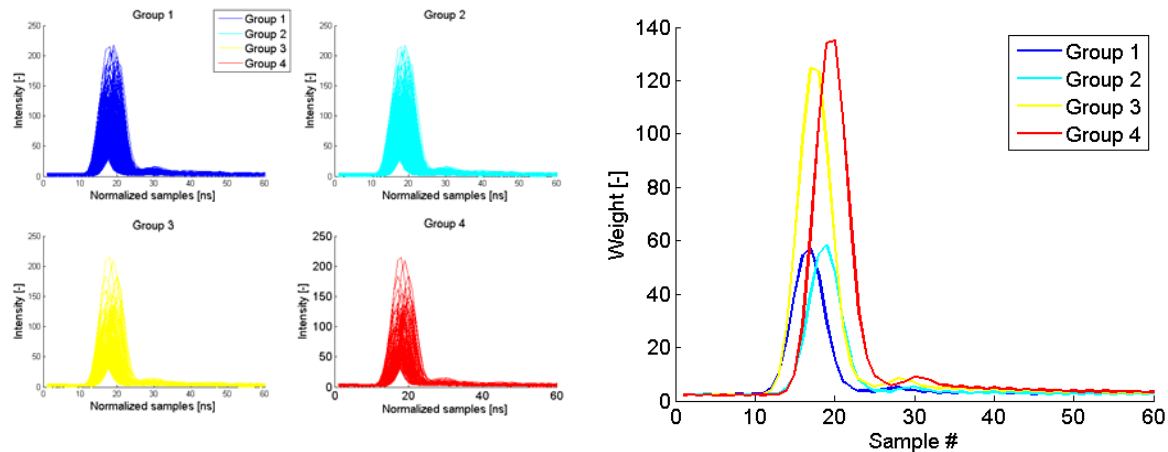
Figure 47 Road test area; orthophoto (a), altitude (b), and scan angle (c)

Using sample vectors

In our first approach, the original length sample vectors were used without any translation. The neural network was the same as it was introduced earlier. The neuron configuration was 2x2, which implies that 4 groups are determined by the SOM. The detected classes are shown in a local coordinate system in Figure 48.



(a) Result of SOM with the density of the class points in the cross section (lines)



(b) Original sample vectors by groups

(c) Weights

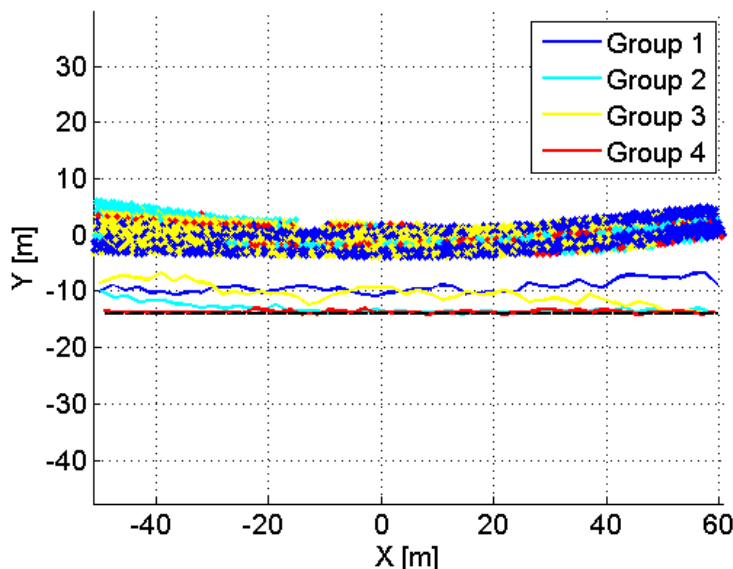
Figure 48 SOM result from original waveforms

In Figure 48, the lines between the 15 and -5 values of the Y axis show the class densities, the X axis is split to equidistance sections, and the number of the points within the classes is accumulated like a histogram. These lines indicate that the densities of the different points in the direction of X axis are uniform.

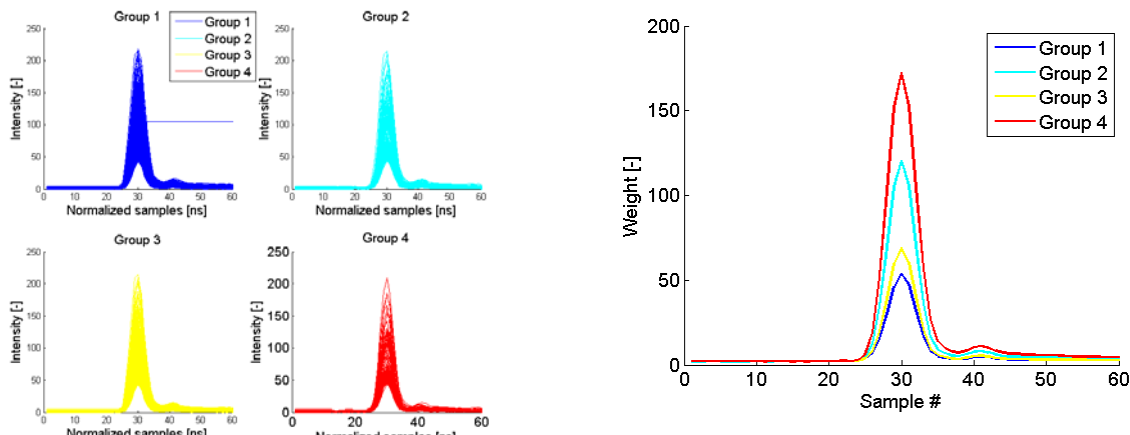
In Figure 48, the pavement markings on the road (Groups 3 and 4) and the road body (Groups 1 and 2) are easily distinguishable. In addition, a pattern is also noticeable in the data, see the waveforms regarding the groups in In Figure 48b and the weights provided by the SOM in Figure 48c. Note that the location of the maximum peaks of Groups 1 and 3 are different than in the case of Groups 2 and 4. We assume that these differences are caused by the measuring or the processing components of the LiDAR system, and it does not indicate any impact of incidence angle or other phenomenon.

Using translated sample vectors

In the next step, the translated sample vectors were applied to the same SOM network. Figure 49 shows the results of this test. Note that the patterns are disappeared, as expected. The Group 4 is clearly representing the pavement markings. Group 2 may be able to detect the topographic changes, compare this result to Figure 48b. The Group 3 and Group 4 may be interpreted as the detection of the changes of the scan. The density line of Group 3 shows that the numbers of the Group 3 points are higher at the beginning and it is decreasing, while the Group 1 point density is lower at the beginning and higher in the end. Note that the changes of the scan angles are in the X direction, see Figure 47c, and thus the Groups 3 and 4 may predict the impact of the incidence angle.



(a) Result of SOM with the density of the class points in the cross section (lines)



(b) Translated sample vectors by groups

(c) Weights

Figure 49 SOM result from translated waveforms

4.5.3 Land classification

The aim of this examination is to classify the waveforms by the backscattering object type. In this study, the five types of land categories are investigated. Figure 50 shows these categories: road1 (paved road), road2 (mud road), grass, building and tree.

The point clouds of these categories are selected by the area, as it is shown in Figure 50. Each point cloud needs to be corrected with removing those points that correspond to other category. Typically, the tree canopy can overlap to another land type area, and these points are removed. In addition, in the tree category, the grass is also removed. Note, in this study, the multiple detections are not used; they are known to be able to predict the laser beam backscattering from trees. Thus points with than one number of returns are eliminated. The return number is extricated from the LAS file. After removing these points, the laser beams in the tree category are supposed to be backscattered from the canopies.

The corrected point clouds can be seen in the Figure 51. These point sets are the classifier inputs and the categories are the classes. The aim of the investigation is to find the best classifier for predicting the class from the inputs.

Legend

- Paved road (road1)
- Dirt road (road2)
- Grass
- Tree
- Building



Figure 50 Land type categories (classes)

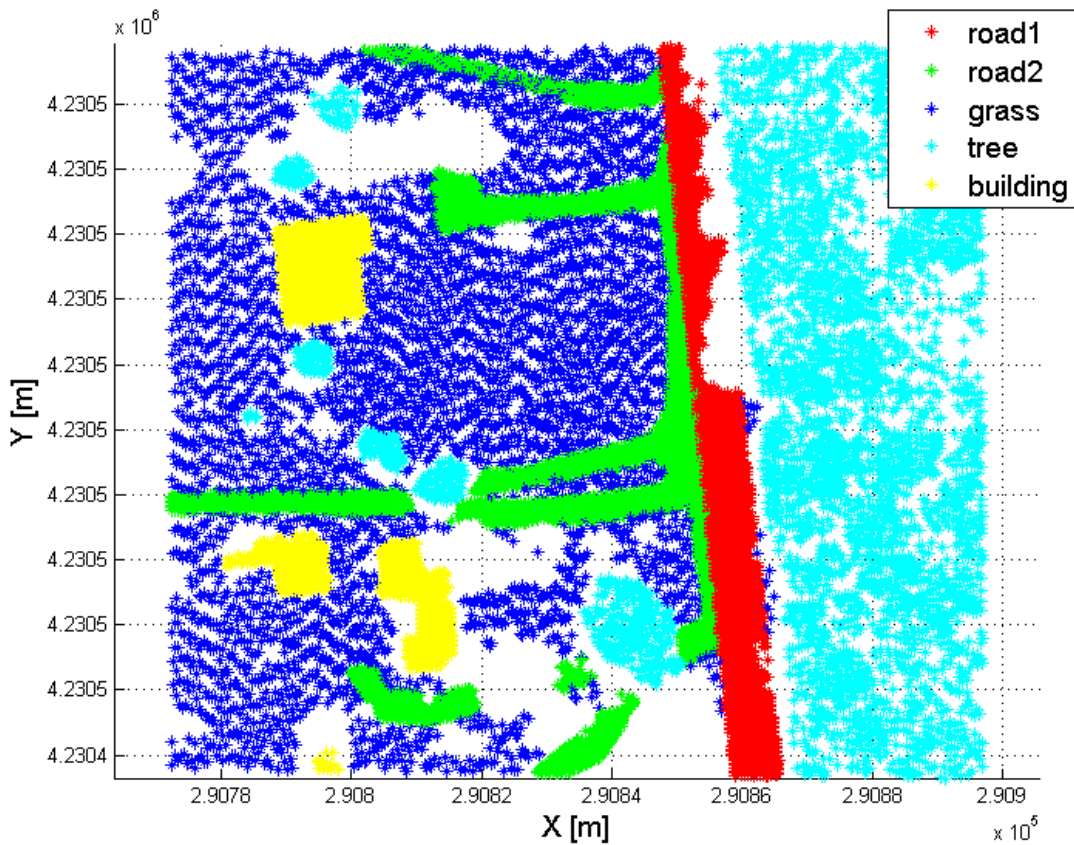


Figure 51 Land type classes after filtering

Median waveforms

First, the sample vectors of the classes were examined. The median waveforms from the 60 sample input for each class is shown in Figure 52. Note that the maximum intensity can be used for distinguishing some classes and that the standard deviation at each pulse is also large making the classification a challenge.

To compare the median sample vectors, see in the left part of Figure 53. The range of the median absolute deviation is depicted by the dashed lines. Clearly, the maximum intensity helps separate classes road2 and grass from classes road1, tree and building. Also note that the tree median sample also has a different tail shape than road1, road2 and the building. Unfortunately, this tail shape is similar to that of the road1, though the amplitude is lower. The two class regions of the median deviation are overlapping with each other, which can cause problems in the class

separation. Also note that the shape Gaussian parameter (p_5) is different in the road1 class than in any other classes.

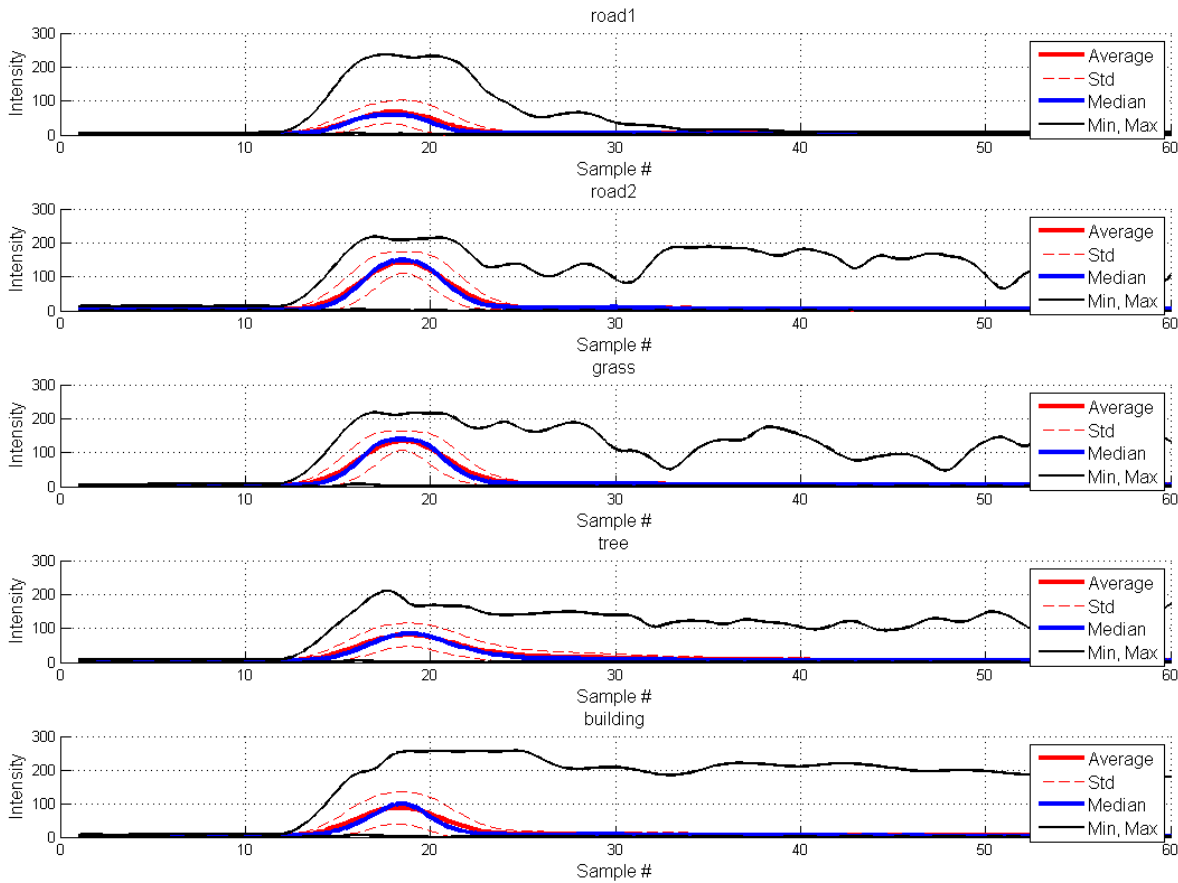


Figure 52 Statistics of sample vectors per class

The classification bases on these median waveforms are shown by the right part of Figure 53. Note that there is pattern not representing any categories. The same pattern was seen in the 4.5.2, Clustering with SOM neural network, section. Both observations confirm the use of the translated sample vectors instead of original sample vectors.

The median sample vector from the translated sample vectors can be seen in the Figure 54. Note that the shapes of the waveforms are nearly the same, suggesting that the maximum peak location difference is caused by the different shapes of median waveform from the original

sample vectors (presented in Figure 53). Also note that the distinguishable tail shape of the vectors from the tree class is still present.

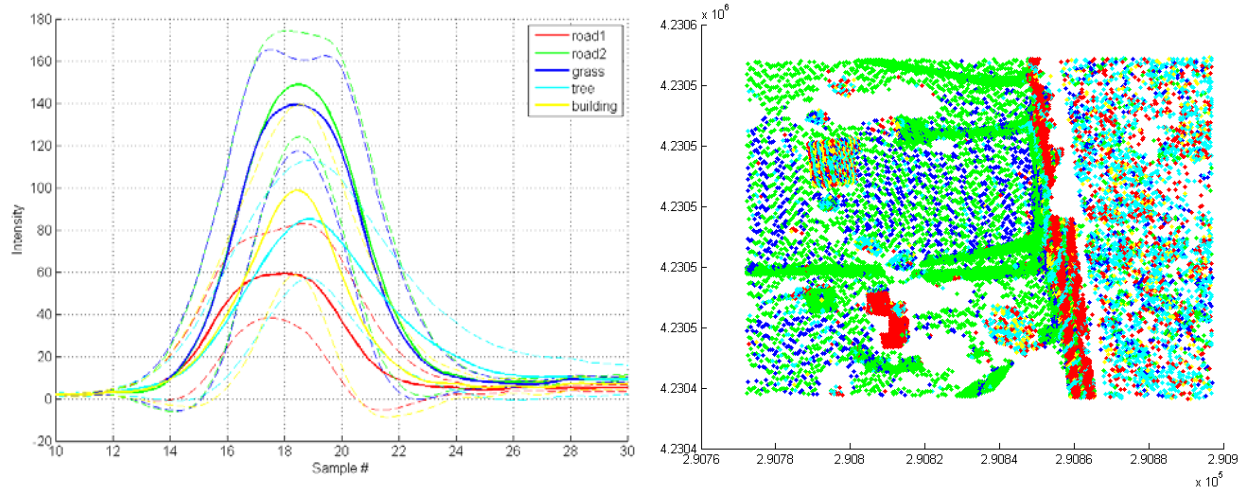


Figure 53 Median sample vectors from translated sample vectors samples (left), and the classification results (right)

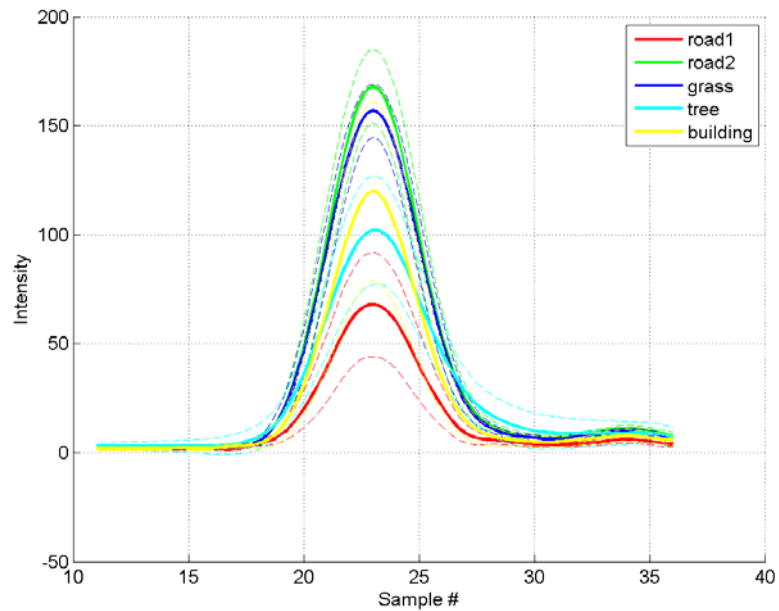


Figure 54 Median sample vectors from translated sample vectors

In the Figure 54, it is seen that the median standard deviation is still large, and they are overlapping each other. In order to determine how these median vectors describe the classes, the classification by these common waveforms is done. The distance between the samples and the median waveforms are measured by the maximum norm, because it is found to be the best distance definition in these circumstances. In order to increase the classification reliability, the approach presented in 4.4.1 section was extended: the minimal threshold is applied to accept if the sample belongs to the selected class. This threshold requires a minimal distance between the sample and the class to accept the class. The threshold is the N times the standard deviation of the distances. Those samples of which distances are larger than the threshold will not be classified.

The overall classification errors and the ratio of the positive and negative mismatches can be seen in Figure 55. On the X axis the N value shows the threshold and Y axis is the matching and mismatching ratios. Also shown is the number of the remaining sample numbers (i.e. data ratio), because increasing the threshold causes to decrease the number of those points that are able to be examined.

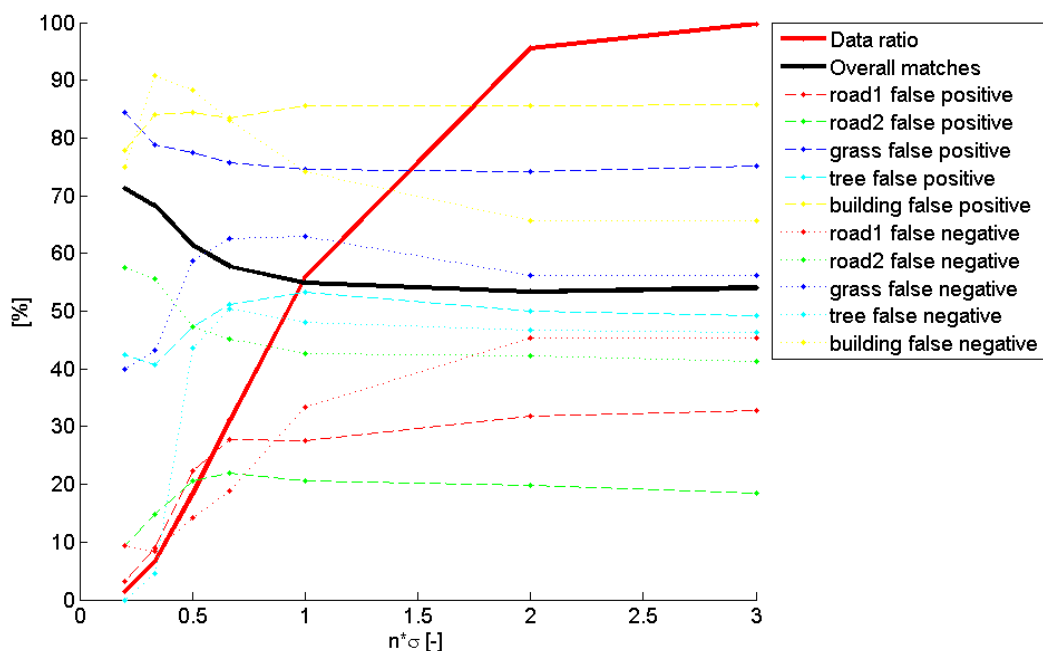


Figure 55 Distances from median waveform

Figure 55 shows that the ratio of the overall matches is 53% and it is increasing with decreasing the threshold.

The confusion matrices at no threshold (i.e. infinity threshold), 0.5 and 0.2 sigma are shown in the Table 20, Table 21, and Table 22, respectively. Note that without any threshold, the classification error is 54%. Note that it is already better than select the class randomly (20%). This error can achieve 71.3%, but note that practically the classifier only works for the road1, grass and tree classes. The results at other thresholds also indicate that this classifier only works correctly for these classes.

Table 20 Classification by the distance from the median waveform without threshold

	road1	road2	grass	tree	building	False negative
road1	2220 43.1%	269 2.3%	45 0.8%	625 9.9%	150 3.6%	32.9%
road2	128 1.3%	5126 51.8%	565 7.2%	351 3.7%	116 1.6%	18.5%
grass	41 0.5%	2525 25.5%	915 18.9%	178 2.5%	20 0.4%	75.1%
tree	761 10.7%	363 3.0%	372 6.8%	1927 35.2%	371 8.4%	49.2%
building	916 16.4%	458 4.3%	192 4.4%	519 9.4%	343 11.1%	85.9%
False positive	45.4%	41.4%	56.2%	46.5%	65.7%	54.0%

Table 21 Classification by the distance from the median waveform with at 0.5 sigma threshold

	road1	road2	grass	tree	building	False negative
road1	1124 68.9%	18 0.7%	5 0.3%	198 10.8%	101 6.3%	22.3%
road2	9 0.4%	591 46.3%	102 10.7%	21 1.6%	22 2.3%	20.7%
grass	6 0.3%	427 33.7%	129 17.1%	4 0.3%	5 0.6%	77.4%
tree	96 5.2%	54 3.2%	54 6.1%	328 37.5%	90 11.6%	47.3%
building	74 5.2%	32 2.5%	22 4.6%	30 4.1%	29 7.2%	84.5%
False positive	14.1%	47.3%	58.7%	43.5%	88.3%	61.6%

Table 22 Classification by the distance from the median waveform with 0.2 sigma threshold

	road1	road2	grass	tree	building	False negative
road1	125 88.0%	0 0.0%	0 0.0%	0 0.0%	4 3.0%	3.1%
road2	1 0.6%	39 40.6%	3 5.5%	0 0.0%	0 0.0%	9.3%
grass	1 0.5%	47 45.6%	9 14.1%	0 0.0%	1 1.5%	84.5%
tree	6 3.6%	6 5.0%	1 2.1%	19 57.6%	1 2.5%	42.4%
building	5 3.5%	0 0.0%	2 9.1%	0 0.0%	2 13.3%	77.8%
False positive	9.4%	57.6%	40.0%	0.0%	75.0%	71.3%

Gaussian parameters

In the next step, the extended Gaussian parameters and the kurtosis-skewness pairs were also examined. The histograms of the Gaussian parameters by the classes are shown in Figure 56. The histograms of the kurtosis and skewness values are in Figure 57.

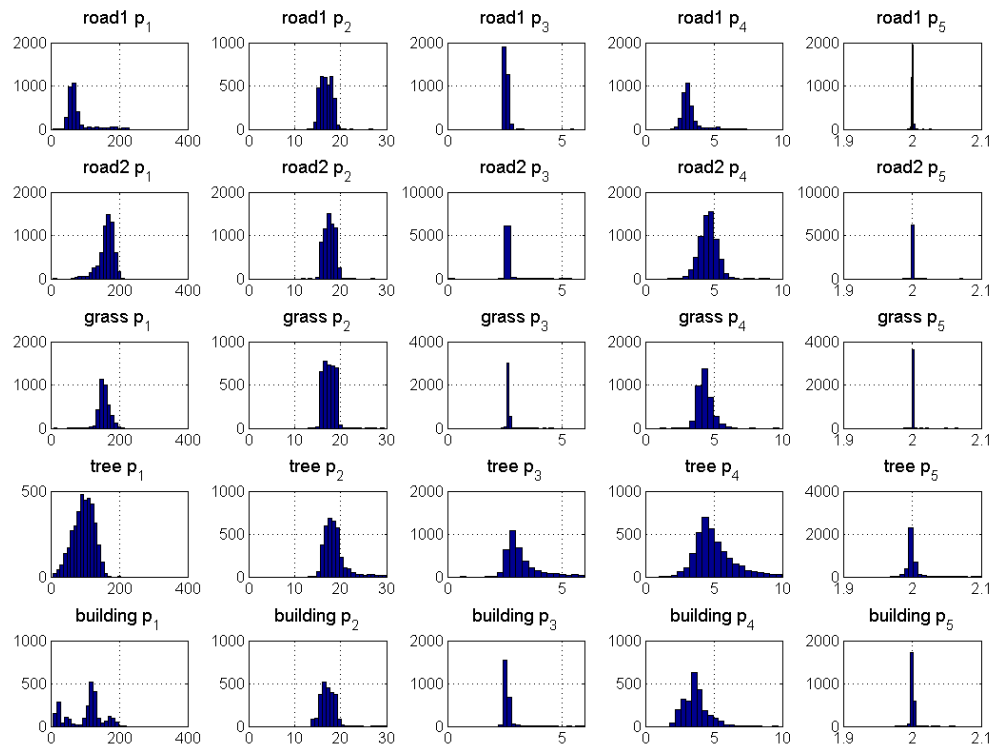


Figure 56 Histograms of the Gaussian parameters by the categories

The linear discriminant analysis (LDA) was applied on these parameters (Gaussian + kurtosis + skewness). The confusion matrix of the result is shown in Table 23. The total classification error (60%) provides slightly better results than the median waveform approach when no threshold is applied. Also this method can only distinguish the road1, road2 and tree classes; it cannot handle the classification of grass and buildings. The Gaussian parameters predict that the grass and the dirt road (road2) are same.

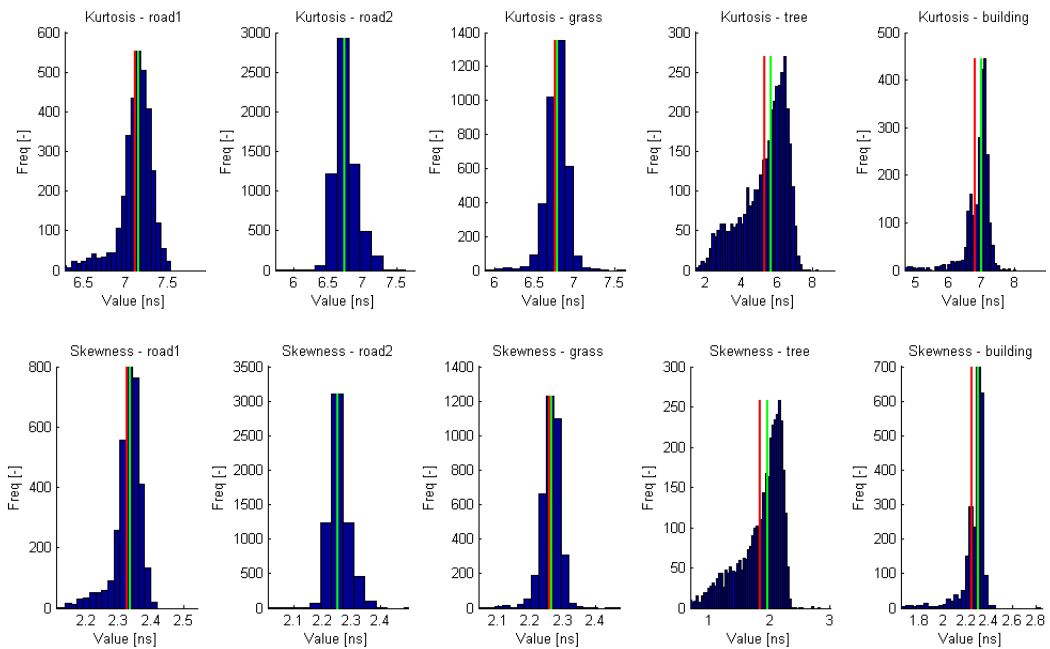


Figure 57 Kurtosis and skewness

Table 23 Linear discriminant analysis of the Gaussian parameters

	road1	road2	grass	tree	building	False negative
road1	2864 64.9%	367 2.5%	0 0.0%	12 0.2%	66 1.5%	13.4%
road2	131 1.3%	5956 50.1%	0 0.0%	57 0.6%	142 2.0%	5.2%
grass	17 0.2%	3602 30.9%	0 0.0%	45 0.7%	15 0.3%	100.0%
tree	216 2.9%	606 4.1%	0 0.0%	2624 64.4%	348 7.7%	30.8%
building	738 13.0%	1031 8.0%	0 0.0%	167 3.2%	492 16.4%	79.7%
False positive	27.8%	48.5%	0%	9.7%	53.7%	61.2%

SOM

Clustering the translated sample vectors provides better separation between grass and road1, and to select buildings. Two SOM configurations were tested. The first is 3x3, which creates 9 groups, and second is 2x2, which creates 4 groups. The results can be seen in Figure 58.

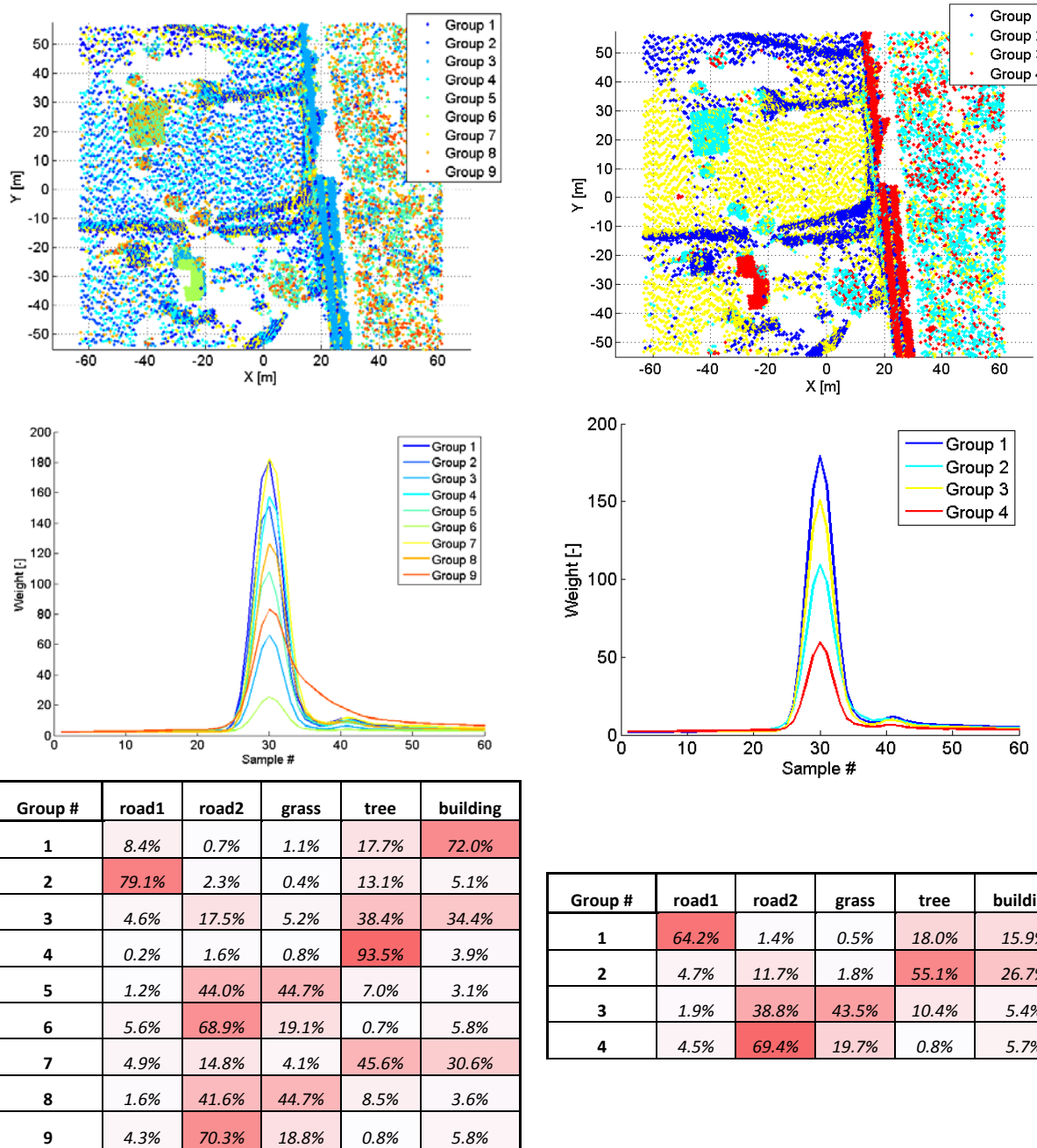


Figure 58 Land classification by SOM with 4x4 neuron configuration (left) and 2x2 neuron configuration (right)

The result matrix of the 4x4 SOM shows that Group 2 represents road1, Group 1 represents building, Groups 6 and 9 are road2. The estimation of the grass is available from Group 5 and Group 8. The misclassification of the grass can be decreased using the Groups 6 and 9, which indicate that the samples are from road2. The shape of the common sample waveforms (the weight vectors) shows that the shape of Group 8 is similar to that of the median waveforms with original sample vectors.

The 4 groups produced by 2x2 SOM also shows better classification performance between road2 and grass than the previous methods, but the results of other classes are worse. Overall, the SOM analysis claims that the main features of the waveforms are the value of the maximum intensity.

Combined method

The above presented three methods (median waveform distances, discriminant analysis and SOM) are combined to achieve the best performance. First, the algorithm uses Bayesian decision to classify the sample vectors. The Bayesian decision is based on the confusion matrix provided by the median waveform distance classifier and the discriminant analysis of the Gaussian parameters. After that, those points, which are selected as road2, will be classified again by the 2x2 SOM. In this step, the algorithm distinguishes road2 and grass. The last step will split the previously determined road1 class to road1 and building classes. The steps of the algorithm are presented by Table 24.

Table 24 Combined method

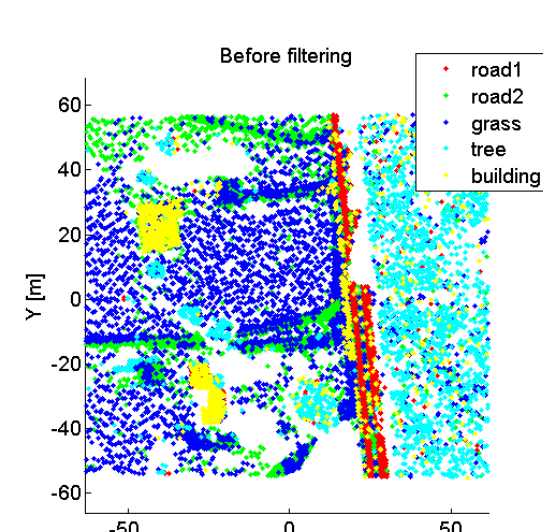
	Method	From	To
1	Bayesian decision using the confusion matrices of median waveforms and discriminant analysis	all vectors	road1, road2, grass, tree, building
2	Select grass points from road2 with 2x2 SOM	road2	road2, grass
3	Select building from road1 with 4x4 SOM	road1	road1, building

The dataset has been divided into train and validation set. The training set included the 70% of the total dataset and the validation set contained the remaining 30%. The confusion matrices that

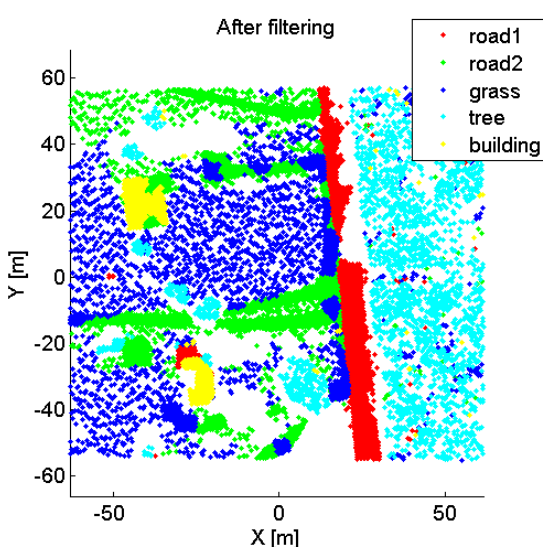
are used for the Bayesian decision and the SOM networks are calculated from the training set. The solution is tested on both sets. In order to improve the results, we applied a mode filter on the dataset. It corrects the class of single waveforms by the mode of the waveforms found within 3 m. Note that it already uses the location of the waveforms (i.e. 3D point), not just the shape, thus, it is an improved solution.

The results, shown in

Figure 59 and Figure 60 shows 65% classification error on the train and the validation set. After using mode filter, the performance can reach 73-75%. Also note that the diagonal elements of the confusion matrix contain the majority of the points within the classes, which means that the correct matches are dominant in each class.

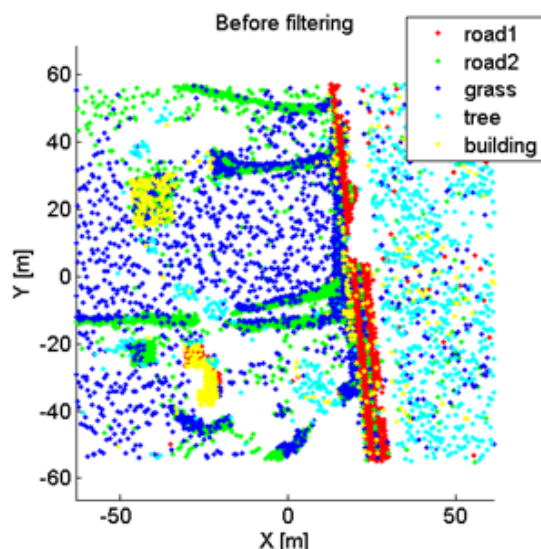


	road1	road2	grass	tree	building	False negative
road1	1909 74.7%	169 2.7%	87 1.4%	16 0.4%	135 4.0%	17.6%
road2	41 0.6%	2566 43.3%	1606 23.7%	50 0.8%	137 2.5%	41.7%
grass	6 0.1%	729 12.3%	1802 37.8%	26 0.5%	12 0.3%	30.0%
tree	83 1.8%	124 1.9%	285 4.5%	1991 68.7%	173 4.7%	25.0%
building	111 3.0%	502 9.5%	216 3.9%	149 3.9%	721 33.4%	57.6%
False positive	11.2%	37.3%	54.9%	10.8%	38.8%	65.9%

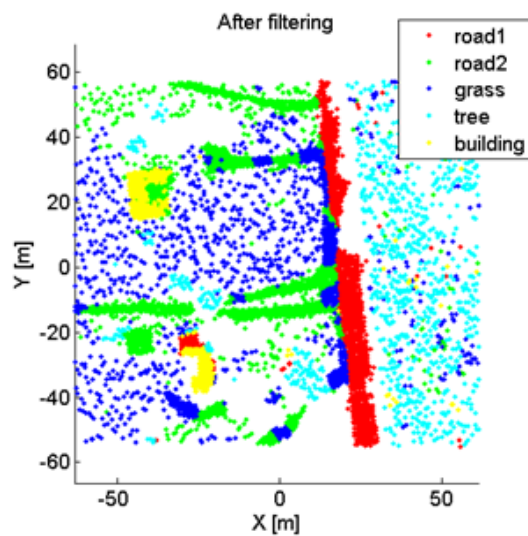


	road1	road2	grass	tree	building	False negative
road1	2294 82.5%	6 0.1%	16 0.3%	0 0.0%	0 0.0%	0.9%
road2	272 3.9%	2925 51.0%	1202 18.9%	0 0.0%	1 0.0%	33.5%
grass	27 0.5%	765 12.6%	1777 44.8%	3 0.1%	3 0.1%	31.0%
tree	22 0.4%	34 0.5%	143 2.5%	2435 88.9%	22 0.6%	8.3%
building	145 3.4%	525 9.7%	31 0.6%	81 2.0%	917 53.2%	46.0%
False positive	16.9%	31.3%	43.9%	3.3%	2.8%	75.8%

Figure 59 Results on the training set before applying mode filter (top) and after if (bottom)



	road1	road2	grass	tree	building	False negative
road1	815 73.6%	72 2.7%	39 1.4%	7 0.4%	60 4.2%	17.9%
road2	21 0.8%	1097 43.2%	693 23.6%	16 0.6%	59 2.5%	41.8%
grass	3 0.1%	298 11.7%	778 37.5%	17 0.8%	8 0.5%	29.5%
tree	41 2.0%	64 2.3%	138 5.0%	827 67.0%	68 4.3%	27.3%
building	49 3.0%	217 9.6%	100 4.2%	57 3.6%	306 33.1%	58.0%
False positive	12.3%	37.2%	55.5%	10.5%	38.9%	65.4%



	road1	road2	grass	tree	building	False negative
road1	981 81.5%	1 0.0%	11 0.5%	0 0.0%	0 0.0%	1.2%
road2	112 3.8%	1243 49.6%	530 19.1%	0 0.0%	1 0.0%	34.1%
grass	10 0.4%	336 12.8%	755 42.8%	2 0.1%	1 0.1%	31.6%
tree	27 1.2%	50 1.7%	105 4.3%	935 79.4%	21 1.4%	17.8%
building	61 3.3%	231 9.8%	15 0.7%	37 2.2%	385 51.2%	47.2%
False positive	17.6%	33.2%	46.7%	4.0%	5.6%	73.5%

Figure 60 Results on the validation set before applying mode filter (top) and after if (bottom)

5. LiDAR SYSTEM PERFORMANCE COMPARISONS

As LiDAR technology continues to develop, new approaches, such as CW FM LiDAR (Continuous Waveform Frequency Modulated), are introduced and improved hardware solutions are used in the next generation of LiDAR systems. Research started to investigate the impact of the new solutions on waveform formation and analysis. The lack of funding prevented to completion of this task, but two areas have been partially pursued under other projects:

- The CW FM system from Bridger Photonics is of interest because of the expectation that this approach may provide better penetration capability for certain materials, such as modestly transparent plastic, glass, and other materials. In addition, this sensing approach provides Doppler observations that could be beneficial to separate static and moving objects in the image area.
- LiDAR systems are performance validated using ground control, mainly certain materials arranged in simple geometrical shapes; for example, circular targets with material characterization. Since it is difficult to provide identical object space environmental conditions to repeat tests, variation system performance is rarely validated. Therefore, it was of great interest to analyze LiDAR data simultaneously acquired by two different LiDAR systems.

A peer-reviewed conference paper and a presentation on Bridger Photonics CW FM system, HRS-3D-1W, providing a comparison to other sensors, and a journal paper using the two simultaneously acquired LiDAR datasets, focused on the compression aspect of LiDAR waveform, are included in the Appendix.

6. CONCLUSION AND FUTURE TASKS

In these investigation data acquired by a Riegl VZ400 digitizer with 2 ns sampling rate was used. Our theoretical investigation shows that in the 300-600 m instrument-to-target range, the impact of the incidence angle is in the ~0.6-1.2 ns range that is not easily detectable with this somewhat modest sampling rate. Note that airborne scanners typically work with 1 ns sampling rate (or sometime with 0.5 ns), in which case, the incidence angle can be reasonable estimated.

Despite the less than ideal sampling rate of the waveform, the investigation results suggest that the incidence angle can be determined with an approximately 10° standard deviation.

For material identification/detection, the reflectance properties of the target object were examined. In ScanPos2 and ScanPos3 datasets, a small variety of materials was represented. Using a simple method based on the distance between an incoming waveform and the average waveform, 2-3 reflectance classes could be easily differentiated, with classification preformance of 93.1% reliability.

The based on the experiences so far, the validity of the algorithms has been checked and modest results have been achieved, which is due to the modest sampling rate of the waveform. Note that the footprint size is also part of the problem, as the impact of incidence angle as well as material properties depends on the divergence of the laser beam. For better testing the methods, additional measurements are required, and arrangement is in place to acquire airborne waveform data simultaneously collected by three scanners.

With the arrival of two new data sets, acquired by two different airborne scanners, the investigation continued on assessing the classification performance of waveform exploitation. The current results indicate that the conditions of normal airborne data acquisitions is harsher compared to the test environment, and, consequently, not all the results can be achieved at the level of the controlled environment tests. Increasing the algorithmic complexity, however, the classification results can improve.

7. REFERENCES

Brodu, N., D. Lague: 3D Terrestrial lidar data classification of complex natural scenes using a multi-scale dimensionality criterion: applications in geomorphology.

Hartzell, P. J., C. L. Glennie: Calibration of a terrestrial full waveform scanner, ASPRS Annual Conference, Baltimore, MD, 2013

Laky, S., Zaletnyik, P., Toth, Ch. and Molnar, B., (2012): Sparse Representation of Full Waveform LiDAR Data, proceedings of IGARSS 2012, Munich, Germany, July 23-27, 2012.

Molnar, B., Laky, S., and Toth, Ch. (2011): Using Full Waveform Data in Urban Areas, proceedings of *Photogrammetric Image Analysis* (PIA 2011), *International Archives of Photogrammetry and Remote Sensing*, Vol. XXXVIII, 3/W22, pp. 203-208.

Toth, C.K., Grejner-Brzezinska, D., Molnar, B., and Zaydak, A. (2012): Calibrating the MS Kinect Sensor, ASPRS Annual Conference, Sacramento, CA, March 19-23, 2012, CD-ROM.

Toth, C.K., Zaletnyik, P., Laky, S., Grejner-Brzezinska, D. (2011): The Potential of Full-Waveform LiDAR in Mobile Mapping Applications, 7th International Symposium on Mobile Mapping Technology, June 13-16, 2011, Cracow, Poland, CD ROM.

Toth, C.K., Grejner-Brzezinska, D., Laky, S., Zaletnyik, P. (2011a): Compressing LiDAR Waveform Data: Surface Classification and Peak Detection, ASPRS Annual Conference, Milwaukee, WI, May 1–5, 2011, CD-ROM.

Toth, C.K., Laky, S., Zaletnyik, P., Grejner-Brzezinska, D. (2011b): Classifying Compressed LiDAR Waveform Data, ASPRS Annual Conference, Milwaukee, WI, May 1–5, 2011, CD-ROM.

Toth, C.K. (2011): The Role of Surface Complexity in Airborne LiDAR Product Error Characterization, ASPRS Annual Conference, Milwaukee, WI, May 1–5, 2011, CD-ROM.

Toth, C.K., Zaletnyik, P., Laky, S., Grejner-Brzezinska, D. (2011c): Peak Detection From Full-Waveform LiDAR Data, International LiDAR Mapping Forum, New Orleans, Louisiana, 7-9 February, 2011, CD ROM.

Toth, C.K., Koppanyi, Z., Laky, S., Anderson, J., Massaro, R., (2013): The Impact of Incidence Angle on LiDAR Waveform, Ca/GIS ASPRS 2013 Specialty Conference, San Antonio, TX, 27-30 October 2013.



8. APPENDIX

8.1 ISPRS Technical Commission I Symposium, Denver, CO, November 17-20, 2014

A COMPARATIVE STUDY BETWEEN FREQUENCY-MODULATED CONTINUOUS WAVE LADAR AND LINEAR MODE LIDAR

R. D. Massaro^a, J. E. Anderson^{a,*}, J. D. Nelson^a, J. D. Edwards^a

^a Remote Sensing and Fluorescence Spectroscopy Lab,
US Army Corps of Engineers ERDC,
7701 Telegraph Road Alexandria, Virginia 22315 - John.Anderson@usace.army.mil

Commission VI, WG VI/4

KEY WORDS: LiDAR, LADAR, range resolution, laser, terrestrial scanning, frequency-modulated, continuous wave

ABSTRACT:

Topographic Light Detection and Ranging (LiDAR) technology has advanced greatly in the past decade. Pulse repetition rates of terrestrial and airborne systems have multiplied thus vastly increasing data acquisition rates. Geiger-mode and FLASH LiDAR have also become far more mature technologies. However, a new and relatively unknown technology is maturing rapidly: Frequency-Modulated Continuous Wave Laser Detection and Ranging (FMCW-LADAR). Possessing attributes more akin to modern radar systems, FMCW-LADAR has the ability to more finely resolve objects separated by very small ranges. For tactical military applications (as described here), this can be a real advantage over single frequency, direct-detect systems. In fact, FMCW-LADAR can range resolve objects at 10^{-7} to 10^{-6} meter scales. FMCW-LADAR can also detect objects at greater range with less power. In this study, a FMCW-LADAR instrument and traditional LiDAR instrument are compared. The co-located terrestrial scanning instruments were set up to perform simultaneous 3-D measurements of the given scene. Several targets were placed in the scene to expose the difference in the range resolution capabilities of the two instruments. The scans were performed at or nearly the same horizontal and vertical angular resolutions. It is demonstrated that the FMCW-LADAR surpasses the performance of the linear mode LiDAR scanner in terms of range resolution. Some results showing the maximum range acquisition are discussed but this was not studied in detail as the scanners' laser powers differed by a small amount. Applications and implications of this technology are also discussed.

1. INTRODUCTION

1.1 Background

Pulsed light detection and ranging (LiDAR) systems for terrestrial surveying and topographic mapping have made great strides in the past 10 to 15 years. Although terrestrial laser scanning was first used in the 1960's(Shan and Toth, 2009), only recently have the scanning mechanisms and computer hardware advanced enough to support topographic measurements within a reasonable amount of time. Terrestrial LiDAR instruments are now able to collect millions of accurately georegistered points within several seconds. While pulsed LiDAR technology is certainly more mature than other approaches, frequency-modulated continuous wave (FMCW) laser detection and ranging (LADAR) is rapidly gaining ground due to several key benefits. First and most evident, is the difference in range resolution between the two technologies. Pulsed LiDAR is limited in range resolution by the width of the emitted laser pulse. A typical conventional LiDAR system emits Gaussian-shaped laser pulses. Meanwhile, FMCW-LADAR is limited in range resolution by the chirped bandwidth of the emitted beam(Reibel et al., 2014). An example of a chirped bandwidth from a FMCW-LADAR system can be seen in Reibel et al(Reibel et al., 2010), Figure 2. Secondly, FMCW-LADAR can detect doppler motions in the returned laser pulse. Finally, FMCW-LADAR requires less power to achieve range measurements or, conversely, can detect objects at a greater range than a pulsed LiDAR having the same power. In this study, the range resolutions of a conventional, pulsed LiDAR system and a FMCW-LADAR system are compared and contrasted using real-world targets.

1.2 Instrument specifications

The instruments used in this comparison experiment were a Riegl VZ-400 3D terrestrial laser scanner and a Bridger HRS-3D-1W imager. The VZ-400 is a conventional, pulsed Class I scanning laser system with a 360° horizontal and 100° vertical field-of-view (FOV). The HRS-3D is a FMCW Class IIIb scanning laser system with a 360° horizontal and 60° vertical FOV. The physical dimensions of the scanner heads are very similar (see Table 1). The HRS-3D has a separate processing unit whereas the VZ-400 performs its processing within the scanner unit. The HRS-3D weighs about twice as much as the VZ-400 and requires about 3 times as much power. Both scanners are easily tripod mounted.

The VZ-400 and HRS-3D lasers both emit at 1.55 μm . The maximum pulse repetition rates for the VZ-400 and HRS-3D are 300 kHz and 48 kHz, respectively. The beam divergences for the VZ-400 and HRS-3D are 0.35 mrad and 0.1 mrad, respectively.

	Riegl VZ-400	Bridger HRS-3D
Scanner head (h x dia)	31 cm x 18 cm	28 cm x 20 cm
Processor size	None	48 cm x 43 cm x 23 cm
Weight	9.6 kg	19 kg
Power	65 W	350 W

Table 1: Size, weight, and power comparisons of the two scanners

*Corresponding author.

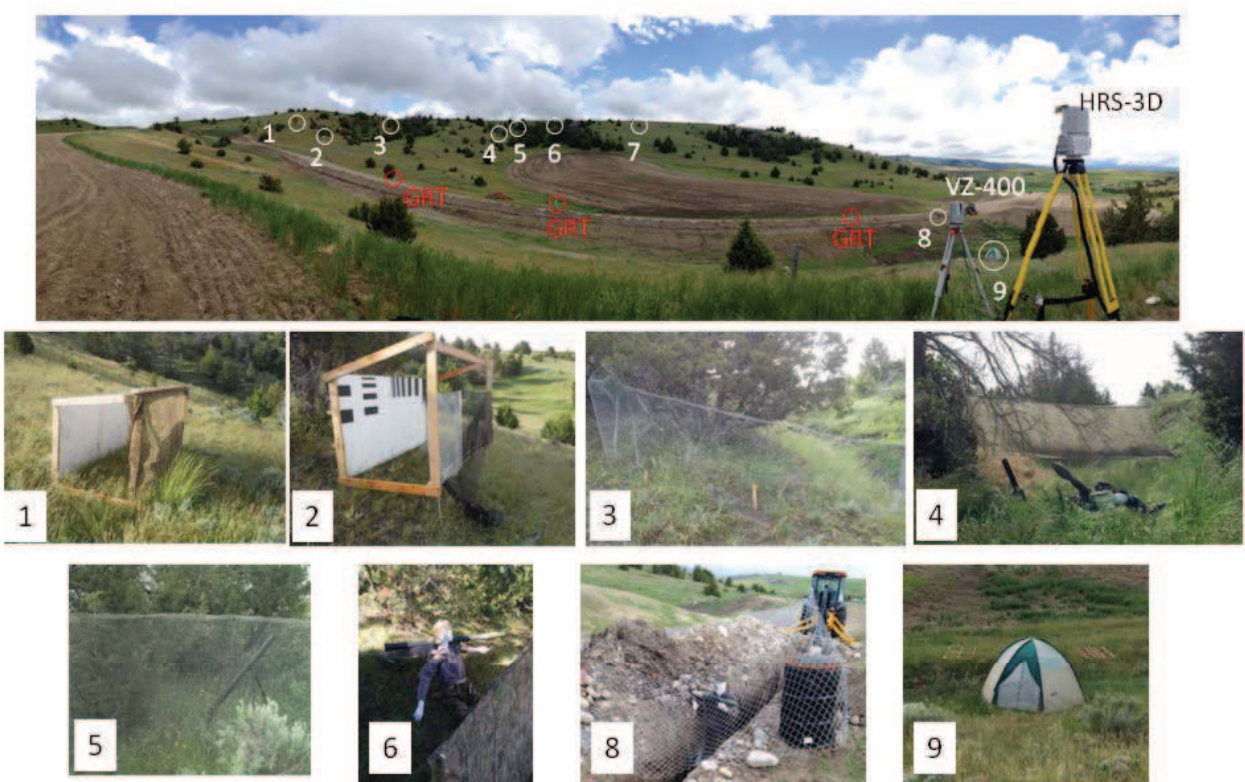


Figure 1: (Top) Overview of scan area and target placements (Middle and bottom rows) Images of targets [No image of target 7 available]

2. DATA COLLECTION

For this series of tests, we explored a variety of tactical scenarios and targets of interest to compare and contrast the technologies. A data acquisition site was chosen at approximate coordinates: 45.661°N, 111.345°W. The site is approximately 14 miles west of Bozeman, MT. A Riegl VZ-400 terrestrial laser scanner and a Bridger Photonics HRS-3D-1W terrestrial laser scanner were mounted on tripods and placed side-by-side (Figure 1, top). Several targets were placed in the scene. Targets 1 through 7 were placed at ranges between approximately 200 and 250 meters. Targets 8 and 9 were placed at 68 m and 45 m, respectively. The targets were designed to simulate sniper blinds and to test the range ambiguity issues that typically arise in direct detect systems. The targets also were designed to evaluate the obscurant penetration ability of the scanners. Camouflage netting and various types of fencing were used to obscure targets. A list of the targets, their descriptions, and their ranges from the scanners are shown in Table 2.

The scans from both instruments were performed with the measurement angular resolution set at $0.001^\circ \times 0.001^\circ$. The exception was for Target 9 which was scanned at a $0.005^\circ \times 0.005^\circ$ resolution. The target scans were not made simultaneously to avoid interference introduced by each of the system's lasers.

3. COMPARISONS

The range ambiguity and obscurant penetration performance of the two scanner technologies was explored. A test of the maximum range of the scanners was also made. The comparisons between the scanners on these topics are discussed in the following sections.

Target #	Range(m)	Description
1	220	Sniper blind with camouflage netting
2	185	Sniper blind with calibration pattern
3	249	Chicken wire near vegetation
4	232	Mesh screen
5	250	Chicken wire concealing mortar stand
6	253	Sniper blind concealing dummy with rocket launcher
7	238	Fencing in front of tree
8	68	Dummy in trench with covered with fencing
9	45	Tent concealing rifle on tripod

Table 2: Target descriptions and their ranges from the scanners

3.1 Range ambiguity

Targets 1 and 2 were chosen to study the range ambiguity of the scanners more in-depth. Target 1 was covered by a camouflage netting and had a wooden vertical support stand in front of a white painted background board. The front, central portion of Target 1

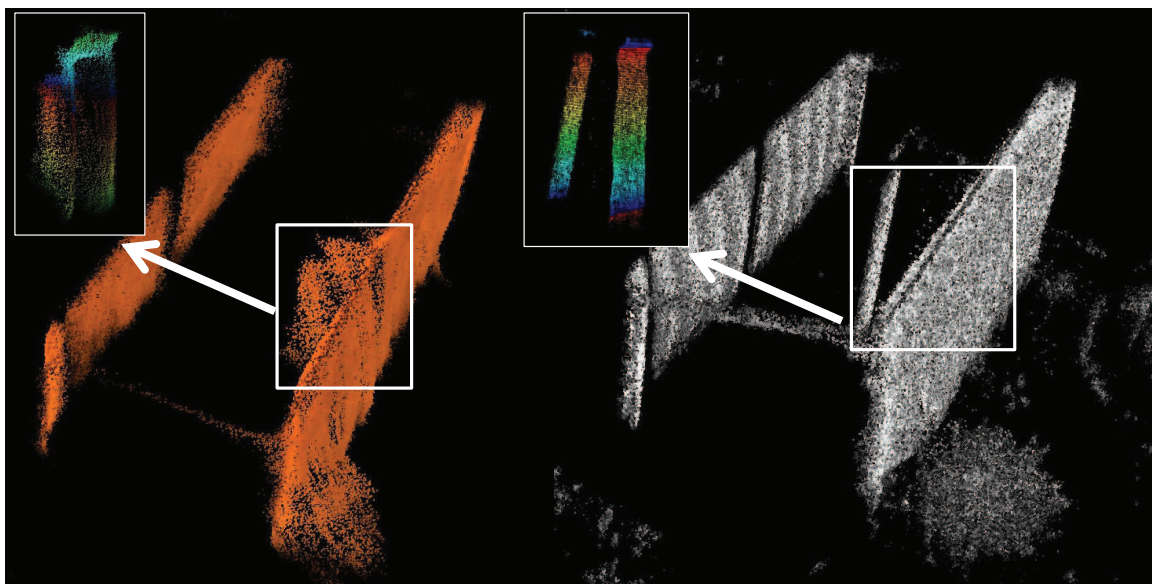


Figure 2: (Top) Point clouds of Target 1 from (left) VZ-400 and (right) HRS-3D. Insets show chosen point cloud subsets for further analysis.

was isolated for the following analysis of both point clouds as seen in the insets of Fig. 2. The histograms of Target 1's isolated range returns for the VZ-400 and HRS-3D is seen at top and bottom of Figure 3, respectively. There is a rather stark contrast between the two range return histograms. As can be seen in the top plot of the VZ-400 range return histogram, there are two range return peaks at approximately 220.6 m and 220.75 m, and a smaller, less distinct peak at approximately 220.95 m. The first two peaks are due to the netting on the left and right side of the vertical support. However, the netting directly in front of the support does not appear as a return in the data. Instead, the returns appear ambiguous as many are registered between the netting and support stand. The support stand itself is the ill-defined peak at 220.95 m.

Meanwhile, the HRS-3D returns rendered significantly, better-defined surfaces for the netting and vertical support. The netting surface is the peak at 221 m in the bottom histogram of Figure 3. The vertical support is the sharp peak at 221.5 m. There are only a few stray points which appear between the netting and vertical support surfaces in the HRS-3D data. These stray points are mainly located between ranges of 221.15 m and 221.35 m.

Two sections of Target 2 were chosen to compare the range ambiguities of the two scanners. The isolated sections are outlined in white boxes in 4 and the insets show the point cloud subsets. The first section included the double-layered mesh, vertical support, and backboard of Target 2. The range return histograms for the first section are shown in Figure 5 for the VZ-400 (top) and HRS-3D (bottom). Interestingly, the VZ-400 histogram shows 4 distinct peaks. The first peak at 184.5 m is due to the double-layered mesh surface. However, the double-layered mesh is not resolved by the VZ-400 into two separate surfaces. The second and third peaks are located at 185 m and 185.15 m, respectively. The double peaks here are due to the range "pulling" effect induced by the mesh. This effect is due (in part) to: 1) the inability of the linear mode system to resolve objects outside of its pulse bandwidth and 2) movement of the mesh material during the scan event. The upper portion of the vertical support has an unabated line-of-sight to the scanner while the lower portion has the double layer mesh intervening the scanner's line-of-sight to the vertical support. The mesh interference shifted the range return of the

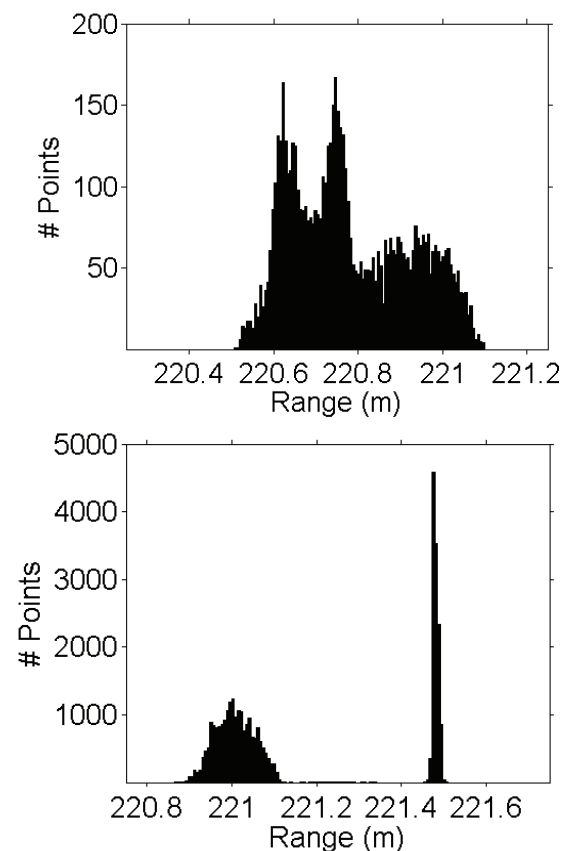


Figure 3: Range return histograms of Target 1 area for (Top) VZ-400 and (Bottom) HRS-3D

lower portion of the vertical support approximately 15 cm closer. The backboard return is located at approximately 185.7 m. There is also a considerable "filling-in" of returns between the mesh and vertical support in the VZ-400 data as can be seen between 184.5 and 185 m.

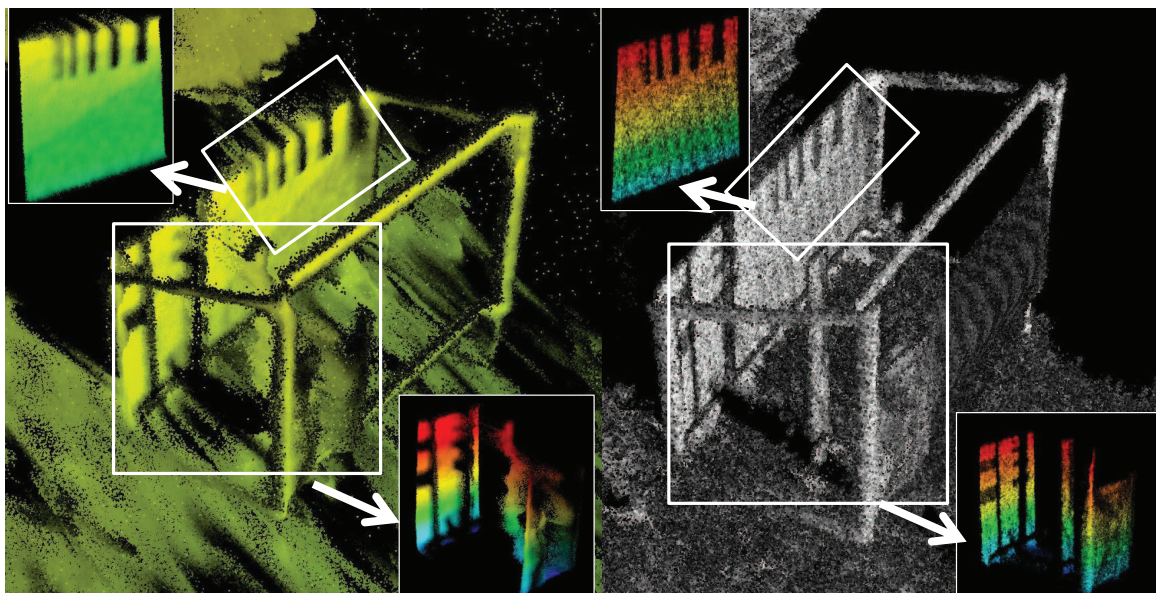


Figure 4: (Top) Point clouds of Target 2 from (left) VZ-400 and (right) HRS-3D. Insets show chosen point cloud subsets for further analysis.

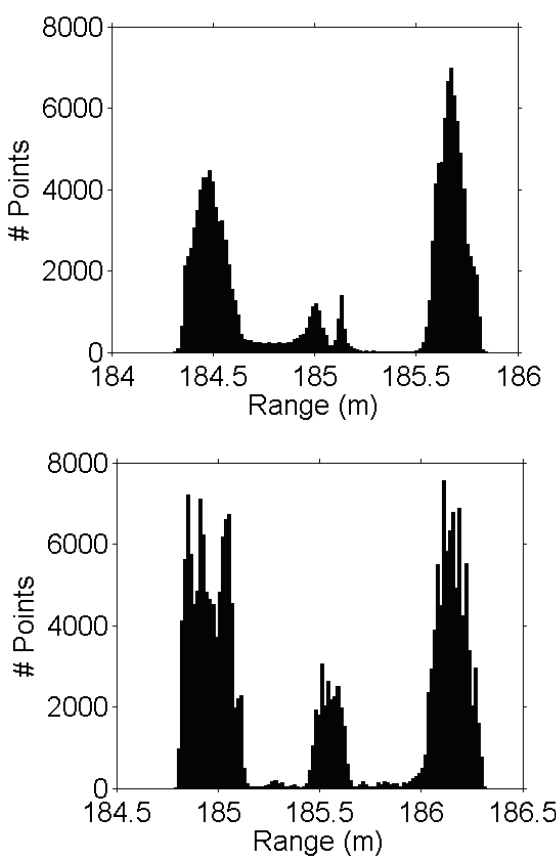


Figure 5: Range return histograms of Target 2 mesh, vertical support, and backboard for (Top) VZ-400 and (Bottom) HRS-3D

The HRS-3D data shows three distinct range return peaks around 185 m. Two of these are due to the double-layered mesh (a separation of only a few cm) while the third peak is due to the horizontal frame at the bottom of Target 2. The central vertical support at 185.55 m and the backboard at 186.2 m are both clearly defined

in the range returns. There are a few spurious returns in the HRS-3D data located at 185.3 m range. The fill-in observed between the vertical support and the backboard at ranges of 185.7 m to 186 m is due to low-lying vegetation.

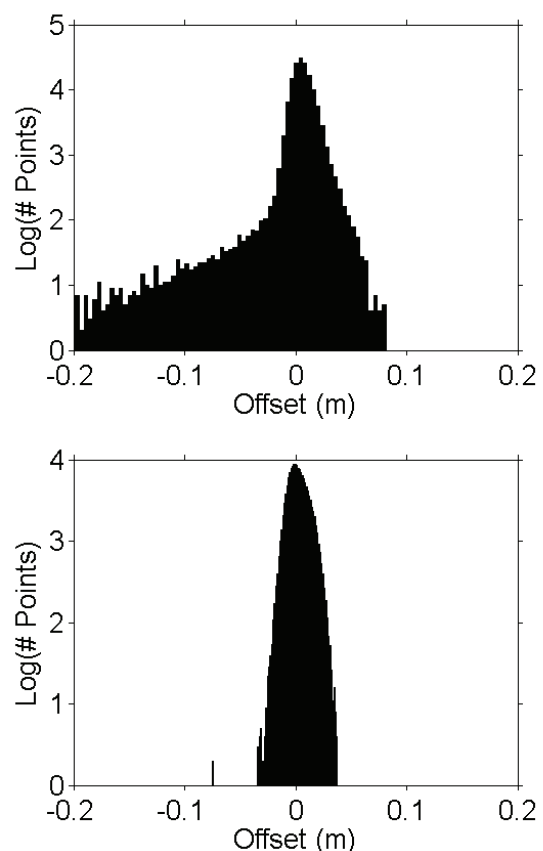


Figure 6: Log histograms of offset from Target 2 backboard for (Top) VZ-400 and (Bottom) HRS-3D

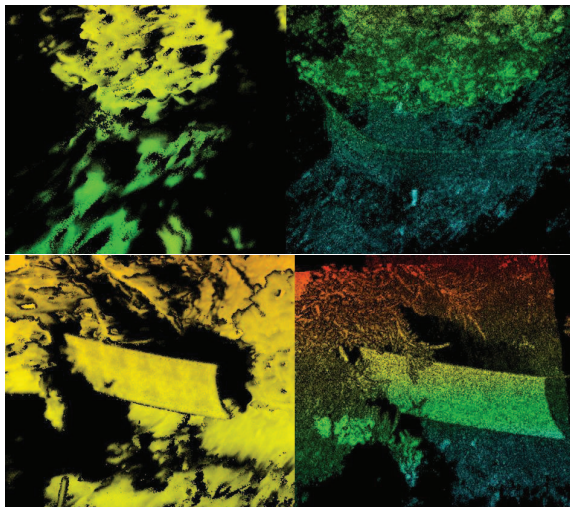


Figure 7: Point clouds of Targets 3 (top) and 4 (bottom), VZ-400 and HRS-3D point clouds are on the left and right sides, respectively.

The second section isolated from Target 2 is the backboard containing the vertical black resolution test lines as can be seen in Figure 4 top-left insets. For each of the sub-setted point clouds, a vertical plane was calculated to act as the geometrical representation of the backboard. The distance between the backboard plane and each point was then calculated. This distance is the offset between the 3-D data point and the vertical plane. Logarithm histograms of the distance offsets are shown in Figure 6 for the VZ-400 (top) and HRS-3D (bottom). Negative and positive distance offset values represent points behind and in front of the backboard from the scanners' viewpoints, respectively. The VZ-400 histogram shows a distinct negative offset shoulder. This is due to range ambiguities between the top of the backboard and a tree limb located approximately 0.5 m behind Target 2. The positive distance offset shoulder shows that the VZ-400 registered returns out to 8 cm in front of the backboard. Meanwhile, the HRS-3D histogram shows that there is no such range ambiguity between the backboard and the tree behind Target 2. Additionally, the distance offsets are confined to ± 5 cm from the backboard plane.

3.2 Obscurant penetration

In this section, the obscurant penetration performance of the two scanners is compared. Some of the differences have already been demonstrated from Targets 1 and 2 in the previous section. Figures 7 and 8 show the remainder of the targets' point clouds. The VZ-400 point clouds are on the left side while the HRS-3D point clouds are on the right side. In Target 3 (Figure 7 top), it can be seen that the VZ-400 point cloud (left) is far sparser than the HRS-3D point cloud (right) behind the chicken wire fencing. Low-lying vegetation can be seen in the HRS-3D data but is unrecognizable in the VZ-400 data. In Target 4 (Figure 7 bottom), it can be seen that both scanners could not easily achieve consistent penetration through the mesh screen. However, the HRS-3D was able to register approximately 10% of the total returns had the intervening screen not been present. The VZ-400 did not register any returns from behind the mesh screen. In Target 5 (Figure 8a), the VZ-400 did not register any returns from the mortar stand behind the chicken wire (see inset for top-down view. The HRS-3D was able to clearly resolve the mortar stand's two legs and barrel. In Target 6 (Figure 8b), the VZ-400 was unable to register the dummy with the rocket launcher behind the sniper blind. Inter-

estingly, however, the intensity image of the dummy's head and shoulders can be seen overlaid on the sniper blind. The HRS-3D was able to easily resolve the dummy's head, torso, and limbs and was able to resolve the barrel of the rocket launcher. Both scanners were able to easily penetrate the fencing of Target 7 (Figure 8c). However, the HRS-3D was slightly more successful than the VZ-400 at registering points on the actual fenceline. In Target 8 (Figure 8d), the VZ-400 was unable to geometrically resolve the dummy in the ditch under the fencing. However, similar to Target 6, the dummy's head appears as higher intensity points mapped onto the surface of the obscuring fenceline. The HRS-3D is able to geometrically resolve the dummy's head, torso, and arms. Finally, in Target 9 (Figure 8e), both scanners are able to penetrate the tent lining to resolve the propped-up rifle inside. The HRS-3D resolves features such as the scope and the shoulder strap. The VZ-400 does a better job at registering the intensity changes of the tent door flap.

3.3 Maximum range

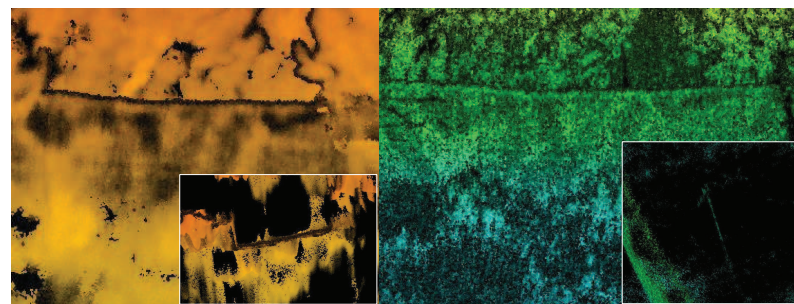
Several measurements were made in this study to assess the maximum range capabilities of the two scanners. The VZ-400 and HRS-3D were both capable of registering returns from highly reflective surfaces at a range of 900 m. The surfaces were primarily vegetation and thus possessed exceptional reflectance (0.7) at $1.55 \mu\text{m}$. The HRS-3D registered approximately twice as many returns than the VZ-400 at these long ranges.

4. ANALYSIS

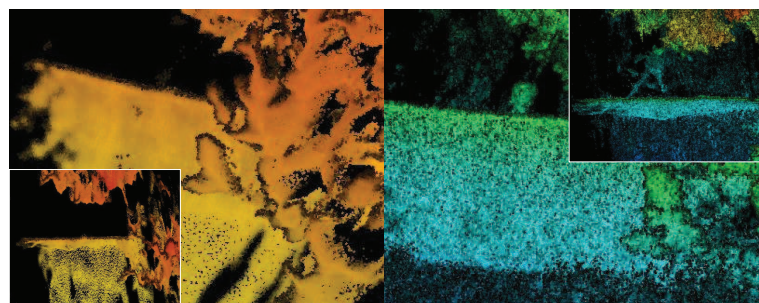
From the standpoint of tactical, military targeting and topographic rendition, it is clear from this study that the FMCW technology vastly improves range ambiguity and obscurant penetration of terrestrial laser scanners. The returns from closely spaced surfaces (down to approximately 10 cm in separation) are capable of being range-resolved by the HRS-3D. In contrast, the VZ-400 begins to experience range ambiguity problems when surface separations are at approximately 0.5 m or less. This is especially true for closely spaced surfaces at larger ranges, as can be seen in Targets 1, 2, 5, and 6. The VZ-400 tends to do a better job at range resolution and obscurant penetration when the targets are closer in range, as in Target 9. Interestingly, the VZ-400 scanner recorded higher intensity values from the concealed objects mapped onto the surfaces of the obscurants as in Targets 6 and 8. It may be the case that the concealed object's Gaussian return shoulder is having an additive effect to the obscurant's surface return. Yet, the concealed object's Gaussian peak is not strong enough to be registered as its own 3-D return by the sensor. It was also observed that the HRS-3D displayed remarkable vegetation feature resolution at larger ranges. Tactically, this is particularly important in foliage penetration(Massaro et al., 2012) and the rendition of camouflage. It is believed that FMCW-LADAR systems will be more adept at highly accurate vegetation mapping(Pirotti et al., 2013).

5. CONCLUSION

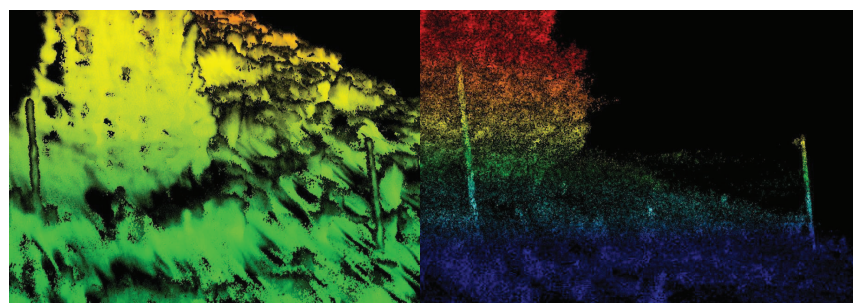
While the FMCW system certainly outperformed the conventional, pulsed system in terms of range resolution, obscurant penetration, and maximum range, there are some drawbacks to the FMCW system. It currently takes about six times as long for a 3-D scene to be acquired with the FMCW system. The FMCW scene acquisition time can likely be decreased however with improved FPGA boards and optimized scanning techniques. The size, weight, and power requirements of the FMCW system are also significantly



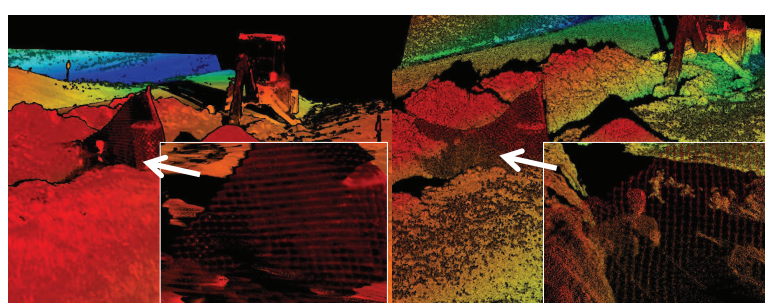
(a) Target 5 (insets are top-down views)



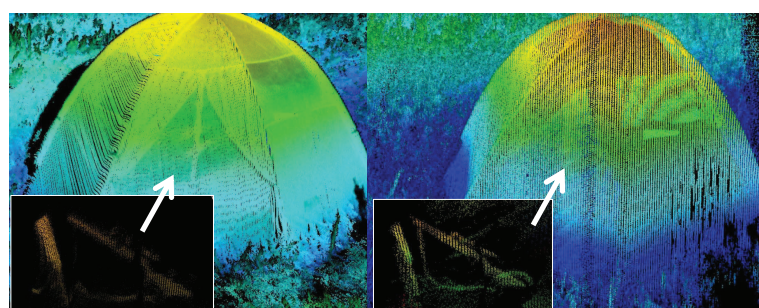
(b) Target 6 (insets are top-down views)



(c) Target 7



(d) Target 8 (insets show close-up of dummy location)



(e) Target 9 (insets show points from tent interior)

Figure 8: Point clouds of Targets 5 through 9 from top to bottom. VZ-400 and HRS-3D point clouds are on the left and right sides, respectively.

greater than the slimmer conventional system. However, this can be remedied by eventual inclusion of the processing unit into the scanner head.

As compared to heterodyne laser radar systems nearly 30 years ago (Keyes, 1986), FMCW-LADAR seems to have overcome many technological hurdles. In all, it seems clear that the future of terrestrial laser scanning, and possibly air- and space-borne LADAR, lies in FMCW systems. In addition to the superiority of their range resolution and obscurant penetration, FMCW systems can provide Doppler velocities and theoretically achieve greater maximum range given the same power input.

ACKNOWLEDGEMENTS

The authors are grateful to Dr. Randy Reibel, Jim Curry, Trent Berg, and the rest of the team from Bridger Photonics for their willingness and assistance in collecting and processing the test data.

REFERENCES

- Keyes, R. J., 1986. Heterodyne and nonheterodyne laser transceivers. *Review of Scientific Instruments* 57, pp. 519–528.
- Massaro, R., Zinnert, J., Anderson, J., Edwards, J., Crawford, E. and Young, D., 2012. Lidar flecks: modeling the influence of canopy type on tactical foliage penetration by airborne, active sensor platforms. In: *Airborne Intelligence, Surveillance, Reconnaissance (ISR) Systems and Applications IX*, Proc. SPIE, Vol. 8360, p. 836008.
- Pirotti, F., Guarneri, A. and Vettore, A., 2013. Ground filtering and vegetation mapping using multi-return terrestrial laser scanning. *ISPRS Journal of Photogrammetry and Remote Sensing* 76, pp. 56–63.
- Reibel, R. R., Greenfield, N. J., Berg, T. J., Kaylor, B. M. and Roos, P. A., 2010. Ultra-compact ladar systems for next generation space missions. In: *Conference on Small Satellites*, Vol. SSC10-I-9, pp. 1–11.
- Reibel, R. R., Roos, P. A., Kaylor, B. M., Berg, T. J. and Curry, J. R., 2014. Imaging through obscurants with a heterodyne detection-based ladar system. In: J. J. G (ed.), *Degraded Visual Environments: Enhanced, Synthetic, and External Vision Solutions*.
- Shan, J. and Toth, C. K., 2009. *Topographic Laser Ranging and Scanning: Principles and Processing*. CRC Press.

8.2 Research discussion presentation



Exploitation of Full-waveform LiDAR to Characterize/Exploit under Canopy Targets - Foliage Penetration (FOPEN)

LiDAR Sensor Comparison Study

Charles Toth and Dorota A. Grejner-Brzezinska

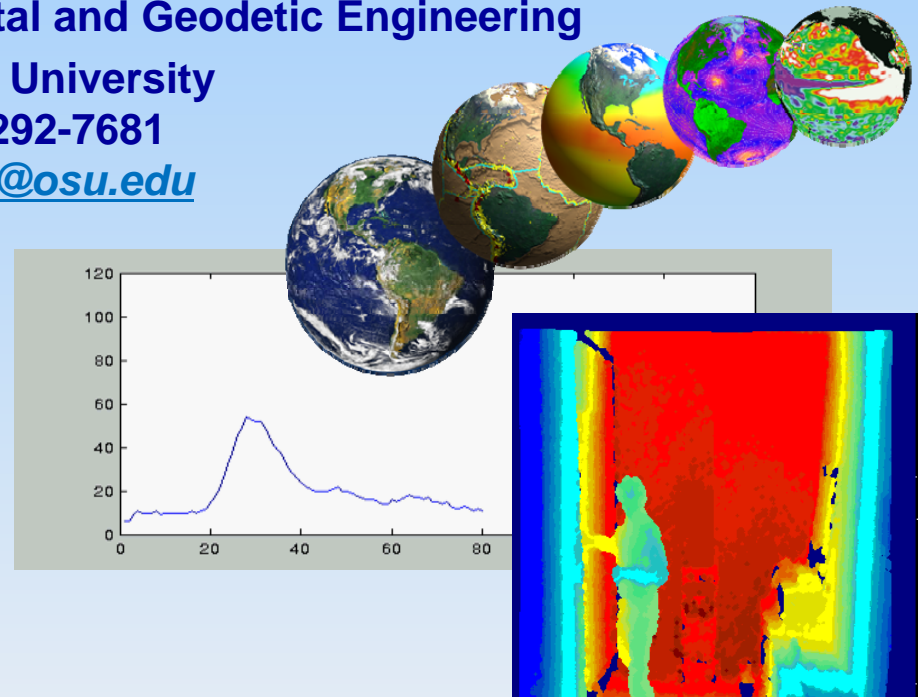
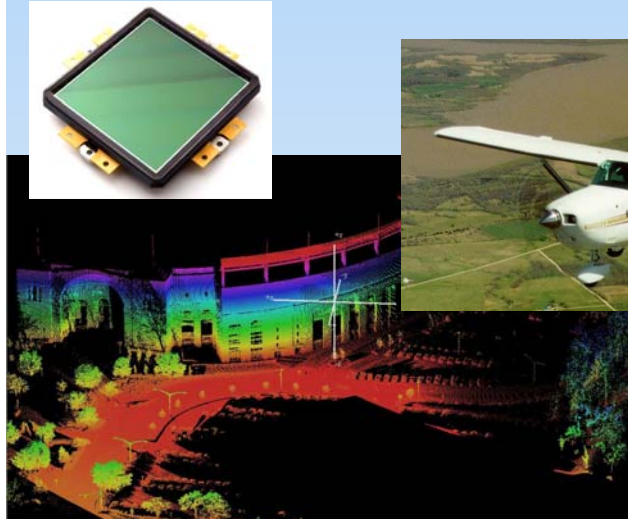
Satellite Positioning and Inertial Navigation (SPIN) Lab

Department of Civil, Environmental and Geodetic Engineering

The Ohio State University

Phone: 614-292-7681

E-mail: toth.2@osu.edu



Approach

Feasibility study to detect moving vehicles:

- ❖ Prototype/test a mobile, easily deployable sensor system
 - Main component: laser sensing technology
 - GPS-based georeferencing and time base
 - Optional optical sensing
- ❖ Acquire sample data
- ❖ Processing
 - Develop vehicle specific feature extraction algorithm to extract shape form laser point cloud
 - Parameterize extracted geometric parameters with accuracy term estimates
 - Estimate velocity and attitude of vehicle
 - Model vehicle trajectory
- ❖ Report on results and recommendations

Initial Sensor Platform and Configuration

- ❖ Install sensors in the OSU GPSVan
- ❖ High-performance georeferencing with data acquisition
- ❖ Suitable platform to install imaging sensors



- ❖ Multiple GPS antennae
- ❖ Roof platform for imaging sensors
- ❖ High-performance IMU sensors
- ❖ Data acquisition system, power

Laser Sensor Comparative Tests



- ❖ Laser technology is rapidly advancing
- ❖ Application specific sensors are introduced (UAS)
- ❖ Performance evaluation needed
 - to optimize sensor selection
 - to provide reference for low-end sensors
- ❖ Profilers/scanners considered:

SICK LMS30206



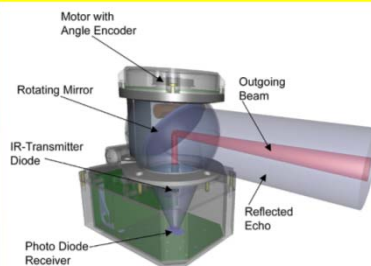
UTM-30LX-EW



Velodyne HDL-64E



Ibeo Alasca XT



Velodyne HDL-32E



Bridger's HRS-3D-1W



Test Site: OSU Airport

Site Location: OSU Airport

- ❖ RWY 9R-27L
 - 5002' X 150'
 - Precision Instrument Marking
 - Utilized by aircraft up to RDC C-III

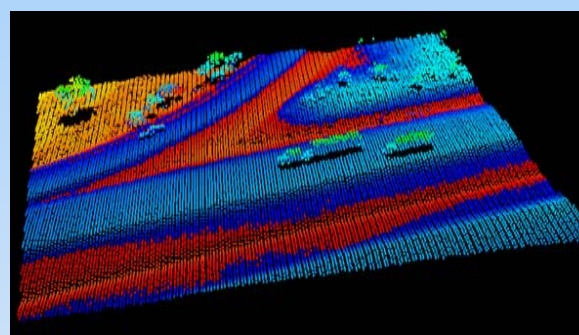


Some Characteristics of Laser Scanning

- ❖ Side effect: motion artifact; objects change shape based on relative motion between sensor and object



← Sensor motion



- ❖ Benefit: from motion artifact, shape deformation, relative velocity can be estimated (object shape must be known)

Some Aspects of Processing



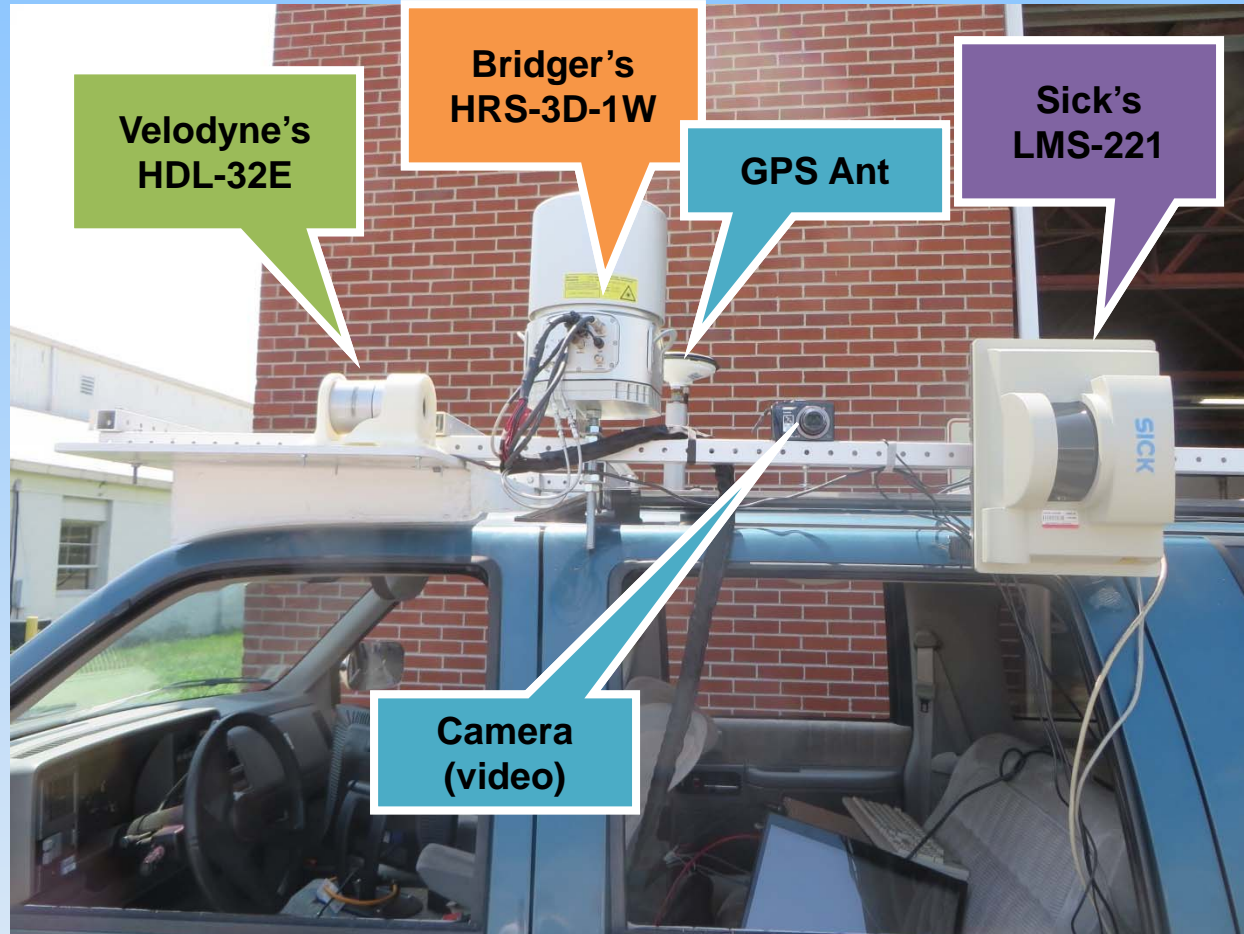
- ❖ Investigation of data acquisition and sensing properties
 - Point cloud generation
 - Range and surface dependency
 - Sample time dependency
 - Observability analysis
- ❖ Shape parameterization based on point cloud
 - Estimation accuracy
 - Shape matching
- ❖ Sensor network formation
 - Sensor synchronization
 - GPS-based georeferencing, calibration
- ❖ High-level processing
 - Combining multiple sensor data
 - Vehicle trajectory and velocity estimation

Team



- ❖ Field tests at Don Scott airport (OSU), August 6 and 8, 2014
- ❖ Crew: OSU and Asymmetric Inc., first user of Bridger's HRS-3D-1W

Sensor Configuration



Sensors' Specification



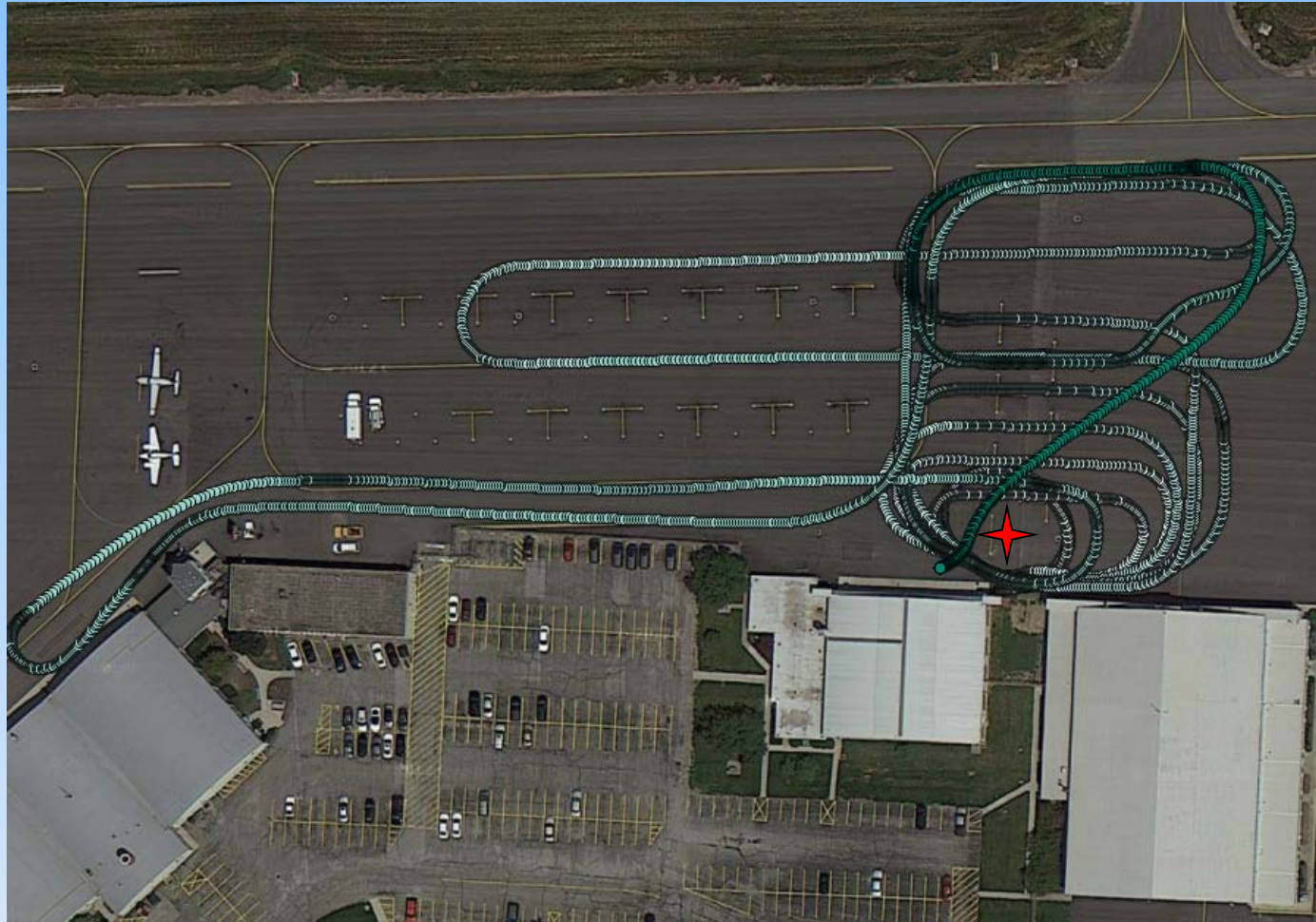
Name	LMS-221-30206	HDL-32E	HRS-3D-1W
Manufacture	SICK AG	Velodyne	Bridger Photonics Inc.
Data interface	RS232 or RS422	Ethernet cable (UDP/IP)	
Measuring	TOF	TOF	FM CW
Angular range	100° / 180°	360°	
Multi-layer	No	Yes, 32 scan planes (+10° - +30°)	
Multi-target	No	No	
Rotation frequency	N/A	10 Hz	
Angular resolution	>0.25-1°	1.33° vertical, 0.6 ° horizontal	
Max. range	30 m with 10% reflectivity	70 m	>2 km (10% reflectivity)
Accuracy	10 mm ± 35 mm	+2 cm at 10Hz (one sigma at 25 m)	
Hardware elements	sensor(s) + LMI (optional)	sensor + interface box + GPS + IMU	
Power supply	24 V DC 20W 1.8A+ (heating: 24 V DC 140W 6A)	9-32 V DC (1A, 12 W)	
Weight	9 kg	< 2 kg	

Test Area



- ❖ Scanning static aircraft (August 6, 2014)

Data Acquisition Trajectory



- ❖ GPSVan trajectory; surveyed Cessna aircraft marked

Scanning Aircraft on the Tarmac



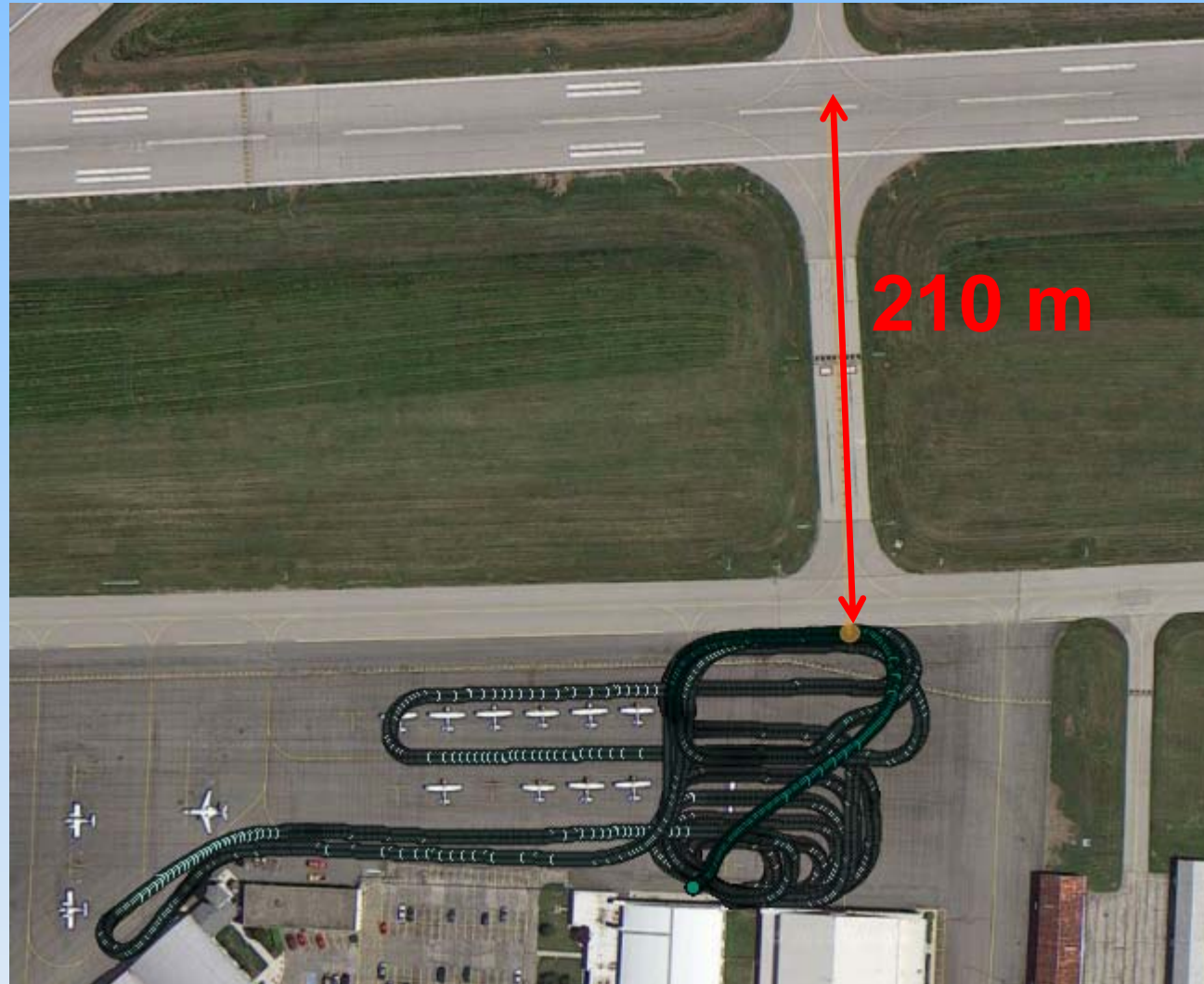
- ❖ Scanning static aircraft (August 8, 2014)

Scanning Aircraft on the Runway

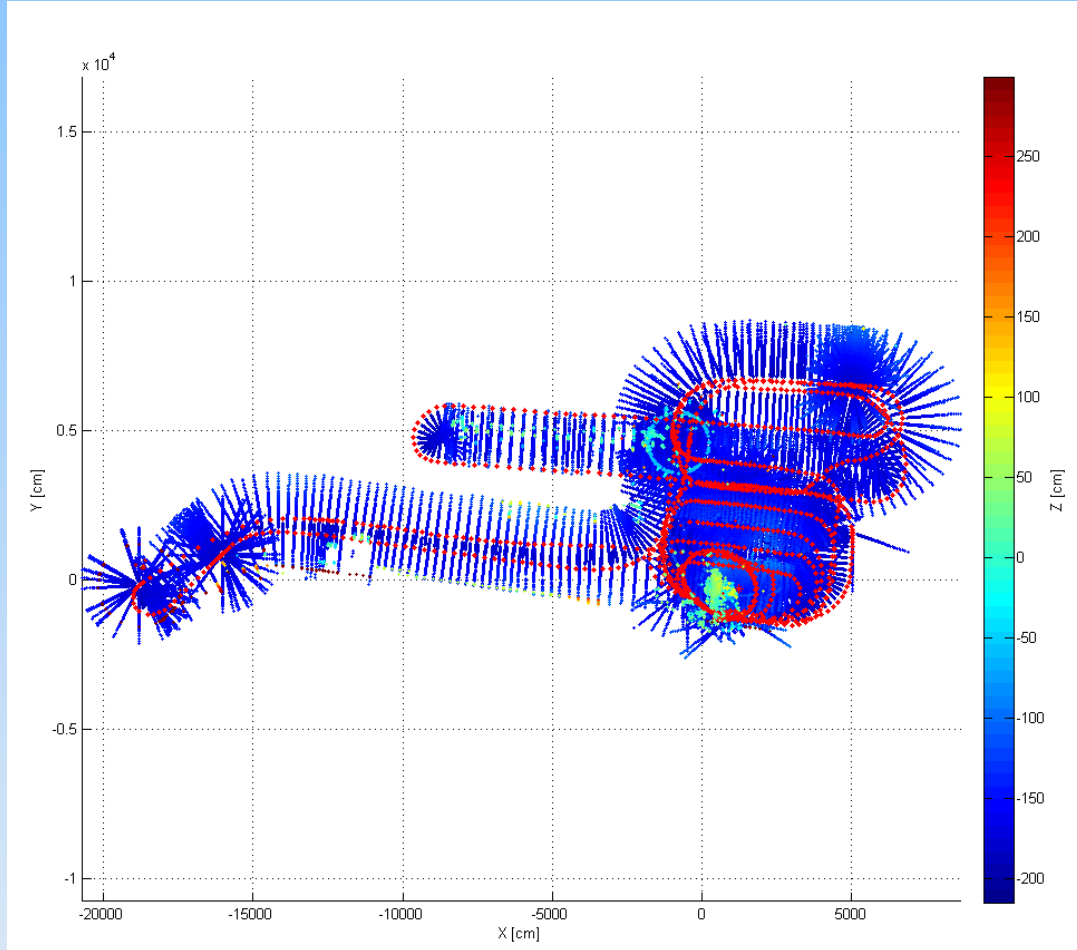
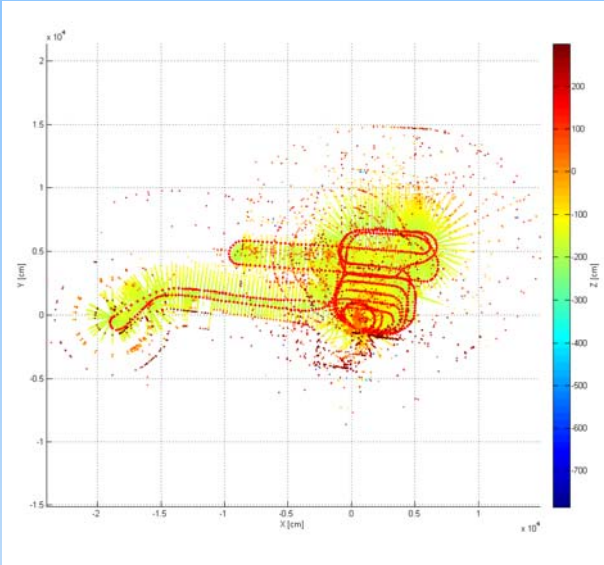


- ❖ Scanning moving aircraft

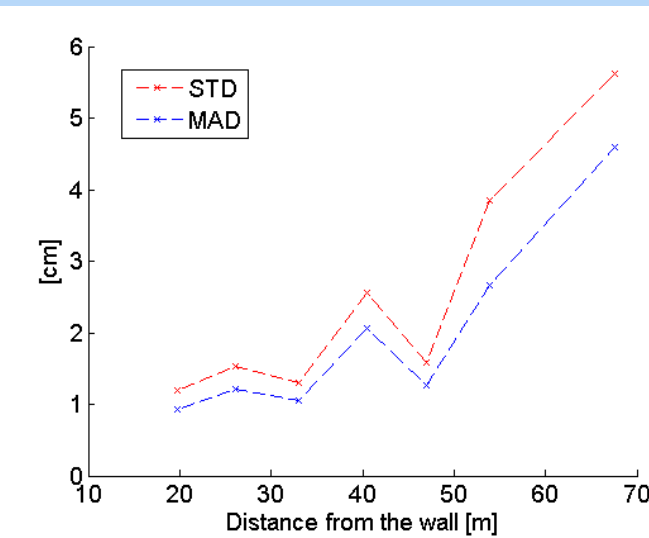
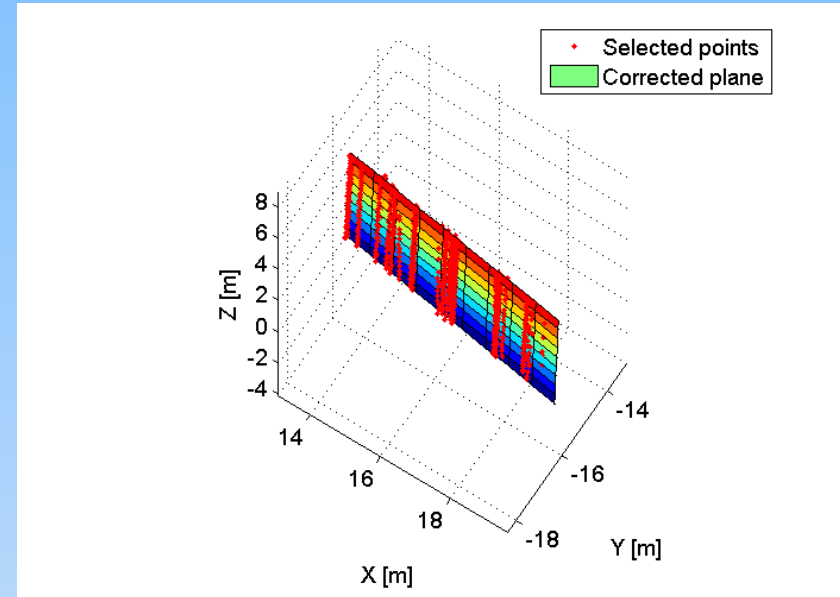
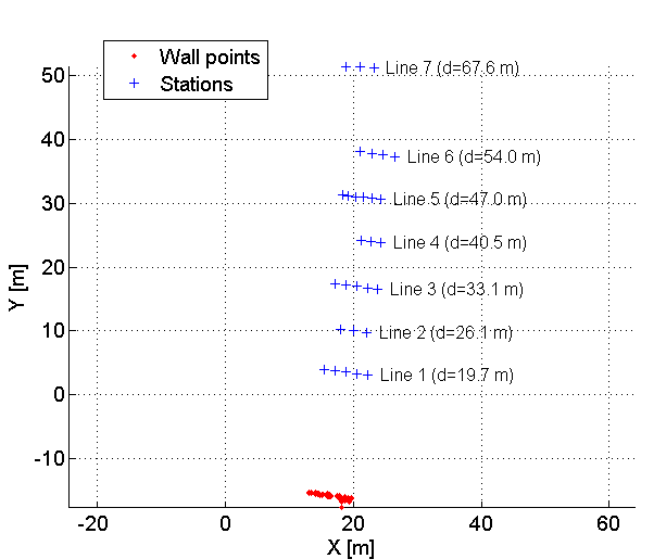
Distance from the runways



Profiles in a Global Frame



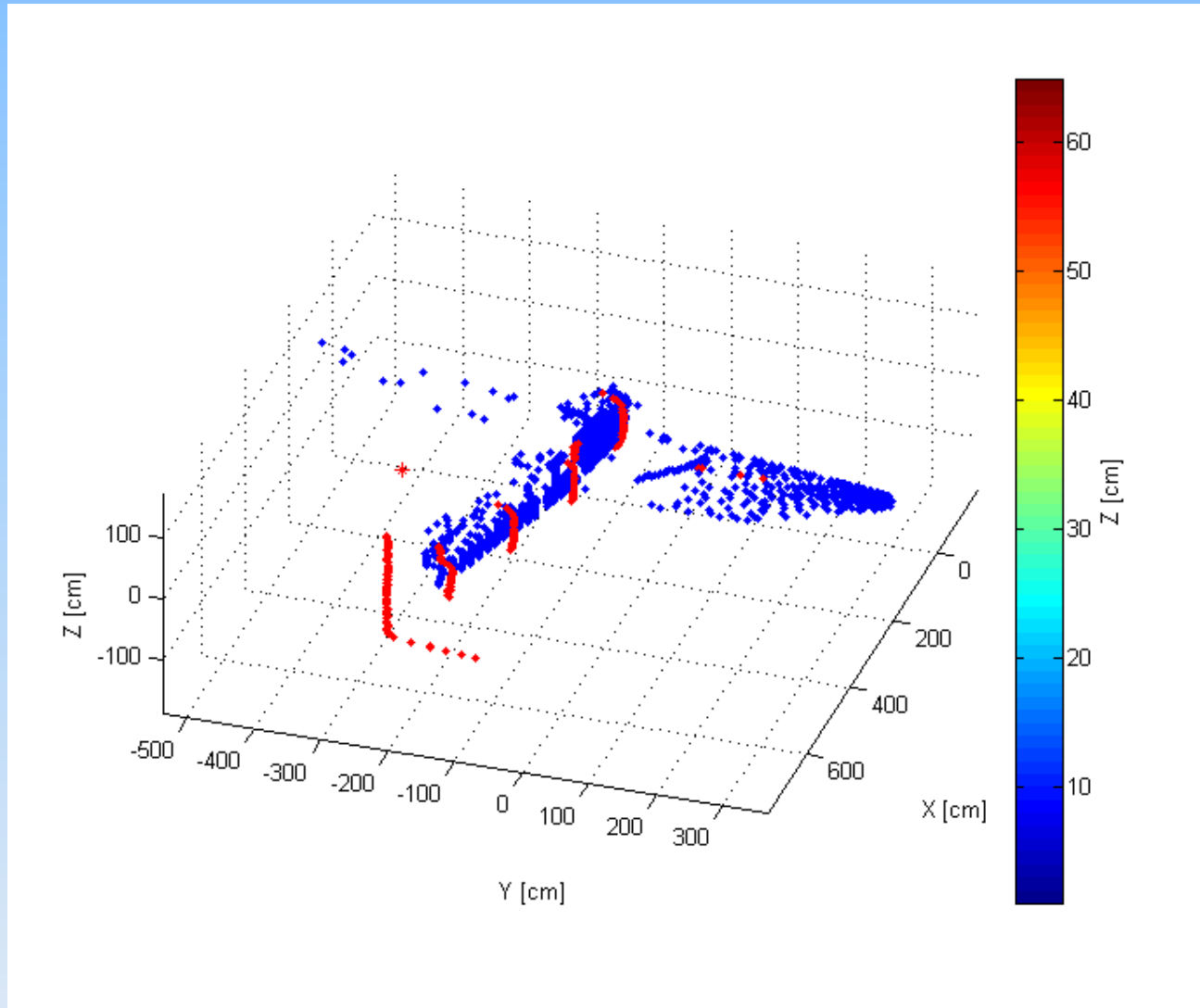
Accuracy Test



	Distance from wall [m]	Differences from the wall			
		AVG [cm]	STD [cm]	MED [cm]	MAD [cm]
Line 1	19.7	1.5	1.2	1.2	0.9
Line 2	26.1	1.8	1.5	1.4	1.2
Line 3	33.1	1.9	1.3	1.7	1.1
Line 4	40.5	3.6	2.6	3.1	2.1
Line 5	47.0	2.1	1.6	1.8	1.3
Line 6	54.0	10.8	3.9	10.4	2.7
Line 7	67.6	10.7	5.6	11.6	4.6

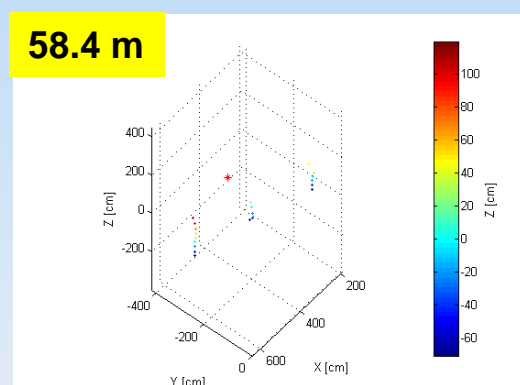
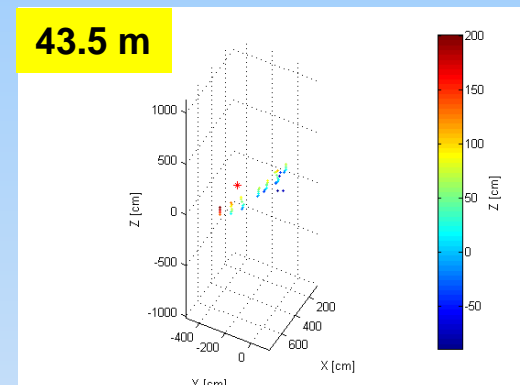
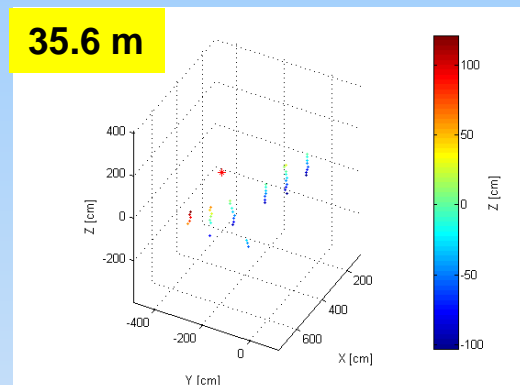
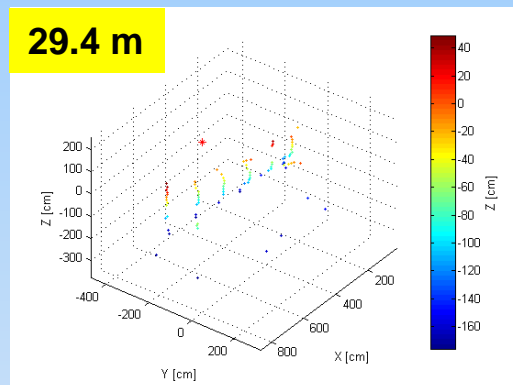
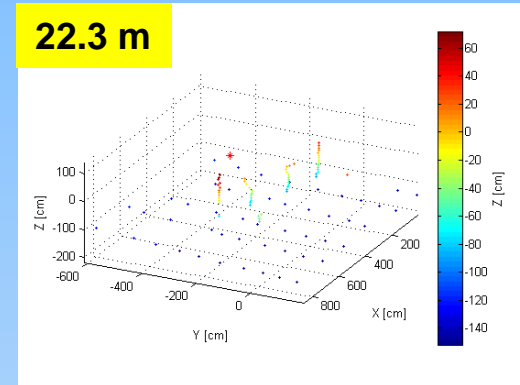
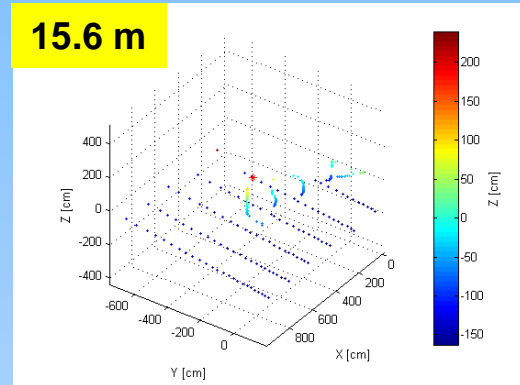
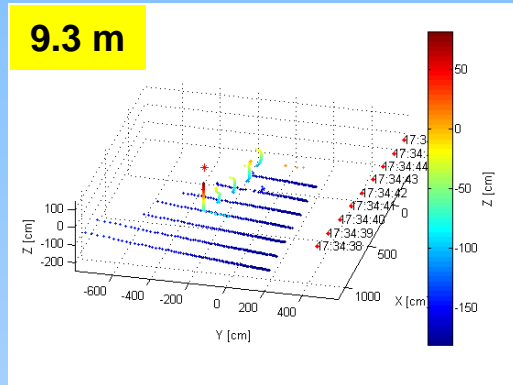
Manufacturer's specification: $< 1 \text{ cm} \pm 3.5 \text{ cm}$

Scanner vs Profiler Data

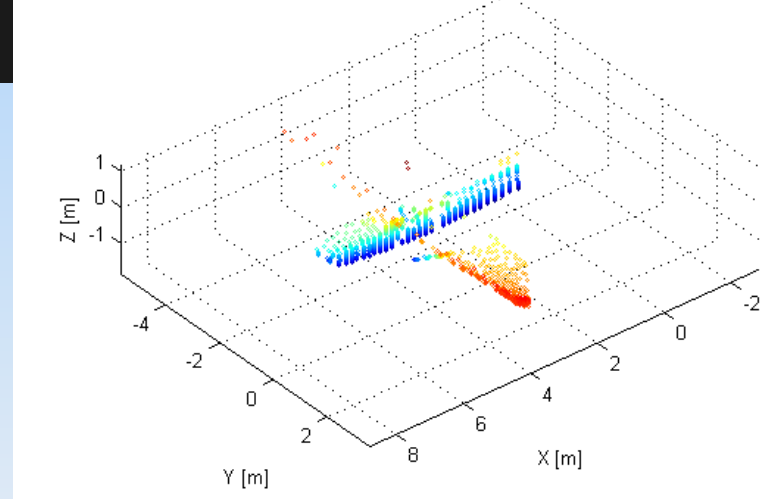
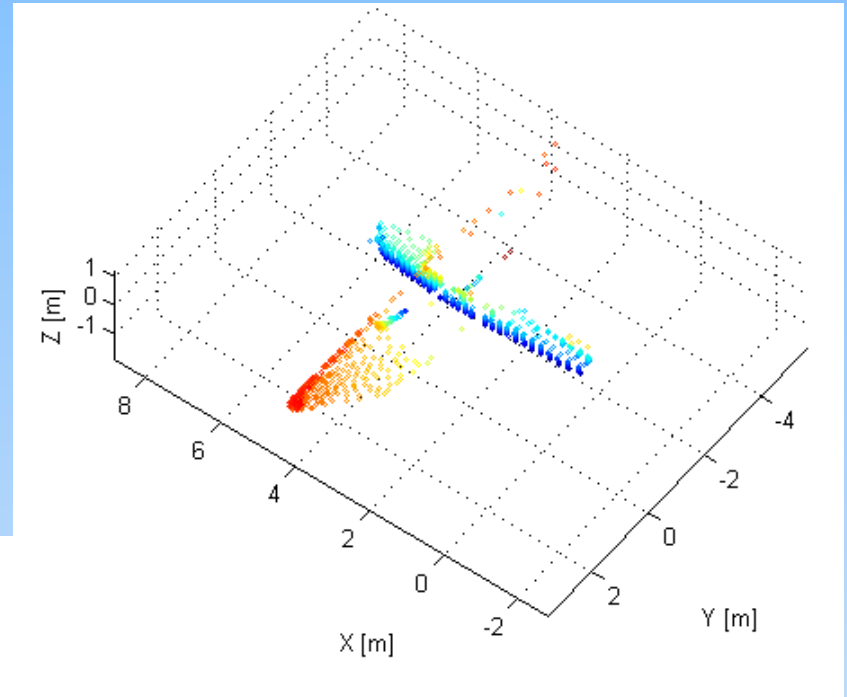
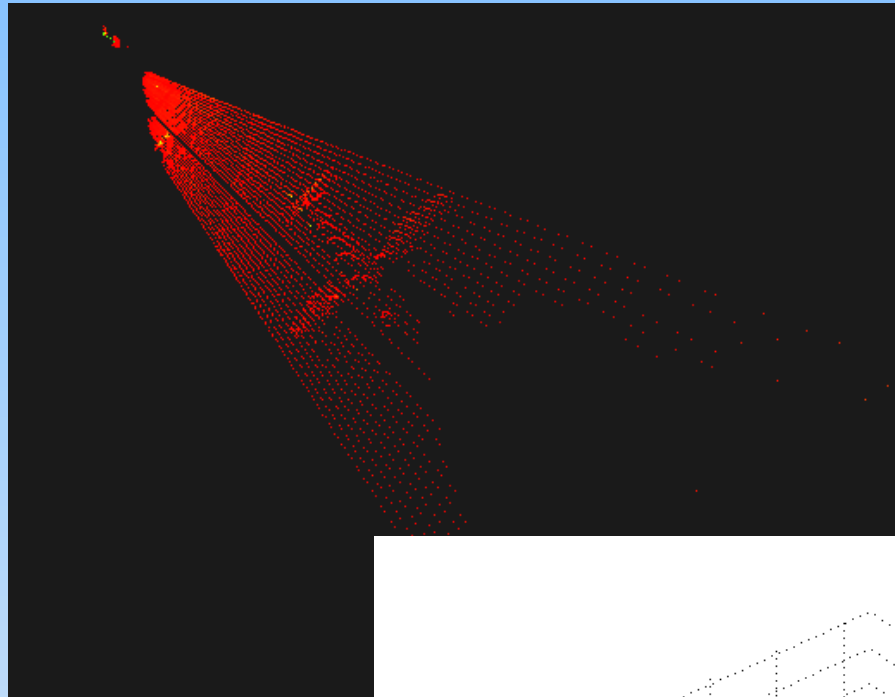




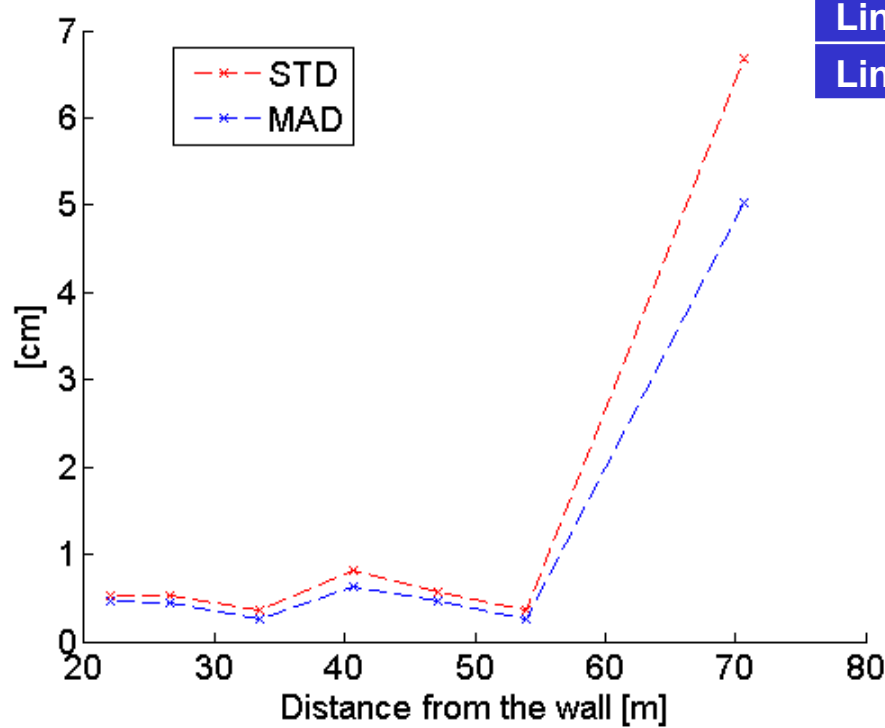
Profiles at Different Distances



Aircraft Scan



Accuracy Analysis: Velodyne HDL-32E



	Distance from wall [m]	Differences from the wall			
		AVG [cm]	STD [cm]	MED [cm]	MAD [cm]
Line 1	21.9	0.8	0.5	0.8	0.5
Line 2	26.6	0.6	0.5	0.3	0.4
Line 3	33.5	0.8	0.4	0.8	0.3
Line 4	40.6	1.0	0.8	0.8	0.6
Line 5	47.1	1.0	0.6	1.0	0.5
Line 6	53.9	0.6	0.4	0.6	0.3
Line 7	70.6	8.2	6.7	5.8	5.0

Manufacturer's specification:
 $< 2 \text{ cm} (< 25 \text{ m})$

8.3 Photogrammetrie, Fernerkundung, Geoinformation (PFG, ISSN 1432-8364)



Study on Sensor Level LiDAR Waveform Data Compression Using JPEG-2000 Standard Multi-Component Transform

GRZEGORZ JÓŻKÓW, CHARLES TOTH, Columbus, OH, USA, MIHAELA QUIRK, Washington D.C., USA & DOROTA GREJNER-BRZEZINSKA, Columbus, OH, USA

Keywords: LiDAR, full-waveform, compression, JPEG-2000 Standard, decorrelation, performance analysis

Summary: In contrast to LiDAR data provided by discrete return systems, full waveform LiDAR data (FWD) improve the quality of products and extend the possibilities of their application. Beside evident benefits, FWD imposes strong requirements on the sensor acquisition and storage hardware. At the moment, there is little effort reported on sensor level waveform data compression. Vendor specified waveform data formats are generally not published for the users and do not mention compression options. Since the recorded waveform is intrinsically noisy, there is less practical need to use lossless compression methods. As long as the properties of FWD are preserved, in other words, as long as it is possible to extract the same FWD features, and the compression noise is below or comparable to the noise of the signal, lossy compression methods are suitable. Such compression of FWD was studied in previous work where waveforms were compressed individually or in groups forming images, which is considered as 1D and 2D compression, respectively. This work presents a strategy for FWD compression that is based on multi-component transforms, which is included in JPEG-2000 Standard Part 2. This extension to JPEG-2000 Standard exploits the 3D correlation between waveform samples and allows compressing waveform cubes without organizing samples. The results of this study indicate that the removal of data redundancies in all three dimensions results in slightly better compression performance than using 1D or 2D approaches. More importantly, the user has the flexibility to decide on how much the data should be compressed or what level of the reconstruction error is allowed. Besides JPEG-2000 compression, this investigation includes experiments with additional data decorrelators, such as Karhunen-Loëve transform and wavelet transform. The conclusion of this study is that the JPEG-2000 Standard is an effective method for FWD compression of waveform cubes, resulting in high compression ratios and low data degradation.

Zusammenfassung: Untersuchung zur Kompression von Full Waveform LiDAR-Daten auf Sensor-Ebene unter Verwendung der JPEG-2000 Multikomponenten-Transformation. Im Gegensatz zu den üblichen Discrete Return Systemen können Full Waveform LiDAR-Daten (FWD) die Qualität der Produkte verbessern und erweitern somit ihre Anwendungsmöglichkeiten. Neben diesen offensichtlichen Vorteilen stellen FWD sehr hohe Anforderungen an den Sensoraufbau und die verfügbare Speicherkapazität. Bisher gibt es noch wenige Arbeiten zur Datenkompression der FWD-Daten auf Sensorebene. Herstellerspezifische Full Waveform Datenformate werden in aller Regel nicht dem Anwender zur Verfügung gestellt und erwähnen keine Möglichkeit der Datenkompression. Da die aufgezeichneten FWD ohnehin verrauscht sind, ist es nicht nötig, eine verlustfreie Kompression zu verwenden. Solange die Eigenschaften der FWD erhalten bleiben, das heißt, dieselben FWD-Merkmale extrahiert werden können und das Kompressionsrauschen unter oder vergleichbar dem Signalauschen ist, können auch verlustbehaftete Kompressionsmethoden genutzt werden. Diese Art der FWD-Kompression ist aus vorherigen Studien als 1D- oder 2D-Kompression bekannt, bei denen einzelne oder Gruppen von Wellenformen als Bilder interpretiert und komprimiert werden. In dieser Arbeit wird eine Strategie zur FWD-Kompression präsentiert, welche auf einer Multikomponenten-Transformation basiert und im JPEG-2000 Standard Teil 2 beschrieben ist. Diese ist eine Erweiterung zum JPEG-2000-Standard, die die 3D-Korrelation zwischen Waveform-Proben auswertet und damit die Kompression eines kompletten Waveform-Kubus ohne Proben als Startwerte erlaubt. Die Ergebnisse dieser Studie zeigen, dass das Entfernen von Redundanzen in allen drei Dimensionen zu einer geringfügig besseren Kompression als die ausschließliche Nutzung von 1D- oder 2D-Informationen führt. Zusätzlich eröffnet sich dem Nutzer jedoch die Möglichkeit zu entscheiden, wie

stark die Daten komprimiert werden sollen oder welcher maximale Fehler bei der Rekonstruktion zugelassen wird. Neben der JPEG-2000-Kompression beinhaltet unsere Untersuchung Experimente mit zusätzlicher Datendekorrelation wie der Karhunen-Loève-Transformation und der Wavelet-

Transformation. Das Ergebnis dieser Studie zeigt, dass der JPEG-2000-Standard eine effektive Methode für FWD-Kompression in Form eines Waveform-Kubus bietet. Daraus resultiert eine hohe Kompressionsrate bei nur geringem Qualitätsverlust der Daten.

1 Introduction

The hardware developments of laser scanning technology continuously provide new application possibilities, though, limitations and difficulties are frequently encountered in the introduction phase. Starting from 2004, when the full-waveform digitization became available for the commercial airborne scanning systems (HUG et al. 2004, MALLET & BRETER 2009), improvements of quality of LiDAR data and products have been observed. The main advantages of the full waveform data (FWD) are: (1) denser and more accurate point cloud generation (MALLET & BRETER 2009, PARTRISH & NOWAK 2009), (2) improved results in vegetation mapping, e.g. for forestry applications (PIROTTI 2011), and (3) better point cloud classification (REITBERGER et al. 2008, TOTH et al. 2010, HEINZEL & KOCH 2011, MALLET et al. 2011). Despite of the advantages of FWD, technology limitations are still present. For example, waveform data may not be recorded at maximum pulse rate designated for the discrete return systems; there is also a lack of vendor independent tools for waveform data processing; finally, the most common problem is the amount of FWD. Typically, FWD binary files, e.g. Riegl SDF, are 3–4 times larger than the binary files (LAS) containing corresponding point clouds. Although storage technologies continue to develop, allowing for faster read/write operation and accommodation of larger data volumes, the drawback of the increasing size of FWD continues to be an issue.

Most of the activities of LiDAR data compression are concerned with the reduction of the point cloud size to better support the dissemination of primary LiDAR products. The most widely used solutions in practice are the lossless LASzip (ISENBURG 2011), LASCompression (GEMMA LAB 2009, MONGUS & ŽALIK 2011) and the lossy/lossless LiDAR Compre-

sor (LIZARDTECH 2014). Other approaches are hardware accelerated compression (BIASIZZO & NOVAK 2013) or considering the point cloud thinning as lossy compression in topographic applications (PRADHAN et al. 2005). Although the need for FWD compression is indisputable, there is rather limited research related to sensor level waveform compression. Work on compressing each waveform separately (TOTH et al. 2010) and exploiting 2D correlation between waveform samples for more efficient compression is reported in JÓZKÓW et al. (2015). BUNTING et al. (2013) proposed the Sorted Pulse Data (SPD) format for storing LiDAR data, implemented in the open source software library SPDLIB (SPDLIB 2013). SPD follows the Hierarchical Data Format version 5.0 (HDF5) (KORANNE 2011, THE HDF GROUP 2014) which supports lossless compression using the zlib deflate algorithm (THE INTERNET ENGINEERING TASK FORCE (IETF) 1996). Since this compression does not exploit LiDAR data properties, e.g. spatial or temporal correlation, the compression ratio is likely to be limited. Due to the complexity of data stored in SPD, it is difficult to compare the compression ratios with those obtained using other methods. Though there are results reported on SPD file compression, they are based on limited experiments (BUNTING et al. 2013). Another proposed waveform exchange standard, Pulse-Waves (ISENBURG 2014) provides an option for file compression, but it is still in the development phase, so details are unknown at the moment. Additionally, waveform decomposition for a sum of components or echoes (CHAUVE et al. 2007, MALLET & BRETER 2009) also represents lossy FWD compression allowing for reconstruction/decompression. Obviously, the compression rate and data distortion strongly depend on the number of detected echoes. According to the authors' knowledge, there is no work published assessing the performance in

terms of ratio and reconstruction noise of the lossy compression represented by waveform decomposition parameters.

Since there is little need for lossless compression of FWD (Józków et al. 2015), this paper investigates a lossy compression approach which employs the extensions of JPEG-2000 Standard Part 2 of multi-component transform. This transform allows exploiting the correlation of waveform samples along three directions: waveform, scan line, flight line, and then compresses the entire waveform cube without the need of separating and compressing single waveforms or arranging them into groups, etc. In relation to 1D (Toth et al. 2010), and 2D (Józków et al. 2015) compression of FWD, the expected gain of the approach proposed here is a higher compression ratio, as the data redundancy may be better removed by considering full spatial (3D) correlation of the waveforms. Additionally, two other transforms for FWD decorrelation were tested to investigate whether the reported high performance of compression based on JPEG-2000 Standard could be further improved.

2 Waveform Data Arrangement

2.1 Waveform Cube

Full waveform data is not necessarily restricted to the digitized waveform, but is usually identified with waveform signal samples, the essential data for further processing. Additional data, such as time and pointers to flight navigation parameters are necessary to compute geolocation and, finally, to create the point cloud. The size of the mandatory metadata, however, is much smaller than the size of waveform samples, which implies that the compression is mainly considered for waveform samples. Besides the vendor specified formats for waveform data storage, which are usually unknown, there are independent standards allowing the waveform data exchange, such as the LAS format (ASPRS 2013); note that only point data record formats starting from LAS v1.3 are able to store FWD, and the PulseWaves tool (ISENBURG 2014) or SPDLIB (SPDLIB 2013) have this capacity, too. The strategy used in the approach proposed here

for waveforms compression is based on a 3D waveform data structure, called a waveform cube (Józków et al. 2015), due to its similarity to the image cube of hyper-spectral images. A very similar idea of representing waveforms in a volumetric data structure, but for static terrestrial scanning, was presented earlier by STILLA & JUTZI (2008). The waveform cube is not a standard or a file format, but the structure of FWD arrangement that maintains the topology of waveform samples according to the data acquisition process (Fig. 1). The three dimensions of the waveform cube are: flight direction of the aircraft, scan line (cross flight direction), and the direction of the laser pulse propagation (waveform). It must be emphasized that the waveform cube is not a georeferenced structure, such as an orthophoto or a digital terrain model (DTM) grid, i.e. the distance in the 3D space between any two elements of the cube cannot be calculated based in the cube indices; however, the topology of waveform samples is always related to the spatial order of the laser pulses, i.e. the sequence, as they are acquired in time.

While the formation of the waveform cube is simple, there are a few additional aspects that should be mentioned. First, the outgoing pulse is also digitized as part of the waveform record, since this information is essential for waveform decomposition. There are two ways to compress the outgoing waveform: either jointly with the return waveform or independently, by forming another waveform

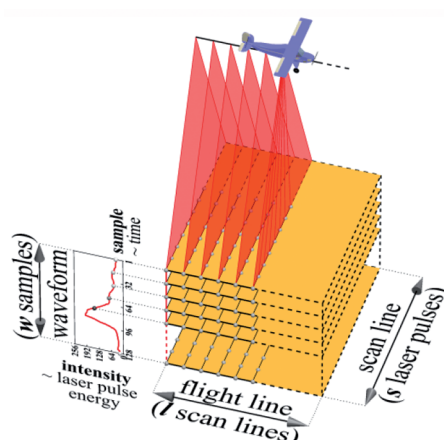


Fig. 1: Waveform cube structure

cube. Since the size of the outgoing waveform is fixed, the second option is preferred. Similarly, for multi-wavelength LiDAR systems, waveform cubes can be formed for each sensor; note the correlation among the different wavelength waveform could be potentially exploited for compression in the future. The second aspect is the object space complexity, which has a paramount effect on the spatial correlation of the waveforms. Neighbouring waveforms are generally similar to each other over open and slowly changing areas, whereas in built-up areas, such as urban canyons, their

shape can change abruptly, resulting in a less efficient compression.

The third aspect is the waveform cube size which is defined in two directions by the waveform record length and the number of pulses per scan line. Both may fluctuate on some systems, in which case, empty waveform samples or records can be inserted, respectively. The third dimension, however, can be set arbitrarily, ranging from a few scan lines to all the scan lines in a strip. Given the spatial extent and the computational aspects, a nearly equal size in the horizontal dimensions is preferred,

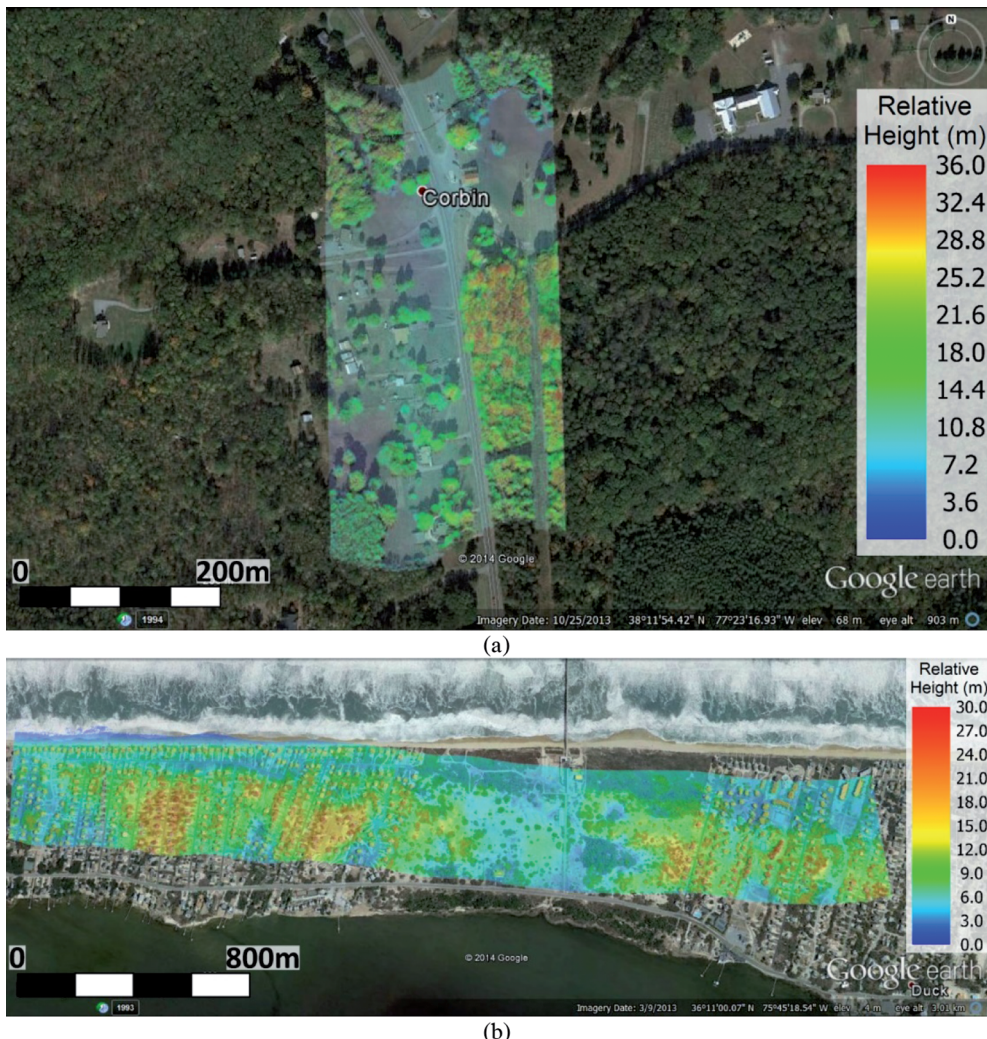


Fig. 2: Test waveform cube location: (a) Area covered by both the C1 and C2 cubes, Corbin, Virginia, USA, (b) C3 cube, Duck, North Carolina, USA.

which is similar to the standard practice of tiling large geospatial data. Note that some sensors use multiple waveform digitizers, requiring the use of multiple cubes.

In summary, the idea of the waveform cube is not ideal in terms of implementation, as it may not be directly applicable to all scanners; for example, waveform sample rearrangement may be needed. Yet in a statistical sense, the waveform cube provides an effective way to achieve high compression performance due to its ability to exploit 3D correlation.

2.2 Test Data

The data variability greatly affects compression performance manifested by the value of the compression ratio; usually data with a low variation can be compressed with higher ratio than more varying data. Consequently, test data for the assessment of compression performance should be chosen carefully, avoiding the extreme conditions of high and low data complexity. The test site, shown in Fig. 2a, contains a mixture of topographic elements, such as buildings, road infrastructure, dense forest, single trees, and open terrain. To support this study, two waveform cubes were extracted and used in extensive tests, covering nearly the same area and acquired by using two different LiDAR systems (Riegl Q680i and Riegl Q780) on the same flight. This explains a slightly different size of both test waveform cubes of $504 \times 1200 \times 120$ and $488 \times 1170 \times 120$ scan lines, waveforms per scan line, and samples in the waveform (l, s, w dimensions in Fig. 1), for the first (C1) and the second (C2) cube, respectively. Additionally, a 3 km single strip, C3 (Fig. 2b), acquired using a Riegl Q780 scanner, was processed, allowing to test the algorithm in diverse conditions, in terms of topographical objects. Tests for C3 data included both emitted and returned waveform cubes; the numbers of waveform samples were 28 and 120, respectively. The strip was divided into 12 cubes, each containing 496 scan lines, and the number of pulses was 1170 per scan line.

For all datasets, the signal intensity was sampled at 1 ns with 8 bit resolution. Thus, the waveform consisting of 120 samples represent

a vertical range of 36 m, clearly sufficient to include all the natural and man-made objects in these areas.

3 Compression Strategy

Similarly to our previous work, only lossy compression methods were considered because a perfect reconstruction of recorded FWD is practically not necessary, as discussed in details by Józków et al. (2015). Based on those results, it was concluded that JPEG-2000 Standard was the most efficient among the tested 2D strategies of waveform data compression. Here the objective is to extend the compression from 2D to 3D, so the goal of this study is to benefit waveform data compression by exploiting the correlation of waveform samples in each of three dimensions: along flight line, scan line, and waveform direction. Extensions of the JPEG-2000 Part 2 (TAUBMAN & MARCELLIN 2002) introduce a multi-component transform resulting in the ability to compress multi-band images. In short, the simplest multi-component transform first applies a decorrelating transform, e.g. 1D wavelet transform, to each pixel of the image in the third dimension, and then each image component, e.g. band, follows the JPEG-2000 Part 1 compression schema. Due to the Part 2 extension, previous JPEG-2000 restrictions of compression only single band or three band images, as RGB, were removed and the possibility of applying JPEG-2000 compression to hyper-spectral images consisting of multiple bands became available (KULKARNI et al. 2006). Since the structure of hyper-spectral images and waveform cubes are identical, both data types can be compressed using the same strategies. The extension of the JPEG-2000 Part 2 containing multi-component transform is implemented only in a few specialized software packages, such as the PICTools Medical SDK for compressing volumetric medical scans (ACCUSOFT 2014), LEADTOOLS JPEG 2000 Image Compression SDK (LEADTOOLS 2014), OpenJPEG library (OPENJPEG 2014), and Kakadu Software (KAKADU SOFTWARE 2013) which, in version 7.2, was used in this study. In order to investigate the variability of the waveform

cube affecting compression, additional operations were also performed prior to Kakadu compression. The flowchart of all performed operations is presented in Fig. 3 and discussed below in details.

Since the actual range of waveform sample intensities (values) varies for each band of the waveform cube and, thus, may adversely affect the decorrelating transforms, waveform cube bands were normalized before applying these transforms. In this study, three variants of the band-wise normalization were tested:

- zero-mean (ZM), where the mean value of the band was subtracted from the waveform samples for each band,
- unit-variance (UV), where beside the mean removal, sample normalization was applied so that each band had unit variance,
- no normalization, i.e. using the original cube data (OC) for comparison purposes.
- JPEG-2000 contains the full lossy compression scheme, including (1) the transform engine for data decorrelation, (2) the quantization engine for data loss/reduction, and (3) the bit encoding engine for lossless compression. Nevertheless, the influence of using data decorrelations prior to JPEG-2000 is of interest since better decorrelation usually results in a better compression rate. Therefore, as a preprocessing step, three different decorrelation methods were tested:

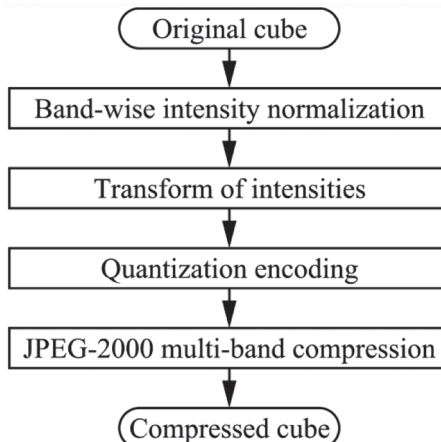


Fig. 3: Flowchart of operations executed during experiments.

- Karhunen-Loëve transform (KLT) (KARHUNEN 1947, QUIRK 2003),
- wavelet transform (WLT) using Cohen-Daubechies-Feauveau 5/3 wavelet (CDF 5/3) (COHEN et al. 1992),
- no transform (NOT) for comparison purposes.

KLT was applied to the cube regarded as a discrete vector stochastic process (QUIRK 2003). This means that the whole waveform cube should be considered as a single large image which is the result of ‘gluing’ together slices of the cube along the waveform-scan line plane. Considering dimensions of the cube as l , s , and w according to Fig. 1, the single large image B will have the size of w , and $l \cdot s$ (shown on the right side in Fig. 4) and then KL-transform is calculated as:

$$C = K^T \cdot B \quad (1)$$

where:

$$K = \begin{bmatrix} k_{1,1} & k_{1,2} & \dots & k_{1,w} \\ k_{2,1} & k_{2,2} & \dots & k_{2,w} \\ \vdots & \vdots & \ddots & \vdots \\ k_{w,1} & k_{w,2} & \dots & k_{w,w} \end{bmatrix}$$

is the KLT matrix whose columns are the eigenvectors of the covariance matrix of image B . Note that covariance of the image can be calculated two ways, depending on whether columns or rows of the image are treated as random variables. In this work, the first method was applied. C is the KL-transformed single large image which is reshaped backward into the cube, and then subjected to the subsequent operations. The key of such use of KLT is the data decorrelation, resulting in packing the energy of the signal mostly in the first few bands (QUIRK 2003, VAIDYANATHAN 1998). This could benefit the JPEG-2000 multi-band compression, where many compressed bands may contain almost no energy. KLT is reversible, which means the original image B can be reconstructed based on the transformed data C and the transformation matrix K :

$$B = K \cdot C \quad (2)$$

The inverse KLT was applied for the reconstruction (decompression) process, which in-

cludes data reshaping between waveform cube and single large image, but in the reverse order as in the compression process.

In the second test, 1D WLT was applied to each waveform separately (Fig. 4). The results of WLT are low- and high-frequency components, denoted here as Lo and Hi . Considering 1D WLT as applied in this work, both Lo and Hi components have the same length, equal to half of the length of the original signal (waveform). Note that the low-frequency component contains most of the original signal energy, thus considering such transform for all waveforms, the energy would be packed into one half of the cube bands. Similarly, the Lo component can be subjected to another WLT resulting in two new components having half of the length of the parent, so the original sig-

nal content will be included only in one quarter of the cube. This sequential WLT known as multi-resolution analysis (MRA) (MALLAT 1989) will finally result in packing the energy of the signal in the first few bands, similar to KLT (see the length of Lo component in Fig. 4). The number, n , of possible levels of MRA depends on the length of the original signal. n is less than $\log_2(m)$, where m is the length of the signal; for example, for a waveform length of 120, used in this study, the maximum MRA is 7 levels; however, only three levels were used here to avoid edge effects and length extension of the WLT components. Similarly to KLT, WLT is totally reversible.

From the perspective of compression of an 8 bit waveform cube, data normalization and transforms contradict to the idea of data re-

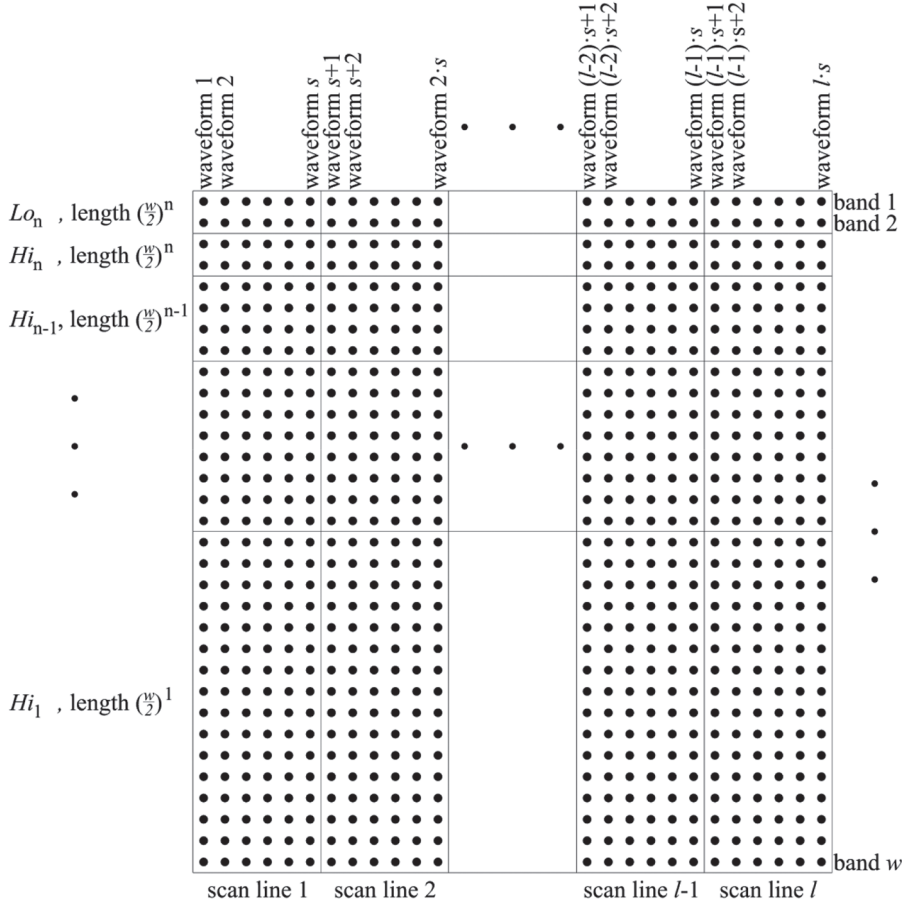


Fig. 4: Wavelet transform applied on the large image of the whole waveform cube.

duction since these operations result in a larger data size due to a conversion from integers into real numbers, usually in 32 bit or 64 bit representation. Additionally, some of the compressing tools do not allow floating point numbers as input pixel (sample) values. For example, the Kakadu Software accepts only 32 bit input. Therefore, the quantization encoding is needed to allow mapping floating point numbers into integers. Note that this process is invertible, known as quantization decoding, but provides no perfect reconstruction. The experiments on the test data showed that an 8 bit range would be too short to avoid large quantization errors, and, thus, more bits for the quantization base are needed. In this experiment, a linear quantizer with a 28 bit base length was used providing much larger dynamic range than that of the original data (8 bits). The amount of the introduced quantization noise and other data distortion, such as numerical errors of data normalization and transforms not caused by JPEG-2000 compression, was empirically evaluated. First, the test waveform cubes were subjected to forward processing, including data normalization, transform, and quantization encoding; and then, the inverse operation, i.e. quantization decoding, inverse transform, and reverse data normalization, was carried out. The observed maximal absolute difference between the value of the original and reconstructed waveform sample was on the level of $1e-4$ that equals to 0 in integer terms.

The results of the investigation of image based waveform cube compression (Józków et al. 2015) showed that the best compression performance was obtained for the set of images where the single image was formed by all waveforms of a single scan line (according to s and w dimensions in Fig. 1). Therefore, the waveform cube was rotated prior to multi-band compression in the Kakadu Software, thus the dimension l of the cube was treated as the band during JPEG-2000 multi-component transform.

In the case of lossy compression, the user can decide partially about the amount of data degradation and compression ratio. Depending on the implementation, a quality factor is used to control the desired compression ratio. In the Kakadu Software, this user input pa-

rameter is the bits per pixel ratio, i.e. the average number of bits for a single pixel in the compressed file. Obviously, this value must be smaller than the bit depth in the original image in order to gain a reduction in the file size, but a smaller ratio means a larger data distortion due to compression. The resulting ratio might be slightly different from the value given by the user because the compression strength depends also on the inherent parameters of the data. Since the original waveform data is 8 bits, experiments were executed for 20 parameters, ranging from 0.4 to 8 bits with a step size of 0.4 bits. Note that Kakadu compressed JPEG-2000 file might include several reconstruction qualities, in other words, one file may contain data compressed with different ratios at the same time, but this option was not tested during this investigation.

4 Performance of Waveform Data Compression

Compression performance might be evaluated from different perspectives, such as the achieved compression ratio and reconstruction error. The compression ratio is defined by the percentage of the compressed file size with respect to the original one. In the case of image compression, the bits per pixel ratio (BPP) or the bits per pixel per band ratio (BPPP) are frequently used to describe the compression ratio, depending whether a single- or a multi-band image is compressed. The BPP value is the number of bits used to store a single pixel in the compressed image. Due to the similarity of multi-band images and waveform cubes, the BPPP was used in this study. Note that a pixel of the image cube is equivalent to a waveform sample in the waveform cube. Knowing the BPPP ratio for the original and compressed cubes, the compression ratio or percentage ratio can be easily calculated. The compression ratio is also affected by the file header, or metadata, essential for decompression. This data is kept in the compressed file, increasing its size. The final BPPP ratio was calculated on the basis of the file size produced by the Kakadu Software and the number of waveform samples in the waveform cube. Note that the size of oth-

er data, mandatory for reconstruction, such as mean values of bands in the case of ZM data or K matrix in the case of KLT transform and quantization parameters, were not included in this calculation. The omission of these parameters in the size calculations does not change the BPPP ratio significantly, because the size of these parameters is much smaller than the size of the compressed cube.

The performance of lossy compression methods is related to the data degradation, the distortion (noise) introduced due to quantization included in the compression process. Reconstruction noise (error) can be measured by different parameters, such as signal to noise ratio (SNR), peak signal to noise ratio (PSNR) (VAIDYANATHAN 1993), or just by giving simple statistics of the differences between reconstructed and original data. In this work data distortion was measured by the SNR, which is based on the variance of waveform samples and their differences:

$$SNR = 10 \cdot \log_{10} \frac{\sigma_o^2}{\sigma_{o-r}^2} \quad (3)$$

where

σ_o^2 – variance of all the original waveform samples,

σ_{o-r}^2 – variance of waveform sample differences between original and compressed data.

For a low data degradation, the SNR is large, and it approaches infinity for a perfect reconstruction. Note that the calculated SNR describes only quantization noise of the original waveform signal.

Another aspect of compression performance is the computational cost, the compression and decompression speed and use of computer resources. In our previous work (Józków et al. 2015), it was concluded that 2D JPEG-2000 based compression is fast enough to support waveform compression during the acquisition process in the sensor system, as waveforms forming single scan lines might be compressed progressively. Similarly, waveform cubes might be compressed progressively by the approach presented in this work. However, the additional transforms for data decorrelation introduced in this experiment, e.g. KLT, make the algorithm much more complex and,

consequently, resulting in a much slower execution than the 2D compression. Obviously, any computation on larger datasets like waveform cubes requires much more memory resources than computation performed on a small part of this data like the single image slice. These issues were not considered in this work in evaluating the computational expenses of the compression performance.

Finally, the impact of compression noise can be evaluated looking at the results of subsequent waveform data post processing tasks, but executed on the decompressed data. For example, the Gaussian waveform decomposition should result in the same number of detected echoes with insignificantly different parameters from those obtained in processing the original uncompressed FWD. Note that even well-established waveform decomposition methods produce varying results, just as the number of parameters used to describe the components can be different, for example, 3 and 4 (CHAUVE et al. 2007), or even 5 (LAKY et al. 2010). Based on the earlier investigation (Józków et al. 2015), it was concluded that the SNR of above 30 dB – 35 dB in typical airborne LiDAR data assures an acceptable waveform reconstruction error which will not cause significant changes in waveform shape and, consequently, does not affect the results of subsequent FWD processing, in particular waveform decomposition.

5 Results and Discussion

Numerical experiments were performed with all combinations of the three decorrelation techniques (OC, ZM, UV) and three transforms (NOT, KLT, WLT) at 20 different user specified compression ratios for two test waveform cubes C1 and C2. To discuss and analyze the effects, experimental results are visualized by showing the SNR as a function of the obtained BPPP in Fig. 5. For comparison purposes, results obtained for the same data but using the earlier proposed approach, based on JPEG-2000 compression of waveforms arranged in the set of 2D images (Józków et al. 2015) was added to the figures. It should be also explained why 2D compression did not result in large SNR or BPPP ra-

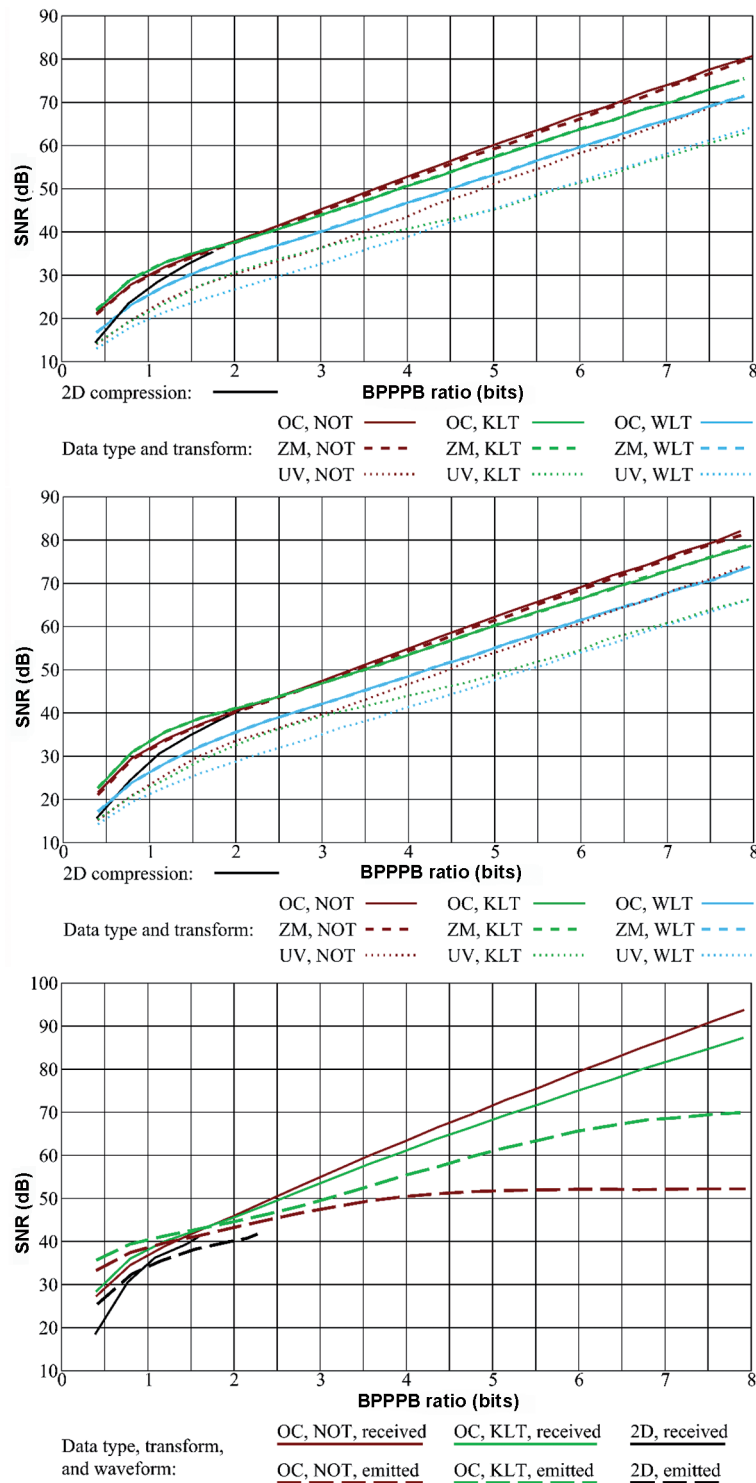


Fig. 5: SNR as a function of BPPPБ ratio, BPPPБ = bits per pixel per band ratio.

tio. For the user input ratios 2.4 bits and larger, the obtained SNR was always similar, about 35 dB and 41 dB for C1 and C2, respectively, as well as similar was the BPPP ratio, about 1.7 and 2 bits for C1 and C2, respectively. This explains the higher dynamic of JPEG-2000 based 3D compression than 2D compression of the waveform cube.

Comparing results obtained for C1 and C2 test cubes, it is clearly seen that the impact of using different sensors for collecting FWD for the same area is insignificant; a slightly larger (maximally 5 dB) SNR was obtained for the test cube C2. The most likely reason is the lower internal complexity of cube C2, as the compression of images containing less details results in lower reconstruction noise for the same compression rate. Among the used transforms, the worst SNR was obtained for WLT. This could be explained with the fact that *Lo* and *Hi* components are usually in very different ranges and, thus, a non-linear quantizer might be more appropriate for preserving better dynamic range of the quantized component values prior to JPEG-2000 compression. Differences between the other two transforms, KLT and NOT, are maximally of about 5 dB for the same BPPP ratio, where higher SNR was obtained for KLT in the case of small ratios and NOT in the case of large ratios. Considering that the used KLT is adaptive (needs to be calculated for every dataset), and therefore highly computational expensive, and the improvement of the SNR by a few dB only for small BPPP ratios compared to the case of using no transform (NOT), it is clearly not beneficial in practice. Obviously, a fixed KLT matrix for similar datasets might be used to reduce the number of computations, but it is extremely difficult to find representative datasets of FWD to create a fixed KLT base (Józków et al. 2015). The last aspect of the investigated approach is the data normalization method. The worst SNR was obtained for UV. Differences between OC and ZM are insignificant, which implies that data do not require any normalization and the intensities of the original waveform samples are suitable for the compression.

Based on the C1 and C2 results, compression experiments with the C3 dataset were executed only for the best performing data nor-

malization (OC) and transforms (NOT, KLT), resulting in similar performance for compressing received waveforms. SNR obtained for C3, however, was about 10 dB larger than for the C1 and C2 cubes. This may be explained by the simpler object complexity of the C3 area. Similarly, a difference of performance between compressing cubes of emitted and received waveforms was observed, as a large number of zero samples in the received cube resulted in higher SNR for large compression ratios. In contrast, the strong similarity of the emitted waveforms allowed for higher SNR for small compression ratios. This close similarity of the outgoing waveforms was also exploited by applying an additional decorrelating transform. For example, KLT applied to the emitted cube resulted in higher SNR, especially for large compression ratios, than in the case where the preprocessing transform was not applied (NOT). Since the outgoing waveforms change very little, instead of using adaptive KLT, a fixed KLT may be applied to reduce the computational expenses. Finally, comparing results of 2D with 3D compression approaches, the same observations can be noted as for the smaller cubes C1 and C2. Compression performance differences for emitted and received cubes in the 2D approach follow the same pattern as for 3D approach.

Comparing waveform compression results of the earlier 2D and here proposed 3D methods, both based on the JPEG-2000 Standard, the difference is not significant; for example, for unnormalized and untransformed data, the 3D approach for small BPPP ratio gives a slightly larger SNR than the 2D approach, the difference being about 5 dB – 10 dB. Clearly, the flexibility of the 3D approach to adjust the data degradation and compression ratio is an obvious advantage.

6 Conclusions

This work investigated the feasibility of compressing waveform cube using multi-component JPEG-2000 extension. The tested approaches included additional computations, such as data normalization and transforms prior to JPEG-2000 compression.

Based on the numerical experiments performed on three waveform cubes, it was concluded that in relation to 2D JPEG-2000 based compression, the multi-component extension is more flexible, because the user can chose between a larger range of compression ratios and select larger file sizes to obtain very low data loss, which was not possible for the 2D approach. For larger compression ratios (small BPPP ratio), however, both 2D and 3D approaches result in similar performance in terms of data degradation and reduction of the file size. Note that for both approaches, this similar performance was obtained for the same cube orientation where bands (images) were formed from waveforms representing single scan lines, offering more flexibility for the practical use where the same compression tool might be used with two different variants depending on the available computational power. More importantly, both single images and waveform cubes can be then progressively compressed according to the waveform data acquisition order. The advantage of 2D approach is speed, but the disadvantage is the low dynamic range and the inability to achieve a large SNR. Multi-component compression is slower, but gives the user more choices on deciding about the amount of data degradation.

The used implementation of the JPEG-2000 Standard with wavelet-based multi-component transform performed well in decorrelating the original waveform cube data. Additional data normalization or transform of the original waveform cube did not show significant improvements in 3D compression performance, and only caused extra computational costs.

Finally, one more advantage of using JPEG-2000 Standard for compressing waveforms in both approaches is the possibility of keeping different reconstruction levels in one, but larger file. It can be useful for data distribution with different distortion and compression levels depending on the application requirements.

References

- ACCUSSOFT, 2014: PICTools Medical SDK. – <http://www.accusoft.com/picmedx.htm> (31.10.2014).
- ASPRS, 2013: LAS specification, version 1.4 – R13. – http://www.asprs.org/a/society/committees/standards/LAS_1_4_r13.pdf (12.6.2014).
- BIASIZZO, A. & NOVAK, F., 2013: Hardware Accelerated Compression of LIDAR Data Using FPGA Devices. – *Sensors* **13** (5): 6405–6422.
- BUNTING, P., ARMSTON, J., LUCAS, R.M. & CLEWLEY, D., 2013: Sorted Pulse Data (SPD) Library. Part I: A generic file format for LiDAR data from pulsed laser systems in terrestrial environments. – *Computers & Geosciences* **56**: 197–206.
- CHAUVE, A., MALLET, C., BRETAR, F., DURRIEUF, S., PIERROT-DSEILLIGNY, M. & PUECH, W., 2007: Processing full-waveform lidar data: Modelling raw signals. – *International Archives of Photogrammetry, Remote Sensing and Spatial Information Sciences* **36** (Part 3/W52): 102–107.
- COHEN, A., DAUBECHIES, I. & FEAUVEAU, J.-C., 1992: Biorthogonal bases of compactly supported wavelets. – *Communications on Pure and Applied Mathematics* **45** (5): 485–560.
- GEMMA LAB, 2009: LASCompression. – <http://gemma.uni-mb.si/lascompression> (12.6.2014).
- HUG, C., ULLRICH, A. & GRIMM, A., 2004: Litemapper-5600-a waveform-digitizing LiDAR terrain and vegetation mapping system. – *International Archives of Photogrammetry, Remote Sensing and Spatial Information Sciences* **36** (Part 8/W2): 24–29.
- HEINZEL, J. & KOCH, B., 2011: Exploring full-waveform LiDAR parameters for tree species classification. – *International Journal of Applied Earth Observation and Geoinformation* **13** (1): 152–160.
- ISENBURG, M., 2011: LASzip: lossless compression of LiDAR data. – <http://www.cs.unc.edu/~isenburg/lastools/download/laszip.pdf> (12.6.2014).
- ISENBURG, M., 2014: PulseWaves. – <https://github.com/PulseWaves> (12.6.2014).
- JÓZKÓW, G., TOTH, C., QUIRK, M. & GREJNER-BRZEZINSKA, D., 2015: Compression Strategies for LiDAR Waveform Cube. – *ISPRS Journal of Photogrammetry and Remote Sensing*, **99** (1): 1–13.
- KAKADU SOFTWARE, 2013: Kakadu Software – Home. – <http://www.kakadusoftware.com> (12.6.2014).
- KARHUNEN, K., 1947: Über lineare Methoden in der Wahrscheinlichkeitsrechnung. – *Annales Academiae scientiarum Fenniae: Mathematica – Physica* **37**: 1–79, Universität Helsinki, Finnland.
- KULKARNI, P., BILGIN, A., MARCELLIN, M.W., DAGHER, J.C., KASNER, J.H., FLOHR, T.J. & ROUNTREE, J.C., 2006: Compression of earth science data with JPEG2000. – MOTTA, G., RIZZO, F. &

- STORER, J.A. (eds.): Hyperspectral Data Compression. – Springer: 347–378.
- KORANNE, S., 2011: Hierarchical data format 5: HDF5. – Handbook of Open Source Tools: 191–200, Springer.
- LAKY, S., ZALETNYIK, P. & TOTH, C., 2010: Land classification of wavelet-compressed full-waveform LiDAR data. – International Archives of Photogrammetry, Remote Sensing and Spatial Information Sciences **38** (Part 3A): 115–119.
- LEADTOOLS, 2014: LEADTOOLS JPEG 2000 Image Compression SDK. – <https://www.leadtools.com/sdk/compression/jpeg2000.htm> (31.10.2014).
- LIZARDTECH, 2014: LiDAR Compressor. – <http://www.lizardtech.com/products/lidar> (6.12.2014).
- MALLAT, S.G., 1989: A theory for multiresolution signal decomposition: the wavelet representation. – IEEE Transactions on Pattern Analysis, and Machine Intelligence **11** (7): 674–693.
- MALLET, C. & BRETAR, F., 2009: Full-waveform topographic lidar: State-of-the-art. – ISPRS Journal of Photogrammetry and Remote Sensing **64** (1): 1–16.
- MALLET, C., BRETAR, F., ROUX, M., SOERGEL, U. & HEIPKE, C., 2011: Relevance assessment of full-waveform lidar data for urban area classification. – ISPRS Journal of Photogrammetry and Remote Sensing **66** (6): 71–84.
- MONGUS, D. & ŽALIK, B., 2011: Efficient method for lossless LiDAR data compression. – International Journal of Remote Sensing **32** (9): 2507–2518.
- OPENJPEG, 2014: OpenJPEG library: an open source JPEG 2000 codec. – <http://www.openjpeg.org/> (31.10.2014).
- PARRISH, C.E. & NOWAK, R.D., 2009: Improved Approach to LiDAR Airport Obstruction Surveying Using Full-Waveform Data. – Journal of Surveying Engineering **135** (2): 72–82.
- PIROTTI, F., 2011: Analysis of full-waveform LiDAR data for forestry applications: a review of investigations and methods. – iForest-Biogeosciences and Forestry **4** (3): 100–106.
- PRADHAN, B., KUMAR, S., MANSOR, S., RAMLI, A.R. & SHARIF, A.R.B.M., 2005: Light detection and ranging (LiDAR) data compression. – KMITL Science and Technology Journal **5** (3): 515–523.
- QUIRK, M.D., 2003: Theory of Principal Component Filter Banks with Applications to Multi-component Imagery. – Ph.D. thesis, The University of Texas at Austin, Austin, TX, USA.
- REITBERGER, J., KRZYSZEK, P. & STILLA, U., 2008: Analysis of full waveform LiDAR data for the classification of deciduous and coniferous trees. – International Journal of Remote Sensing **29** (5):1407–1431.
- SPDLIB, 2013: The SPDLIB Documentation Wiki. – <http://www.spdlib.org/> (30.10.2014).
- STILLA, U. & JUTZI, B., 2008: Waveform analysis for small-footprint pulsed laser systems. – SHAN, J. & TOTH, C.K. (eds.): Topographic laser ranging and scanning: Principles and processing: 215–234, CRC Press.
- TAUBMAN, D. & MARCELLIN, M., 2002: JPEG2000: Image Compression Fundamentals, Standards and Practice. – Springer.
- THE HDF GROUP, 2014: HDF Group – HDF5. – <http://www.hdfgroup.org/HDF5/> (30.10.2014).
- THE INTERNET ENGINEERING TASK FORCE (IETF), 1996: RFC 1951 – DEFLATE Compressed Data Format Specification Version 1.3. – <http://tools.ietf.org/html/rfc1951> (30.10.2014).
- TOTH, C., LAKY, S., ZALETNYIK, P. & GREJNER-BRZEZINSKA, D., 2010: Compressing and classifying LiDAR waveform data. – International Archives of Photogrammetry, Remote Sensing and Spatial Information Sciences **38** (Part 1): (on CD-ROM).
- VAIDYANATHAN, P.P., 1993: Multirate Systems and Filter Banks. – Prentice Hall PTR.
- VAIDYANATHAN, P.P., 1998: Theory of Optimal Orthonormal Subband Coders. – IEEE Transactions on Signal Processing **46** (6): 1528–1545.

Address of the Authors:

GRZEGORZ JÓZKÓW, CHARLES TOTH & DOROTA GREJNER-BRZEZINSKA, Department of Civil, Environmental and Geodetic Engineering, The Ohio State University, Hitchcock Hall, 2070 Neil Avenue, US-43210 Columbus, OH, USA, Tel.: +1-614-292-7681, +1-614-292-8787, e-mail: {jozkow.1} {toth.2} {grejner-brzezinska.1}@osu.edu

MIHAELA QUIRK, The National Intelligence University, e-mail: mihaela.quirk@dodiis.mil

Manuskript eingereicht: August 2014

Angenommen: Februar 2015